UNIVERSITEIT VAN PRETORIA
UNIVERSITY OF PRETORIA
YUNIBESITHI YA PRETORIA

MODEL-BASED ESTIMATION AND CONTROL OF WHEEL SLIP IN LOCOMOTIVES

by

Charl Viljoen van de Merwe

Submitted in partial fulfillment of the requirements for the degree
Master of Engineering (Electronic Engineering)

in the

Department of Electrical, Electronic and Computer Engineering
Faculty of Engineering, Built Environment and Information Technology

UNIVERSITY OF PRETORIA

October 2023

SUMMARY

MODEL-BASED ESTIMATION AND CONTROL OF WHEEL SLIP IN LOCOMOTIVES

by

Charl Viljoen van de Merwe

Supervisor:	Prof. J.D. le Roux
Department:	Electrical, Electronic and Computer Engineering
University:	University of Pretoria
Degree:	Master of Engineering (Electronic Engineering)
Keywords:	Kalman filter, Locomotives, Modelling, Parameter estimation, Railways, Slip control

This dissertation investigates wheel slip control of locomotive traction systems in the presence of non-linear wheel surface behaviour and varying adhesion conditions. It is difficult to determine when the maximum point of adhesion has been exceeded since the adhesion coefficient cannot be measured directly during the operation of the locomotive. Therefore, classical slip controllers suppress excessive slip by using predetermined thresholds for the slip velocities and accelerations of the axles. The classical methods are convenient but cannot maximise adhesion utilisation.

Modern methods continuously modulate the torque and are expected to produce superior performance if implemented effectively. Most continuous controllers calculate the reaction torque using a generated slip ratio (slip velocity divided by the locomotive velocity) reference and a slip ratio estimate feedback. Computing the estimate depends on an accurate locomotive velocity estimate, which is difficult to obtain when all the wheelsets of a locomotive are driven. Slip ratio reference generation generally requires estimates of the slip ratio and adhesion coefficient or adhesion force. This dissertation focuses on producing accurate estimates to enable effective slip control.

Adhesion force is the adhesion coefficient multiplied by the normal force. The adhesion coefficient is dependent on the rail conditions. Under constant rail conditions, it varies only with a wheel load and slip ratio change. Therefore, the normal forces, wheel velocities, and locomotive velocity should be modelled accurately to ensure the model produces realistic adhesion coefficients. A linearised railway vehicle model could be well over the 100th order. Such models are helpful for design and validation, but using such complex models in model-based filter or estimator design is impractical.

In this dissertation, a new simulation model is developed that includes the longitudinal, pitch, vertical, and wheelset rotational dynamics. In addition, it includes a unique approach to the coupler force by modelling the wagons using a single-axle wheelset model. This model captured the desired dynamics, including wheelset torsional vibrations and oscillations in the pitch dynamics.

A linear state-observable estimator is developed to produce estimates of slip ratios and adhesion coefficients. The estimation model is an adaptation of the simulation model, but the adhesion forces and coupler force are modelled as unknown disturbances. This estimator requires measurements of the locomotive longitudinal acceleration and velocity, body pitch angle and rate, and the motor angular velocities. The rail angle and motor torque estimates should be provided to the estimator.

The estimates are used in a novel slip ratio reference adaptation method to provide a reference to an adaptive PI controller. The PI controller is used to compute the reaction torque to prevent unstable slip in the rear/reference wheelset, while a speed differential controller is used to prevent slip in the other wheelsets.

The simulation results indicate that the estimator and controller configuration can suppress unstable slip under varying adhesion conditions, thereby preventing damage to the wheels and rail while ensuring maximum adhesion utilisation. Maximum adhesion utilisation allows a locomotive to increase its hauling capacity without increasing its mass.

ACKNOWLEDGMENTS

I want to express my sincere thanks to my supervisor, Prof Derik Le Roux, for his guidance and patience throughout the process.

Thank you to Prof David Limebeer for generously imparting knowledge on modelling, model-order reduction, and estimation.

Thank you to my colleagues at Transnet for helping me to keep my research grounded in reality.

I want to thank my parents for their ever-loving support and encouragement.

Many individuals, not named here, played a part in helping me achieve this milestone. Thank you to all of you. Finally, all the honour and glory to God, the root of all knowledge.

LIST OF ABBREVIATIONS

AC	Alternating Current
ABS	Anti-lock Braking Systems
CAD	Computer Aided Design
COG	Centre of Gravity
DC	Direct Current
DTC	Direct Torque Control
EV	Electric Vehicle
FOC	Field Oriented Control
IGBT	Insulated Gate Bipolar Transistor
IMU	Inertial Measurement Unit
LQR	Linear Quadratic Regulator
MPC	Model Predictive Controller
PCC	Power Converter Cubicle
PID	Proportional Integral Derivative (Controller)
SMC	Sliding Mode Controller

TABLE OF CONTENTS

LIST OF FIGURES

LIST OF TABLES

CHAPTER 1 INTRODUCTION

1.1 PROBLEM STATEMENT

Railway transportation is considered one of the most energy-efficient and eco-friendly modes of transport. There is a constant need for improvement of the efficiency and reliability of traction systems and the development of these systems at the lowest cost and highest quality [1].

Producing maximum tractive effort while preventing unstable wheel slip is an important objective in designing traction control systems for locomotives. Increasing the adhesion utilisation increases the hauling capacity of a locomotive. Unstable wheel slip is caused when the traction torque is too large and the maximum available adhesion point for the specific conditions between the wheels and rail is exceeded. When unstable slip occurs, the traction force decreases, and the wheels and rail can suffer damage [2].

It is difficult to determine when the maximum point of adhesion has been exceeded since the adhesion coefficient cannot be measured directly during the operation of the locomotive [3]. Classical slip controllers suppress excessive slip by using predetermined thresholds for the slip velocities and accelerations of the axles [2]. The classical methods are convenient but cannot maximise adhesion utilisation (producing the maximum tractive effort without unstable slip).

1.1.1 Context of the problem

Transnet, South Africa's state-owned rail, ports and pipeline company, has embarked on developing a power converter cubicle (PCC). The PCC contains inverters controlling alternating current (AC) traction motors. The PCC is powered by a diesel generator on a diesel locomotive and from overhead cables on an electric locomotive. In addition to accurately controlling the torque of traction motors, the PCC is responsible for detecting and suppressing unstable slip.

The current PCC prototype is being developed for Transnet's 8E locomotive. The 8E is an old direct current (DC) electric locomotive being converted to a diesel locomotive with AC traction motors. It is a Bo-Bo locomotive, meaning it has two wheelsets per bogie, as shown in Fig. 1.1. The simulations and control design in this dissertation are based on this locomotive.

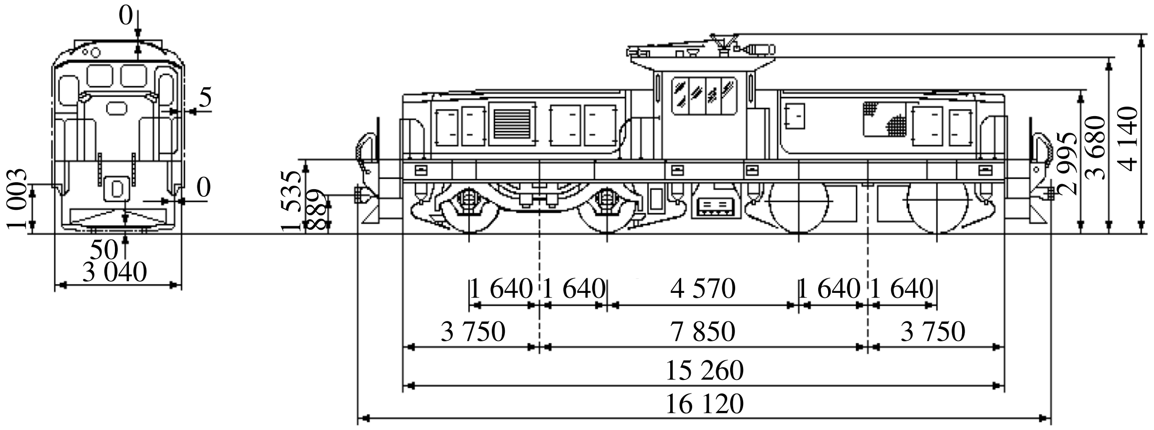

Figure 1.1. Transnet 8E locomotive.

Generally, slip refers to a positive slip velocity (wheel surface velocity is larger than the locomotive velocity), and slide refers to a negative slip velocity. The difference is significant in automotive vehicles, where tractive power is supplied by the engine and braking power is provided hydraulically. However, for modern locomotives, the traction and braking power is supplied by the traction motors. This braking mode is often called dynamic braking since the motors generate electrical power during braking. Locomotive(s) and wagons in a train are equipped with air brakes (controlled by the locomotive), which may work in conjunction with dynamic braking [4]. However, the 8E's air brakes are used only to keep the train stationary when parked and as an emergency stopping mechanism. Therefore, while this dissertation focuses on slip, it is assumed that the controller will also work for slide conditions.

1.1.2 Research gap

Most slip control methods depend on the slip ratios and estimates of the adhesion coefficients of the wheelsets. Longitudinal creep, or slip ratio, is the slip velocity divided by the locomotive longitudinal velocity. The slip velocity is the difference between the longitudinal velocity of a wheel, i.e., the locomotive velocity, and the wheel circumference/surface velocity. These methods are fallible because of small errors in the measurements of wheel and locomotive velocities [5]. Therefore, a model-based approach that provides estimated adhesion forces and filtered velocity measurements would be beneficial. Such an estimator may require a complex model of the locomotive.

Various modern slip control systems have been proposed and implemented in recent years, but there has yet to emerge a single approach that the industry has widely accepted as a superior (or optimal) controller. The development of a modern slip control system that is reliable, practical, simple, and cost-effective is needed.

1.2 RESEARCH OBJECTIVE AND QUESTIONS

The main focus of this research is the following question: Can a slip controller be developed using model-based estimation suitable for real-time control onboard a locomotive?

To answer this question, the following sub-questions have to be addressed:

1. What is the necessary level of complexity of the locomotive dynamics modelling for simulation (to test the control and validate the results)? The required complexity of each of the following parts needs to be determined:
   (a) Wheel-rail adhesion interaction.
   (b) Modelling along all the degrees of freedom (longitudinal, lateral, vertical, roll, pitch, and yaw) for the locomotive body, bogies, and wheelsets.
   (c) Wheelset rotational dynamics.
   (d) Effects of rail geometry (slope and curves).
   (e) Traction system (generator, inverters, and motors).
2. What is the level of complexity needed for the estimator model?
3. Are all the parameters needed for control measurable? If some are not, can they be estimated? Some of these parameters that need to be investigated are the locomotive velocity, slip ratio, motor torque, and the adhesion coefficient or adhesion force.
4. Which control scheme is most appropriate, e.g., fuzzy logic, proportional-integral-derivative (PID) control, or a more complex controller such as a model predictive controller (MPC)?

1.3 APPROACH

1.3.1 Simulation and Estimation Models

A linearised model of a railway vehicle could be well over 100th order. These models are useful for simulation, but using such complex models in the model-based estimator is impractical [6]. The important parameters (that need to be measured/estimated) and the complexity of the locomotive control system should inform the required complexity of the estimator model [7].

1.3.2 Slip Controller

There are two macro trends in slip controllers. In the first, the control objective is achieved by discretely modulating the applied torque, which includes rule-based (also referred to as dynamic threshold-based), fuzzy-logic, and neural-network controllers. In the second, the torque is modulated continuously, which includes PID, linear quadratic, sliding mode, robust, and MPC [8].

The industry has predominantly used rule-based controllers [8, 9]. One of the benefits of fuzzy controllers is that they do not need an accurate system model [10]. Experimental results showed that fuzzy logic controllers are better than proportional-integral (PI) type controllers with constant gains [10].

In the initial development of automotive anti-lock braking systems (ABS), there were no alternatives to rule-based controllers due to the limited bandwidth of traditional hydraulic systems. Since the 2000s, the emergence of decoupled brake systems has made it possible to implement continuous slip control [9]. If continuous controllers are implemented effectively and paired with model-based estimators, they are expected to perform better.

1.3.3 Results Validation

This dissertation entails the theoretical development of a model and controller that depend on parameters that can be measured or estimated with sufficient accuracy. It must be shown that the developed system can be implemented practically using available measurements.

To test slip control on an actual locomotive is generally costly, requires a lot of manpower, and material resources need to be coordinated [2]. Therefore, the development of the slip control system cannot depend solely on physical testing on a locomotive.

A single-axle wheelset model is generally used to study and analyse the adhesion behaviour. A limitation of this model is that the integrity of the locomotive and interaction among the different axles are ignored [2]. Simple modelling can be used to develop the estimator and controller but cannot be used to validate whether it will produce good practical results.

The best compromise is advanced modelling using a co-simulation. In this approach, the multi-body software considers the mechanical and traction components, separated from the software that models the electrical system and control. There are several multi-body simulation software programs that could be used for co-simulation, such as NUCARS, GENSYS, VAMPIRE, VI-RAIL, SIMPACK, and Universal Mechanism [4].

While a multi-body simulation would be beneficial, constructing a multi-body model requires significant modelling effort and expertise. Therefore, a sufficiently complex simulation model should be developed from first principles instead. This model will be used in simulation to validate whether the estimator and controller function as expected. Such a model will provide more insight than a simple single-axle wheelset model. A co-simulation will be left as future work.

1.4 RESEARCH GOALS

The research goals are:

1. **State-Observable Estimator:** As mentioned in Section 1.3.2, it is expected that continuous controllers (such as PI controllers) should be able to produce good slip control if the parameters that are needed for control, such as the slip ratios and adhesion coefficients, can be estimated accurately. The main focus of this dissertation is to develop a state-observable estimator that can produce these estimates.
2. **Slip Controller:** A slip controller that can suppress unstable slip and achieve high adhesion utilisation should be developed. The estimator and controller should be able to be used onboard a locomotive in real-time.
3. **Simulation:** A simulation capturing the dynamics important for slip-control should be used to validate whether the developed estimator and controller can deliver the desired results.

1.5 RESEARCH CONTRIBUTIONS

The key contributions of this dissertation are:

1. A simulation model is developed, which includes a pitch-plane locomotive model, a five-mass wheelset model for each individual wheelset, and a unique approach to the coupler force by modelling the wagons using a single-axle wheelset model.
2. A linear state-observable estimator is developed that can produce estimates of the slip ratios and adhesion coefficients of each wheelset. It requires measurements of the locomotive longitudinal acceleration and velocity, body pitch angle and rate, and the motor angular velocities.
3. An adaptive PI controller with anti-windup is used, which requires a slip ratio reference. A novel slip ratio reference adaptation method is developed. It utilises the slip ratio, locomotive velocity, and adhesion coefficient estimates.

In summary, it is demonstrated that combining a slip controller with a model-based estimator suitable for real-time control onboard a locomotive allows for efficient slip control.

1.6 RESEARCH OUTPUTS

The following publications resulted from this study:

1. Charl V. Van de Merwe, Johan D. le Roux, David J. N. Limebeer, "Locomotive Wheel-Slip Control with Slip Ratio Reference Adaptation using Model-Based Estimation," in *submitted to IEEE Transaction on Control Systems Technology*, 2023.
2. C. V. Van de Merwe, J. D. le Roux, "Estimation of Locomotive Adhesion Coefficients and Slip Ratios," *2023 American Control Conference (ACC)*, San Diego, CA, USA, 31 May - 2 Jun. 2023. pp. 2252-2257, doi: 10.23919/ACC55779.2023.10155953.
3. C. V. Van de Merwe, J. D. le Roux, "Model-Based Estimation of Wheel Slip in Locomotives," *2022 European Control Conference (ECC)*, London, United Kingdom, 12-15 Jul. 2022, pp. 2124-2129, doi: 10.23919/ECC55457.2022.9838075.

1.7 OVERVIEW OF THE STUDY

Chapter 2 reviews the available literature. In Chapter 3, the simulation model is presented. Chapter 4 presents the estimator. Chapter 5 shows the development of the slip controller and slip ratio reference adapter. The final simulation results of Chapter 5 combine the simulation model, estimator, reference adapter, and slip control, as shown in Fig. 1.2, to validate the effectiveness of the chosen slip control strategy. Chapter 6 provides concluding remarks.

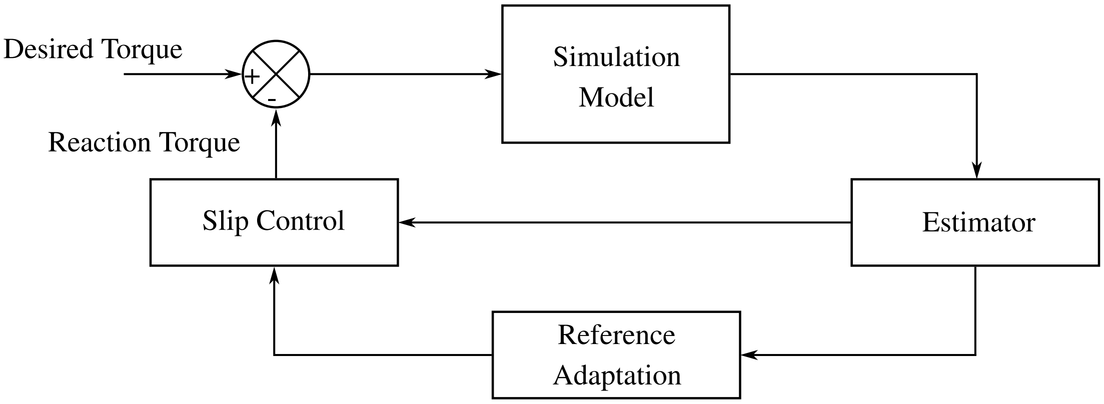

Figure 1.2. Slip control overview.

CHAPTER 2 LITERATURE STUDY

2.1 CHAPTER OVERVIEW

This chapter presents the literature study for this dissertation. Section 2.2 discusses the technological advances in locomotive traction systems. The mechanical and traction systems relevant to the specific locomotive shown in Fig. 1.1 are discussed in Section 2.3. Before the different slip control methods are explored in Section 2.5, an understanding of the wheel-rail contact dynamics is needed, as discussed in Section 2.4. Slip parameter estimation is discussed in Section 2.7. The chapter is concluded in Section 2.8.

2.2 TECHNOLOGICAL ADVANCES IN LOCOMOTIVE TRACTION SYSTEMS

The first known overland precursor to railways was the Wollarton Wagonway in Nottingham, England, which carried coal in wagons with flanged wheels running on wooden rails over several kilometres, operating from 1604 to 1614. The development from wagonways to conventional railways occurred during the Industrial Revolution, commencing in Great Britain before quickly spreading through the Western world. Steam power and metallurgy developments allowed locomotives to haul loads many times their weight by realising significant tractive effort from the friction between smooth flanged wheels and rails. Diesel and electrical traction locomotives were developed in parallel in the second quarter of the twentieth century, with electrical locomotives becoming popular in Europe after World War II. Only about 300,000 km of the world's approximately 1.4 million km of railways are electrified [4].

Locomotives used DC propulsion systems, first controlled using diode rectifiers and later phase-controller thyristors, until the 1990s. Due to the robustness and low cost of squirrel-cage induction motors, AC propulsion systems were adopted in the 1990s. The introduction of insulated gate bipolar transistors (IGBTs) significantly boosted inverter efficiency to over 98% while simultaneously reducing harmonics and losses in traction transformers [1]. Digital control strategies of IGBTs of AC motors, such as field-oriented control [1], allow for fast and accurate torque control, which enables slip control strategies that were not applicable before [9, 11].

2.3 LOCOMOTIVE SUBSYSTEMS

Before considering slip control, the mechanical and traction topologies of locomotives have to be understood. The manner in which torque is delivered to the locomotive, as well as the control architecture of the locomotive, determines whether some slip control methods are suitable or not.

2.3.1 Mechanical Components

The mechanical components of a locomotive are shown in Fig. 2.1, where the numbered parts are: 1 - car body; 2 – driver's compartment (cab); 3 – equipment compartments; 4 – main frame; 5 – coupling device; 6 – Cowcatcher; 7 – fuel tank; 8 – air reservoirs; 9 – battery compartment; 10 - bogies; 11 – wheelsets; 12 – axle boxes; 13 – traction motors; 14 – gearboxes; 15 – brake cylinders; 16 – sandboxes [4].

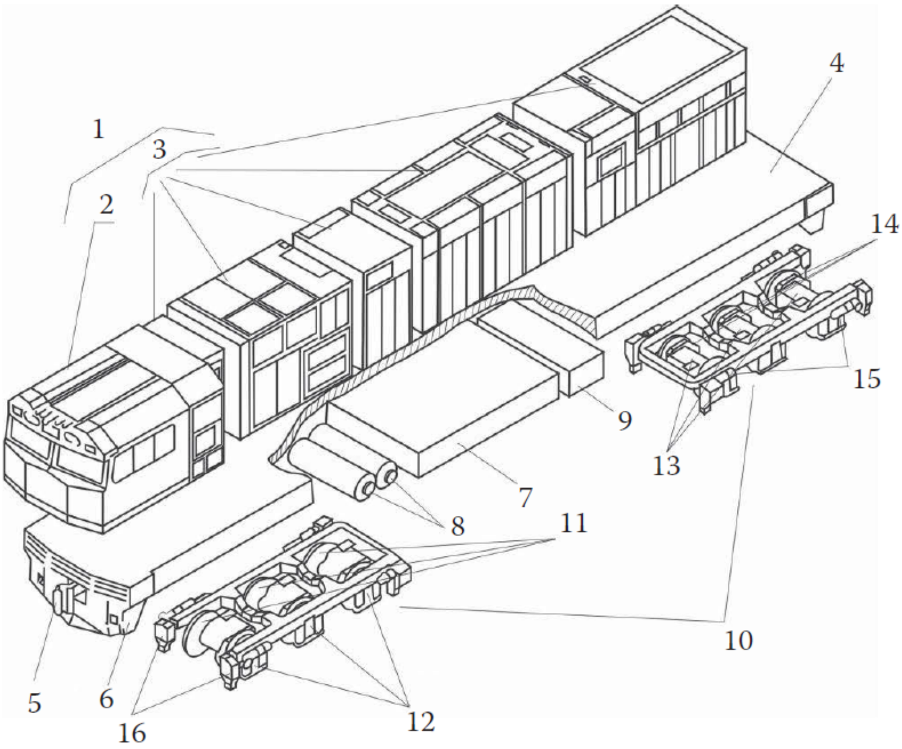

Figure 2.1. Mechanical components of a locomotive. Taken from [4], with permission.

Locomotive bogies are either Co-Co or Bo-Bo, which refers to three or two wheelsets per bogie. The 8E, for which this dissertation is intended, is a Bo-Bo locomotive, meaning it has two wheelsets per bogie, as shown in Fig. 1.1.

2.3.2 Traction Systems

2.3.2.1 Power Supply and Traction Motors

A typical power architecture of a heavy rail diesel locomotive is given in Fig. 2.2. The diesel engine is the power supply to the locomotive. The generated power is rectified and applied to the DC-link, from which power is fed to the traction motors through inverters controlled by the traction control units.

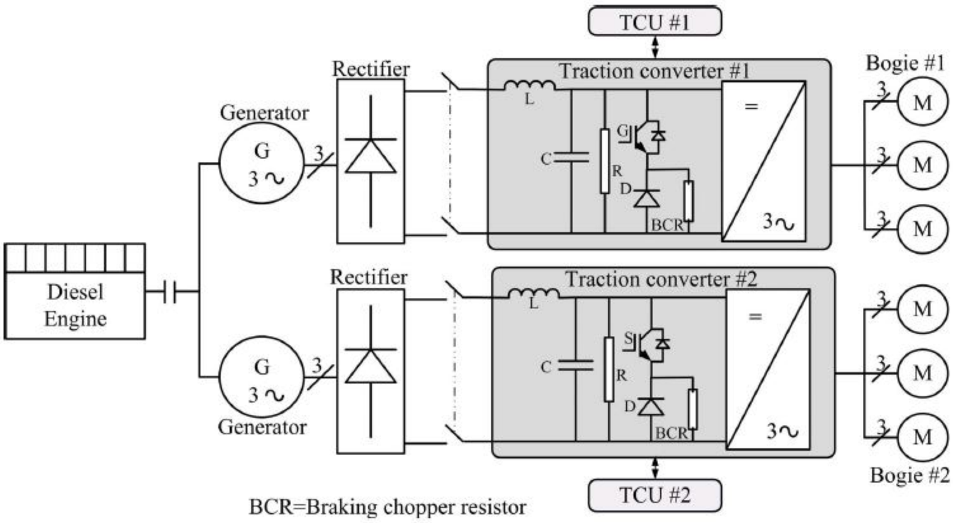

Figure 2.2. Typical power architecture of a heavy rail diesel locomotive. Taken from [1], © 2017 IEEE.

The traction configurations of a locomotive are categorised as locomotive traction control, where all the motors are controlled by a single inverter, bogie traction control, where each bogie has its own inverter, and individual wheelset or axle control, where each wheelset is controlled by its own inverter. The 8E is a diesel shunting locomotive that has individual wheelset control, allowing independent traction and slip control for each wheelset.

The speed of a passenger train is typically higher than that of a freight train, but the weight and required tractive effort of a freight locomotive are higher [3].

2.3.2.2 Operator Tractive Effort Control

The locomotive operator selects a throttle notch to set the required tractive effort. A diesel-electric locomotive typically has eight notches (levels) of throttle adjustment [7].

The traction system is limited by current at low velocities and limited by power at higher velocities. Therefore, tractive effort is applied proportionally to the notch levels at low velocities, and the available tractive effort decreases at higher velocities. Accordingly, the tractive effort command, F_t (N), can be calculated as follows [4]:

$$F_t = \begin{cases} (N/8)\,F_{\max} - k_f v_d & ; \quad v_d < v_{\text{cross}} \\ (N/8)^2\,P_{\max}/v_d & ; \quad \text{otherwise}, \end{cases} \tag{2.1}$$

with:

$$v_{\text{cross}} = \frac{(N/8)F_{\max} - \sqrt{((N/8)F_{\max})^2 - 4k_f P_{\max}(N/8)^2}}{2k_f}, \tag{2.2}$$

where v_d (m/s) is the wheel velocity at the wheel-rail contact point, v_{cross} (m/s) is the crossover velocity from which the system is limited by power, F_t (N) is the tractive effort command, $F_{\max}$ (N) is the maximum tractive effort that the locomotive can produce, $P_{\max}$ (W) is the maximum locomotive tractive power, N [0 to 8] is the notch setting selected, and k_f (N $\cdot$ s/m) is the torque reduction factor. This function is plotted for each notch in Fig. 2.3.

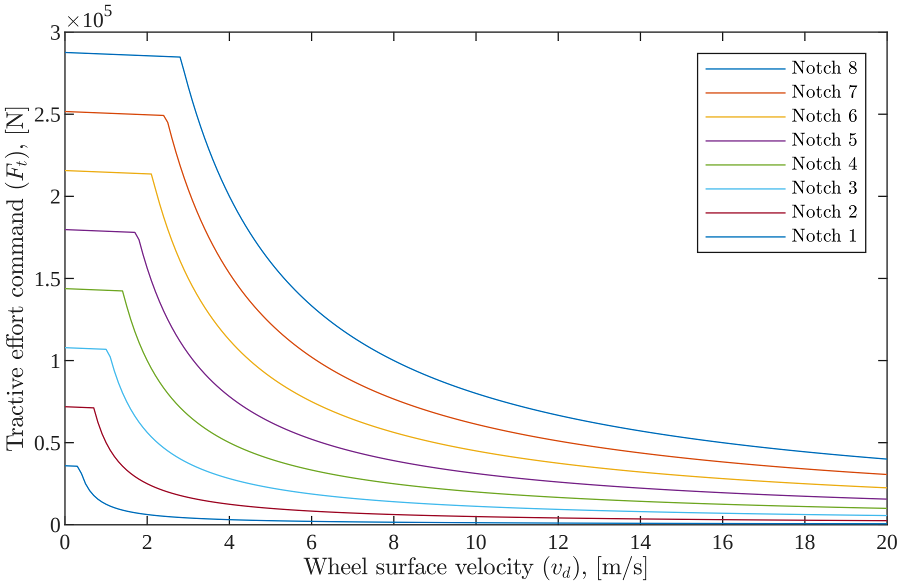

Figure 2.3. Tractive effort command curves.

For individual wheelset control, the torque required from each wheelset is calculated by:

$$T^* = \frac{r}{nR} F_t, \tag{2.3}$$

where T^* (N $\cdot$ m) is the motor torque setpoint, r (m) is the distance from the axle centre to the wheel-rail contact surface (wheel radius), n is the axle count of the locomotive, and R is the gear ratio of the gearbox [4].

Note that the torque setpoints are calculated from the wheel velocities, not the locomotive velocity. In the case of excessive slip where the wheel surface velocity is much larger than the locomotive velocity, the torque setpoint will be reduced, and the slip will be suppressed. This control response is slow at high velocities and insufficient for slip control. However, the torque reduction factor, k_f, (which determines the initial slope of the curves in Fig. 2.3) is specifically designed to suppress slip at velocities smaller than the crossover velocity, v_{cross}.

2.3.2.3 Induction Motor Torque Control

Algorithms used to control the torque of the motors include field-oriented control (FOC), direct torque control (DTC), DTC with space vector modulation and model predictive DTC [1]. These methods have varied advantages and disadvantages, but all produce a fast torque response relative to the relatively slow dynamics of the locomotive.

2.4 WHEEL-RAIL CONTACT DYNAMICS

Delivered tractive effort depends on the wheel-rail behaviour (described by the adhesion coefficient to slip ratio characteristic curve), which is a complex time-varying and non-linear process subject to the axle loads, temperature, humidity and other factors [12]. The relationship between the tractive effort and the adhesion coefficient is:

$$F_a = \mu_{\text{actual}} F_N, \tag{2.4}$$

where F_a (N) is the adhesion force, μ_{actual} is the actual (or realised) adhesion coefficient, and F_N (N) is the wheel-rail normal force or wheel load.

The adhesion coefficient cannot be measured directly during the locomotive run [3]. Lowering of adhesion may be caused by many factors, including rain, oil contamination, condensation of water droplets or compressed leaves [13]. In addition, determining the maximum adhesion coefficient is difficult due to unexpected slip, the difference between wheel diameters of wheel pairs, track curvature, redistribution of load between wheels, and vibration [5].

Literature describes the adhesion characteristic either by approximating the adhesion coefficient to slip ratio characteristic curve shape or by considering the wheel-rail contact parameters. Both methods agree on the curve shape, but the position of maximum adhesion may differ [3].

2.4.1 Burckhardt's Simplified Model

The adhesion coefficient to slip ratio characteristic curve as described by Burckhardt's simplified model is [12]:

$$\mu_{\text{actual}} = c_1(1 - e^{-c_2\lambda}) - c_3\lambda, \tag{2.5}$$

$$\lambda = \frac{v_s}{v_t} \tag{2.6}$$

$$v_s = v_d - v_t \tag{2.7}$$

where c_1, c_2 and c_3 represent model parameters, λ is the slip ratio, v_s (m/s) is the slip velocity, v_d (m/s) is the wheel velocity at the rail, and v_t (m/s) is the locomotive velocity

2.4.2 LuGre Model

The LuGre model is an alternative to the Burckhardt model often used in automotive ABS research [14, 15]:

$$F_a = (\sigma_0 p + \sigma_1 \frac{dp}{dt} + \sigma_2 v_s) F_N \tag{2.8}$$

$$\frac{dp}{dt} = v_s - \sigma_0 \frac{|v_s|}{h(v_s)} p \tag{2.9}$$

$$h(v_s) = \mu_c + (\mu_s - \mu_c) e^{-\frac{v_s}{v_S}^{\gamma}}, \tag{2.10}$$

where μ_c and μ_s are the normalized Coulomb and static friction coefficients respectively, p is the internal friction state, and σ_0, σ_1, σ_2, γ are model parameters. Extensive experiments are needed to determine the model parameters [16].

2.4.3 Polach Model

The Polach model is a railway-specific model verified through extensive experiments [16] and is usually used to calculate the adhesion force [2]. It includes the assumption that the initial creep/slip ratio curve has a varying slope for different adhesion conditions. It also models the non-linear adhesion characteristics beyond the creep saturation [17]. This model is used throughout this dissertation. It is described below [2, 5, 18, 19].

The adhesion coefficient μ is described by:

$$\mu = \mu_0((1 - \frac{\mu_\infty}{\mu_0})e^{-Bv_s} + \frac{\mu_\infty}{\mu_0}) \tag{2.11}$$

where μ_0 is the maximum friction coefficient at zero slip, μ_∞ is the maximum friction coefficient at infinity slip, and B is the coefficient of exponential friction decrease. The adhesion force is described by:

$$F_a = \frac{2\mu Q}{\pi}\left(\frac{k_A \varepsilon}{1+(k_A\,\varepsilon)^2} + \arctan(k_S\,\varepsilon)\right), \tag{2.12}$$

with:

$$\varepsilon = \frac{G\pi abC_1}{4Q\mu}\lambda \tag{2.13}$$

where $Q = F_N$ (N) is the wheel load, k_A and k_S are reduction factors in the adhesion area, ε is the gradient of the tangential stress in the adhesion area, G is the shear modulus, a and b are the lengths of the semi-axis of the elliptic contact patch respectively, C_1 is the Kalker linear theory coefficient [20], and λ is the slip ratio or creep.

By defining the adhesion force as the product of the actual (or realised) adhesion and the force between the wheel and rail as in (2.4), the actual adhesion coefficient is described by:

$$\mu_{\text{actual}} = \frac{2\mu}{\pi}\left(\frac{k_A \varepsilon}{1+(k_A\,\varepsilon)^2} + \arctan(k_S\,\varepsilon)\right). \tag{2.14}$$

This function is plotted in Fig. 2.4 using the parameters in Table B.1 and B.2. Whenever the adhesion coefficient is referred to in the rest of this dissertation, it refers to the actual adhesion coefficient, μ_{actual}.

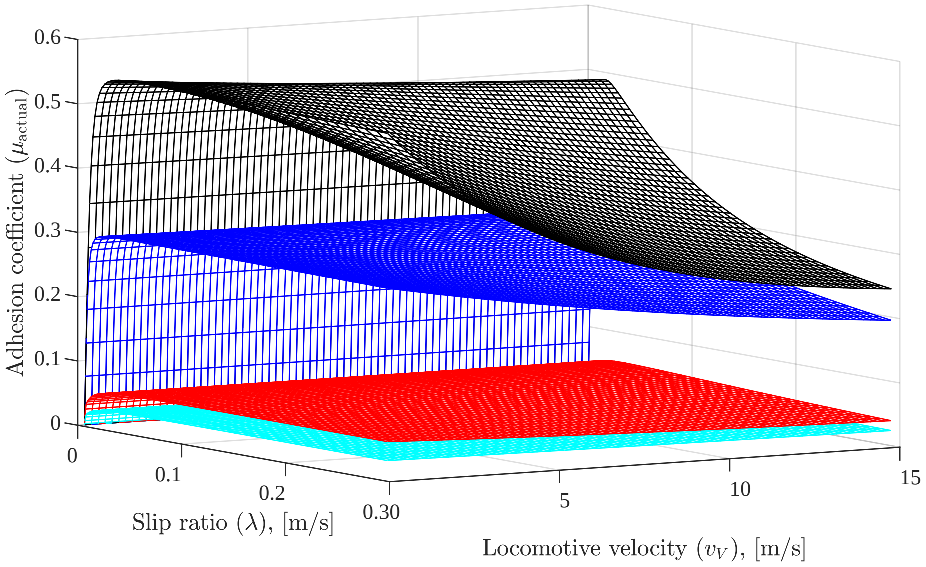

Figure 2.4. Adhesion plot (actual adhesion) in dry (black), wet (blue), low (red), and very low (cyan) adhesion conditions.

2.5 SLIP CONTROLLERS

Unstable wheel slip is caused when the traction force is larger than the maximum available adhesion force between the wheels and the rail. Once the maximum available adhesion is exceeded, the slip velocity will continue to increase without an increase in adhesion force if the torque is not decreased [2]. Unstable slip should be avoided since it causes flat spots on the wheels [21]. It is difficult to determine when the maximum available adhesion is exceeded because the adhesion coefficient cannot be measured directly, and the adhesion conditions are generally unknown.

A slip controller should attempt to maintain the operating point of the adhesion coefficient in the stable area or close to the maximum adhesion point (to the left of the peak in the adhesion coefficient with respect to the slip ratio in Fig. 2.4). The parameters required to perform slip control depend on the method used.

Some slip control methods investigated here are from automotive ABS. There are significant differences between locomotive slip control and ABS. For example, the wheel-rail contact surface is smoother (lower adhesion) [22], making the detection of the optimal adhesion point more difficult. In most industrial ABS solutions, slip control uses rule-based wheel torque control through hydraulic brake actuators. The latest trends in vehicle electrification have given rise to revising slip control since electric vehicles (EVs) are capable of accurate individual wheel torque control [9, 11]. Therefore, recent automotive studies are more relevant to locomotive slip control.

2.5.1 Starting Strategy

Slip control strategies generally require knowledge of the ground velocity of a locomotive [4]. The locomotive velocity is difficult to determine when all the wheels are driven [3], especially at low speeds [4]. The slip controller of a locomotive will typically be equipped with a separate starting starting strategy for speeds between 0 and 5 km/h and an adhesion/creep strategy at speeds higher than 5 km/h (18 m/s). The starting strategy usually relies on the traction motor speeds and accelerations [4]. Depending on the requirements for the specific locomotive, the torque reduction factor, k_f, as mentioned in Section 2.3.2.2, could be sufficient to develop a control strategy.

2.5.2 Speed Differential Control

When the locomotive is accelerating, the weight redistribution causes a decrease in the normal force of the front wheelsets and an increase in the rear wheelsets. The front wheelset (with the smallest of normal force) will slip first. If slip can be prevented in the rear wheelset, its speed can be used as a reference speed to the other wheelsets, thereby reducing the torque if they slip [23]. A similar approach is control based on comparing the traction motor currents since the difference in speeds will also result in a difference in current [4].

Sole reliance on the starting strategy and speed differential controllers will not produce optimal slip control since the slip still has to be controlled in the rear wheelset at higher speeds using an alternative control method.

2.5.3 Rule-Based Control

Rule-based slip control methods use predetermined threshold values for the slip velocity and acceleration of each axle. When slip is detected, the torque is rapidly decreased to suppress the slip. After slip is suppressed, the traction torque is increased stepwise [2]. Similarly, slip can be detected when the derivative of the estimated load (or disturbance) torque, caused by the adhesion force, drops by a certain threshold [24].

These methods require large amounts of tuning of the threshold values and recovery rates. They may be able to suppress excessive slip, but they will not be able to maintain the operating point close to the maximum adhesion point.

2.5.4 Fuzzy Logic

Fuzzy logic controllers have been widely used because of the amount of uncertainty due to the non-linear wheel-surface behaviour and noisy or uncertain state variables [8].

A popular approach is identifying the current road condition and generating the required torque signals using a combined fuzzy logic element and a decision logic network based on current and past data of the applied torques and wheel slip ratios [8, 25]. Considering the curves in Fig. 2.5, a fuzzy logic controller can assume that if the motor torque and the slip ratio increase, the operating point is in the stable region (left of the peaks). If the torque increases and the slip ratio decreases, the operating point is in the unstable region [25, 26]. An alternative controller has been proposed in [10] that depends on the derivative of an estimate of the adhesion coefficient and the derivative of the slip ratio.

These controllers do not require accurate mathematical models [10]. A drawback of this approach is that it involves tuning many parameters [8].

2.5.5 PI Control

PI and PID controllers are the most used controllers in general. However, they do not cope well with non-linearities and changes in process behaviour. Therefore, they do not perform best under the varying operating conditions in slip control [8]. They are simple to implement, but oscillatory behaviour of the wheel slip may occur [9].

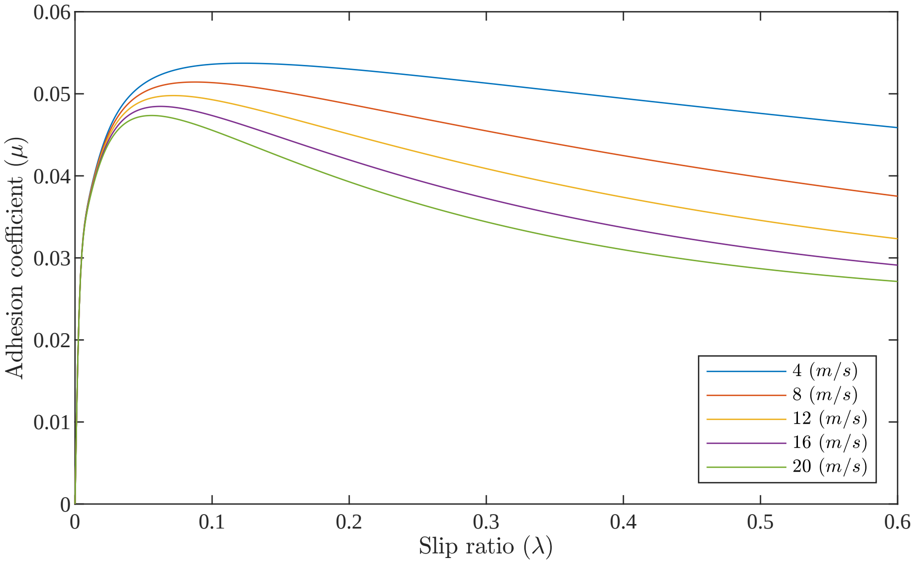

Figure 2.5. Adhesion coefficient vs slip ratios at different locomotive velocities at low adhesion conditions.

The derivative term in PID controllers can amplify process noise [8]; therefore, PI controllers are preferred for slip control. The viability of the PI control strategy depends on the chosen inputs to the controller and the noise levels of these inputs.

The conventional PI slip controller computes the reactive torque (the amount of torque by which the applied torque should be reduced) using the optimal slip ratio (corresponding to the maximum adhesion coefficient) as the reference and the estimated slip ratio as the feedback [4, 8, 9], as seen in Fig. 2.6. The slip controller should only reduce the applied torque if the slip ratio is larger than the optimal ratio (unstable slip). Therefore, the error signal, e_λ, is computed as follows [9]:

$$e_\lambda = \begin{cases} \lambda - \lambda_R & ; \quad \lambda > \lambda_R \\ 0 & ; \quad \text{otherwise,} \end{cases} \tag{2.15}$$

where λ is the actual or estimated slip ratio, and λ_R is the optimal (reference) slip ratio. This controller in Fig. 2.6 requires slip ratio reference adaptation to generate the optimal slip ratio, as will be discussed in Section 2.6. Accurate estimates of the wheelset slip ratios are needed, as will be discussed in Section 2.7. Anti-windup is needed to gradually reduce the reactive torque if the slip ratio is not larger than the optimal slip ratio [9]. PI control using slip ratio inputs is attractive because it is simple from a dynamic point of view as it is essentially a wheelset speed controller, and the response has fewer oscillations compared to controllers depending on axle accelerations [8].

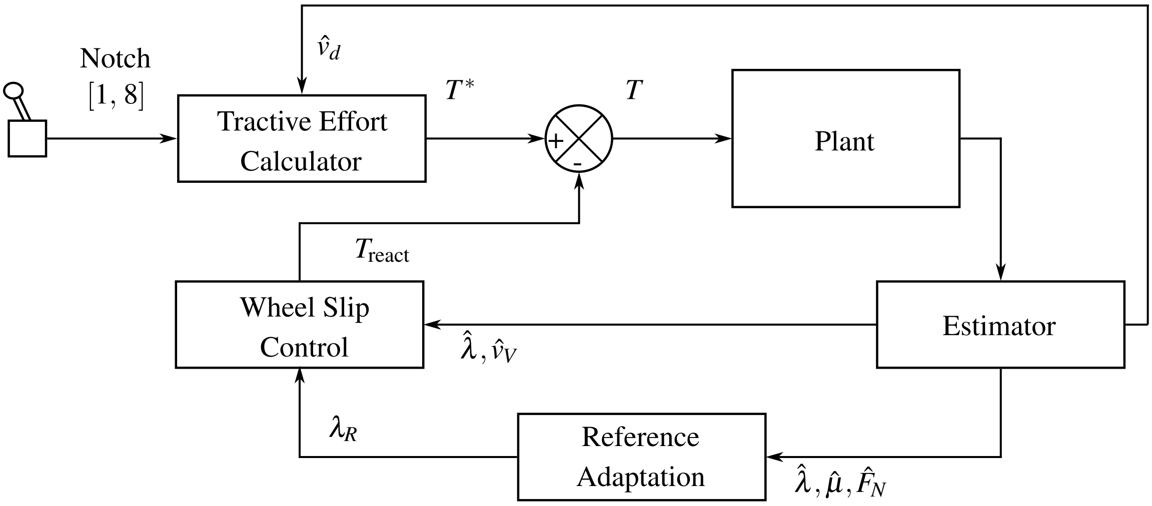

Figure 2.6. Slip control using slip ratios as inputs. Adapted from [9], © 2018 IEEE.

Alternative PI control schemes include using the derivative of the adhesion coefficient with respect to the slip velocity (reaches the maximum adhesion point where the derivative is zero) [27] or using a constant dissipated power setpoint (adhesion force multiplied by the slip velocity) [3], but these methods are more susceptible to measurement noise and estimation inaccuracies.

2.5.6 Sliding Mode Control

PI controllers are typically tuned for a specific linear model that may make them poorly suited to variable wheel-rail conditions [9]. Sliding mode control (SMC) is characterised by a switching control action as the system crosses a particular manifold (sliding surface) in the state space. The state trajectories should stay on the sliding surface once it is reached [15]. SMC is an attractive alternative to PI controllers since it improves robustness against model uncertainties [9, 15]. Due to time delays and hardware limitations, it is impossible to actuate the control infinitely fast in practice. Therefore, SMC can lead to high-frequency oscillation or chattering [8].

A sliding mode wheel slip controller has the same structure (same inputs and outputs) as the PI controller, as illustrated in Fig. 2.6. It requires slip ratio reference adaptation [15]. The sliding surface, s, could be chosen as:

$$s = \lambda - \lambda_R, \tag{2.16}$$

where the reactive torque is increased if $s > 0$ and decreased if $s < 0$. To suppress chattering, the switching surface could be replaced with:

$$f(s) = \frac{s}{|s| + \delta}, \tag{2.17}$$

where $\delta > 0$ [15].

In [9], an integral sliding mode is used to compensate and estimate the perturbations, resulting in reduced chattering. In an experiment with a sport utility vehicle under low adhesion conditions, this method reduced the braking distance by 31% compared to a rule based controller, and by 7% compared to a PI controller

2.5.7 Advanced Controllers

Similar to rule-based and fuzzy-logic controllers, neural network controllers are discrete modulating controllers. Neural network controllers use test data to train the system to approximate the non-linearities, as opposed to tuning the rules and membership functions in rule-based controllers. The main drawback is that they require a large set of training data to achieve good robustness and performance [8].

Advanced continuous controllers include linear quadratic regulators (LQR), classical robust ($\mathcal{H}^\infty$) control, and MPC. LQR methods are sensitive to modelling errors [8]. Classical robust control deals with uncertainty explicitly to achieve robust performance [8], but finding an optimal $\mathcal{H}^\infty$ controller is theoretically and numerically complicated [28]. Fixed longitudinal slip stiffness is generally assumed for $\mathcal{H}^\infty$ controllers, which makes it challenging to design an optimal ($\mathcal{H}^\infty$) controller [11].

MPC offers better noise and disturbance rejection than LQR, but its computational burden is high [8]. A case study of a non-linear MPC is presented in [8], in which the controller can recover from a drop in friction conditions 50% faster than a rule-based controller. For electric vehicles, the implementation time step has a more significant impact on the performance of the controller than the selected control method [11]. A possible solution is using an explicit non-linear MPC, which requires a fraction of the computing time [11].

The possible performance and robustness improvements these advanced controllers offer warrant further investigation. Still, the main challenge in slip control is the uncertainty due to the unknown adhesion conditions, the non-linear wheel-surface dynamics, and the difficulty in obtaining the slip ratio accurately. Therefore, this dissertation prioritises reducing the parameter uncertainty related to slip control over optimising the controller.

2.6 REFERENCE SLIP RATIO ADAPTATION

While advanced controllers may improve reference tracking and robustness against model variabilities and non-linearity, they still depend on finding the optimal slip ratio reference (maximum adhesion), which is challenging. Slip controllers are highly sensitive to setpoint selection [8].

The ideal adhesion characteristic curve is smooth and unimodal, but in reality, the curve has a certain width due to the inherent non-linearities and the unpredictable external environment [12]. A setpoint adaptation strategy based on the rail conditions is needed [8].

2.6.1 Constant Reference and Pseudostatic Curve References

In most automotive applications, a constant slip ratio reference is used [9,21]. An improvement thereon is using a pseudo-static curve to calculate the reference wheel slip corresponding to the maximum adhesion coefficients at different velocities [15]. The drawback of this method is that the pseudo-static curve is calculated for specific friction conditions, meaning that the generated reference will not be optimal for all conditions. Multiple curves corresponding to different adhesion conditions could be used, but fast detection of the adhesion level is not trivial.

2.6.2 Fuzzy Logic Reference Adaptation

A slip ratio reference updating rule is given:

$$\lambda_R^k = \lambda_R^{k-1} + \Delta(\dot{\lambda}, \dot{\mu}), \tag{2.18}$$

where $\Delta(\dot{\lambda}, \dot{\mu})$ is calculated using fuzzy logic. The maximum adhesion coefficient occurs when $d\mu/d\lambda$ is zero. Therefore, $\Delta(\dot{\lambda}, \dot{\mu})$ should be decreased if $d\mu/d\lambda < 0$ and increased if $d\mu/d\lambda > 0$. Fuzzy logic is used to determine the amount by which the reference should be updated based on the magnitude and sign of $d\mu/d\lambda$ [21].

2.6.3 Extremum Seeking

Using estimates for the adhesion coefficient and slip ratio, maximum likelihood estimation could be used to determine the shape of the characteristic curve based on the Burckhardt model, as shown in Section 2.4.1, from which the optimal slip ratio corresponding to the maximum adhesion coefficient can be calculated [12]. Maximum likelihood estimation solves the extremum of the likelihood function, which is constructed using a system model and observed data.

The slope of the characteristic curves, as shown in Fig. 2.5, could be approximated by the partial derivative of the acceleration with respect to the slip ratio [29], or the partial derivative of adhesion force with respect to the slip ratio [9]. A recursive least-squares estimator is used to estimate these partial derivatives [9, 29]. In [9], the linear polynomial:

$$\hat{F}_a = C_1 + C_2\lambda, \tag{2.19}$$

is fitted using a collected set of adhesion force estimates, $\hat{F}_a$, and wheel slip ratios, λ. The sign of the second coefficient, C_2, corresponds to the sign of the gradient:

$$\nabla f = \frac{\partial \hat{F}_a}{\partial \lambda}. \tag{2.20}$$

If a change in the sign of the gradient is observed, a new optimal/reference slip ratio is generated by taking the mean of the last n samples of the slip ratio during a predefined time Δt. This could lead to a rapid variation of the reference wheel slip. Therefore, an additional set of adaptation rules is applied to ensure that the reference value varies slowly. Experimental results showed that this method reduces the braking distance by 2% compared to a preset reference slip ratio [9].

Approximating the slope of the characteristic curve from the partial derivative of the acceleration or adhesion force with respect to the slip ratio has the benefit that it does not need an estimate of the adhesion coefficient. However, if the adhesion coefficient can be estimated accurately, it should enable more accurate extremum seeking of the optimal slip ratio.

2.7 ESTIMATION OF THE SLIP PARAMETERS

As illustrated in Fig. 2.6, the slip control system (consisting of reference adaptation and slip control) depends on estimates of the adhesion coefficients and slip ratios of the wheelsets. The slip ratio estimate is determined by [4]:

$$\lambda = \frac{\omega_d r - v_t}{v_t}, \tag{2.21}$$

where ω_d (rad/s) is the wheelset angular velocity, r (m) is the wheel radius, and v_t (m/s) is the locomotive velocity. The wheelset angular velocities are easily obtainable using encoders on the motor axles (might need noise filtering [8]), but the locomotive velocity, wheel radii and adhesion coefficients are difficult to determine.

Direct estimation of the adhesion coefficients of the wheelsets is theoretically possible, but it is generally calculated by dividing the adhesion force estimate by the normal force:

$$\hat{\mu}_{\text{actual}} = \frac{\hat{F}_a}{\hat{F}_N}. \tag{2.22}$$

2.7.1 Locomotive Velocity

The efficiency of slip control is directly linked to the accuracy of the vehicle velocity estimate [16]. The locomotive velocity is difficult to determine if all the wheelsets are driven [3], especially at low speeds [4]. A simple way to determine the velocity is by removing or reducing the torque on one wheelset and using it as the reference. However, doing so limits the tractive force the locomotive can supply. The locomotive velocity should either be measured directly or estimated.

2.7.1.1 Direct Measurement of the Locomotive Velocity

Many modern locomotives are equipped with a radar, which measures the ground velocity of a locomotive using the Doppler effect [4]. Doppler radars are expensive [16], but their cost is justifiable considering their relative cost compared to a locomotive. A typical accuracy tolerance of a Doppler radar is $0.139-0.194$ m/s. [4]. An alternative is measuring the velocity with a lidar sensor [16], which are as expensive as Doppler radars.

2.7.1.2 Estimation of the Locomotive Velocity

In the automotive application, direct measurement of the vehicle velocity is generally too expensive for mass production. Therefore, the velocity is usually obtained via estimation, which makes slip control highly sensitive to wheel speed measurement noise [8].

In [16] and [14] (automotive ABS application), a wheel-surface adhesion model is combined with a vehicle model to enable the estimation of the vehicle velocity using only measured wheel angular velocities. A single axle wheelset model (similar to a quarter/corner vehicle model in automotive applications [9, 15]) can be used to describe the vehicle dynamics:

$$I\dot{\omega}_d = R\,T_M - r\,F_a \tag{2.23a}$$

$$m_t\dot{v}_t = n\,F_a - F_r, \tag{2.23b}$$

where I ($\mathrm{kg}\cdot\mathrm{m}^2$) is the inertia of the wheelset, T_M ($\mathrm{N}\cdot\mathrm{m}$) is the motor torque, m_t (kg) is the mass of the train, and F_r (N) is the total resistive force. As described in Section 2.4, the adhesion force is a non-linear function that depends on the parameters that describe the wheel-rail adhesion conditions, the wheel surface velocity and locomotive velocity. These methods typically depend on the LuGre adhesion model. If the adhesion parameters are known, the adhesion coefficient becomes dependent only on the measurable wheel velocity and the unknown vehicle velocity. If the normal force is known (could be assumed to be constant), then the adhesion force is dependent only on the wheel velocity and the unknown vehicle velocity:

$$F_a = \mu_{\text{actual}}\{\omega_d, v_t\}\, F_N. \tag{2.24}$$

By substituting (2.24) into (2.23) and assuming that the resistive force is a linear function of the locomotive velocity, the locomotive velocity becomes the only unknown. An unscented or extended Kalman filter can be constructed from this model to determine the locomotive velocity. The estimator must be designed for the nominal adhesion conditions, for which the velocity estimation should be reasonably accurate. This method is expected to produce poor results during significant changes in adhesion conditions due to the assumption of linearity between the resistive force and the locomotive velocity.

In [30], a particle Rao-Blackwellized particle filter is implemented to estimate the velocity of a car based on measurements of the longitudinal and lateral accelerations, wheel angular velocities, steer angle, roll and yaw rates and the GPS position. Without the GPS measurement, not all the states are observable. This approach integrates the acceleration measurement in the absence of the GPS measurement, where the integration drift is intermittently readjusted by using the GPS position measurement. This estimator can produce reliable estimates for reasonable durations during which the GPS signal is lost. Even so, [16] argues that velocity estimation based on GPS measurements should not be relied upon due to the unpredictable availability of the GPS signal. For the non-linear car model, the Rao-Blackwellized particle filter produces more accurate estimates than an unscented Kalman filter [30].

A possible alternative estimation method is based on the measurement of the time shift of the track random excitations (vibration) between two wheelsets of a bogie. The measurements are used in a simplified inverse locomotive model to determine the locomotive velocity [6]. The drawback is that it requires additional measurement equipment that needs to work in a harsh environment [16].

2.7.2 Wheel Radius

The wheel radius is an essential parameter in slip control since it affects the slip ratio estimate, as seen in (2.21), and the adhesion force estimate, which will be discussed later. Having an accurate radius parameter is difficult for two reasons. Firstly, the wear of the wheels will reduce their radius over time. In the case of the 8E locomotive, the nominal radius is 1.220 m, and the wheel is replaced when the radius reaches 1.144 m. Ideally, the radius of each wheel should be updated in the control system at each service interval [4], but in practice, such updates cannot be relied upon. Secondly, due to the conicity of locomotive wheels, the rolling radius alters continuously during operation [31, 32].

To address the first problem, the radii could be updated by logging data during steady-state operation and comparing the velocity measurement with the angular velocities [30]. Such a routine could be used to recalibrate the radii daily [4].

To address the second problem, a possible but non-trivial approach is to include the radii as states that need to be estimated as part of a larger model-based estimator [19, 31]. The preferred approach is to handle the variation in radii as uncertainty that the estimation and control systems have to be able to deal with [30].

2.7.3 Adhesion Coefficient

2.7.3.1 Direct Adhesion Coefficient Estimation

The adhesion coefficient can be determined using noise spectrum analysis of the noise in the contact zone, which depends on the friction conditions [5]. Noise spectrum analysis is complex and requires prior knowledge of some of the track conditions.

During unstable slip, the wheelsets can experience severe vibrations with frequencies in the range of $45-65$ Hz. These vibrations can be used to detect when the friction conditions are low, but they cannot be used as part of a wheel slip detection algorithm [4].

2.7.3.2 Disturbance Observer Adhesion Force Estimation

The adhesion force can be estimated using a disturbance observer, where the adhesion force is seen as a disturbance from the perspective of the motor [27, 33, 34]. From (2.23), a simple observer given in the Laplace domain is:

$$\hat{F}_a = \frac{a}{s+a}\frac{1}{r}(RT_M - I\dot{\omega}_d), \tag{2.25}$$

where a controls the disturbance observer pole [27] that acts as a filter for the measurement noise of the motor torque and wheel angular rate. This observer is based on a simple model of the locomotive, which does not take into account bogie vibration. A second-order observer is proposed in [33] to account for the first resonant frequency of the bogie dynamics. An alternative is extending the observer to estimate both the adhesion force and the wheel angular rate [34].

2.7.3.3 Model-Based Adhesion Force Estimation

The benefit of using a Kalman filter is that the estimator gains are determined from process uncertainty and measurement noise levels instead of choosing an observer pole. It should produce a more optimal estimator.

2.7.3.3.1 Estimation Based on a Wheelset Model

A locomotive wheelset consists of a motor, pinion, gear wheel, and two wheels. These could be combined in a five-mass model where the masses are connected by shafts represented by their elasticity and damping values [22]. Typically, the motor torque is known (provided by the motor control system), and its angular rate is measured with an encoder. If additional sensors are not added, this model cannot produce an observable estimator.

An observable estimator can be produced using a two-mass model, where the motor forms one mass and the pinion, gear wheel and single wheel form the second mass [3, 22]. This model preserves the most significant dynamics of the five-mass model. The vibrations in a wheelset will typically contain a lower frequency component (around 18 Hz) and a higher frequency component (around 61 Hz). The two-mass model preserves the lower frequency dynamics of the wheelset [22].

2.7.3.3.2 Estimation Based on a Locomotive Model

An additional benefit of using a Kalman filter is that it is relatively simple to extend the model to include more of the relevant dynamics, given that sufficient measurements are available to ensure that the estimator is observable. A model-based approach where the adhesion forces are estimated, and the velocity measurement noises are filtered would be beneficial. This requires a model that includes much of the dynamics of the locomotive.

This approach has been adopted in condition monitoring applications for detecting low adhesion. A model-based estimator that includes the lateral dynamics of the vehicle body and the lateral and yaw degrees of freedom of the bogie and wheelsets is used in [13, 17, 19, 32, 35] to estimate the lateral adhesion forces. The degrees of freedom were chosen based on the dynamics that capture the significant responses to track irregularities. Onboard real-time estimation of the adhesion level should be possible if changes in these running dynamics can be observed [32].

The adhesion forces were estimated with a Kalman-Bucy filter, where the estimation model is a rigid body system floating on a series of contact forces [19]. The estimator is constructed by including the adhesion forces as states, assuming their derivates are zero, and attributing significant uncertainty to these states in the noise covariance matrix. This means that no dynamic understanding of the creep forces and gravitational stiffness are inherent in the estimation model [35], which produces a linear estimator model.

The model used in these studies focused on estimating lateral forces and did not consider longitudinal adhesion forces. Therefore, it cannot be used directly, but it illustrates that including the relevant locomotive dynamics in the model yields good estimation.

2.7.4 Normal Force Estimate

The normal force can be assumed to be constant [14, 16], but longitudinal acceleration will cause the normal force distribution to change, as explained in Section 2.5.2. Load-sensing technology could measure the normal force, but this is yet to be a commercialised solution [8].

In the automotive application, the normal force of the rear axle, F_{Nr} (N), can be estimated by [34]:

$$F_{Nr} = -m\frac{H_{\text{COG}}}{L}(a_x \cos\theta_v + a_z \sin\theta_v) - m\frac{L_r}{L}(a_x \sin\theta_v + a_z \cos\theta_v), \tag{2.26}$$

where m (kg) is the mass of the vehicle, H_{COG} (m) is the height of the centre of gravity (COG), L_r (m) is the longitudinal distance from the rear axle to the COG, L (m) is the distance between the axles, a_x and a_z (m/s) are the measured vehicle longitudinal and vertical (including gravitational) accelerations respectively, and (θ_v) (rad) is the pitch angle.

2.8 CONCLUSION

Slip control is difficult due to uncertainty, such as the unknown adhesion conditions, the non-linear wheel-surface dynamics, and the difficulty in accurately obtaining the slip ratio. Therefore, slip control has been primarily implemented with discrete controllers such as rule-based and fuzzy logic. Some studies have shown that fuzzy logic performs better than PI controllers with constant gains [10]. However, it is expected that if the uncertainty in the system can be reduced using an appropriate estimator, it will enable continuous controllers to produce superior performance.

Most continuous slip controllers use slip ratio as an input, which is simple from a dynamic point of view, and the response has fewer oscillations compared to controllers depending on axle accelerations [8]. Since the optimal slip ratio corresponding to the maximum adhesion coefficient is unknown and changes with the locomotive velocity, wheel load and adhesion conditions, these control systems require slip ratio reference adaptation. Many automotive applications use constant slip ratio references, but it has been found that dynamically adapting the reference achieves better performance [9]. The best reference adaptation is expected to be achieved by using the slip ratios and the estimated adhesion coefficients as inputs. Therefore, these are the important parameters for slip control.

The locomotive velocity and wheel radii need to be determined to calculate the slip ratios. The locomotive velocity is difficult to determine if all the wheelsets are driven. The most reliable method is using Doppler radars and estimation based on the longitudinal acceleration and GPS position measurement may be feasible. The wheel radii are difficult to estimate, but assuming they remain constant will introduce estimation errors. The introduced errors may be tolerable if the slip controllers are sufficiently robust.

The adhesion coefficient estimate can theoretically be determined directly, but it is generally calculated by dividing the adhesion force estimate by the normal force estimate. The adhesion force can be estimated reliably using a model-based approach where the dynamics of the wheelset are captured. A separate estimator should be able to estimate the normal forces.

A benefit of using a Kalman filter is that it is relatively simple to extend the model to include more of the relevant dynamics. This has been demonstrated for condition monitoring, where the lateral dynamics of the vehicle body and the lateral and yaw degrees of freedom of the bogie and wheelsets are used to estimate the lateral adhesion forces. It is believed that a similar approach should be possible where the relevant dynamics are captured to produce estimates of the locomotive velocity, wheelset angular rates, adhesion forces, and normal forces. The slip ratio and adhesion coefficient could be calculated from these parameters for each wheelset. As far as the author is aware, an estimator that includes all the mentioned dynamics is not yet reported in literature.

CHAPTER 3 SIMULATION MODEL

3.1 CHAPTER OVERVIEW

This chapter presents the development of a simulation model with which the estimator and slip controller can be tested. Section 3.2 investigates which dynamics to include in the simulation model and reviews various modelling approaches. Section 3.3 gives an overview of the different parts from which the simulation model is constructed, such as the Newtonian dynamics, wheel-rail mechanics, and traction system. In Section 3.4, the locomotive model is developed to include the relevant dynamics. The wagons model is given in Section 3.5. The simulation model combines a locomotive model and a simple wagon model to model the coupler force, as described in Section 3.6. The external forces to the locomotive, including the coupler force, wheel-rail adhesion forces, and motor torques, are described in Section 3.7. In Section 3.8, the simulation model is used in a simulation to show that the relevant dynamics are modelled. This chapter is concluded in Section 3.9.

3.2 MODELLING APPROACH

The dynamics of a locomotive are modelled using wheel-rail contact and Newtonian mechanics. The wheel-rail contact mechanics of locomotives are generally modelled using the Polach model, as described in Section 2.4.3.

A linearised railway vehicle model could be well over 100th order [36]. Such models are helpful for design and validation, but using such complex models in model-based filter or estimator design is impractical [6]. Many studies have a simple modelling approach for developing slip controllers and use real-world experiments for performance validation [6, 9, 24, 30, 34]. While all controllers should eventually be tested in practice, doing so is often tedious, time-consuming, and expensive [2]. A sufficiently sophisticated simulation model, including the dynamics of the locomotive that are most relevant to slip control, provides a platform to test and iterate the controllers quickly.

As shown in Section 2.4, the adhesion force is the realised (or actual) adhesion coefficient multiplied by the normal force ($F_a = \mu_{\text{actual}} F_N$). The adhesion coefficient is dependent on the track conditions. Under constant track conditions, it varies only with a change in wheel load and creep/slip ratio (slip velocity divided by the locomotive velocity). Therefore, the normal forces, wheel velocities, and locomotive velocity should be modelled accurately to ensure the model produces realistic adhesion coefficients.

3.2.1 Single Axle Wheelset Model

The simplest model found in literature is a single axle wheelset model (similar to a quarter/corner vehicle model in automotive applications), as described in Section 2.7.1.2. It is often used in simulation to test slip control [15, 21, 27, 33], estimation [14, 16], and slip ratio reference adaptation [15, 21, 29]. In these studies, a simple model is sufficient to test a specific controller or algorithm. However, these studies do not present their results as conclusive evidence that their methods will work in practice. A limitation of this model is that the integrity of the locomotive and interaction among the different axles are ignored [2].

3.2.2 Longitudinal, Vertical, and Pitch Dynamics

The normal forces are dependent on the pitch dynamics. Unstable slip in the front wheelset may result in subsequent slip in the other wheelsets due to the normal force redistribution caused by the sudden change in acceleration [23]. The pitch dynamics, including the suspension forces, should be modelled to ensure that the normal force distribution is accurately modelled.

In [10], a 2D model is presented, including the longitudinal, vertical, and pitch dynamics, resulting in 21 degrees of freedom. The locomotive body and bogies are modelled as independent bodies connected through the suspensions modelled as spring and damper elements. It is assumed that there is no deflection in the locomotive body and bogies, all masses on the locomotive are constant, pitch angles are small, i.e. $\sin\theta \approx \theta$ where θ is a pitch angle, and friction in the locomotive is negligible. Their simulation results contain oscillations in the tractive force due to the oscillations in the normal force [10]. Without modelling the vertical and pitch dynamics, the robustness of the controllers cannot be tested against these oscillations.

Such 2D models have precedence in the automotive industry. In [34], a bicycle model (simplified lateral and yaw dynamics) is used to calculate the lateral adhesion force of a car while taking into consideration the steering angle, a pitch-plane model to calculate the front and rear normal forces, and a roll-plane model to calculate the normal forces of the left and right wheels.

3.2.3 Wheelset Rotational Dynamics

Although the 2D pitch-plane model in [10] provides more insight than a single-axle wheelset model, it has a simple model for the wheelset:

$$I_w \dot{\omega}_w = T_M - rF_a \tag{3.1}$$

where I_w is the total wheelset inertia and ω_w is the angular rate. Such a simple model neglects torsional vibration within the wheelsets, which can occur during unstable slip due to the non-rigid wheelset axles. Therefore, the rotational dynamics of the simulation model should differentiate between the angular rates and adhesion forces of the left and right wheels. Torsional vibration can cause damage to the wheels and should be avoided.

As mentioned in Section 2.7.3.3.1, [22] presents a five-mass wheelset model. The pinion and gear wheel are lumped together. Axles connect the motor to the pinion and from each wheel to the gear wheel. The axles are represented as stiffness and damping components, but their inertias are lumped with the mentioned masses. This wheelset model provides higher accuracy, where the oscillations caused by the non-stiff wheelset during unstable slip are captured [22].

3.2.4 Lateral, Yaw, and Roll Dynamics

Lateral slip will cause a decrease in both the lateral and longitudinal adhesion force [37]. This dissertation is concerned with maximising the longitudinal adhesion force. If the simulation model includes enough variability to cause sudden decreases in the longitudinal adhesion force (such as a drop in the adhesion conditions), including the lateral adhesion forces is redundant. However, this may not be true when a locomotive travels along a curve, where the lateral dynamics may have large variability.

As mentioned in Section 2.7.3.3.2, a yaw-plane model is used to estimate the lateral adhesion forces to detect low adhesion for condition monitoring. At first, a half-vehicle model was used to simulate and test the estimators [19], but later, a full-length model was used in simulation to test the revised estimator [17]. While their model is not relevant for testing longitudinal slip and estimation, the approach to build a sufficiently complex simulation model containing only the most pertinent dynamics to test the estimator is useful.

A single motor controls the wheels in a wheelset. Therefore, the sum of the wheel adhesion forces is important, and the difference in normal forces between the wheelset wheels, dictated by the roll dynamics, is less relevant for slip control.

Including the lateral, yaw, and roll dynamics in addition to the required longitudinal, vertical, and pitch dynamics dramatically increases the complexity of the model. At such a high complexity level, dedicated multi-body software, such as VAMPIRE or VI-RAIL, should be used [2, 4]. While the software packages can solve and simulate the dynamics efficiently, they require accurate models of the geometry and mass properties of all the components imported from CAD models or experimentally determined. In the context of studying slip control, such high-fidelity models are not needed if it can be ensured that the simpler model that is used contains and accurately models the most relevant dynamics.

3.2.5 Train Longitudinal Dynamics

Simulating the longitudinal dynamics of a locomotive in operation accurately is difficult because it requires modelling of the train as a whole (wagons and possibly additional locomotives) [26]. The longitudinal dynamics depend on the locomotive traction and braking inputs, track topography and curvature, rolling-stock and bogie characteristics, and the relative interactions between the vehicles [4, 7]. The relative motions depend on the couplers, which can be modelled by spring and damper connections with "free slack" due to the coupling air gap [7]. The non-linearities introduced by the slack and the high stiffness of couplers may cause numerical instability during simulation [4].

The longitudinal dynamics are relevant to studies investigating driver comfort of passenger trains, energy optimisation, and equipment failures or derailments [4]. Energy optimisation studies deal with managing the power level of a locomotive for the duration of its journey. Dynamics such as changes in the rail angle are essential for the overall power consumption [38], but the high-frequency dynamics, such as the relative vehicle interactions, are less relevant. This is illustrated in [38], where the train is modelled as a point mass. In the context of derailments, it was found that the in-train forces of long and heavy trains may result in significant forces on the locomotive coupler, impacting the lateral, vertical and pitch dynamics of the locomotive [4]. If these forces become too large, they can affect vehicle stability by causing wheel unloading [4]. The vertical and pitch dynamics are important for investigating slip control. Accurate modelling of the in-train forces is unnecessary, but it is essential to model the forces on the coupler comparable to what could be expected in practice.

3.2.6 Dynamics Included in the Final Model

Choosing the dynamics to include in the simulation model is not trivial. Based on the considerations discussed above, it can be concluded that a pitch-plane model similar to [10], as mentioned in Section 3.2.2, is needed. To ensure that the wheelset oscillations and possible torsional vibrations are modelled, the five mass model of [22], described in Section 3.2.3, should be used to model each wheelset. Modelling the full longitudinal dynamics of the train is not needed since the in-train forces are not relevant to this dissertation. However, a realistic coupler force can be modelled by using a single axle wheelset model, as described in Section 3.2.1, for all of the wagons, and connecting it to the locomotive through a coupler with stiffness and damping.

While the model developed below does not include all the locomotive dynamics, it is expected to capture the most significant dynamics for subsequent estimator and control design. A similar approach is followed in [37], where a passenger aircraft is modelled to aid braking control design. The model of the aircraft body is a 6-degree-of-freedom rigid body, the vertical suspension of the wheels is modelled, and the wheel contact dynamics are modelled in detail. Even though the combined model remains relatively simple, comparing it to a high-fidelity model showed strong correlation (maximum of 9% mismatch) of the oscillating vertical and longitudinal dynamics [37].

3.3 SIMULATION MODEL OVERVIEW

The simulation model for the diesel freight locomotive with Bo-Bo bogies (two wheelsets per bogie), as shown in Fig. 1.1, is constructed using a novel combination of the modelling approaches discussed in Section 3.2. A unique approach is taken to the train longitudinal dynamics by connecting the locomotive model to a simple wagon model. Fig. 3.1 shows the main components of the simulation model. Throughout the modelling, the numerical subscripts ij indicate the front, $i = 1$, or rear, $i = 2$, bogies and the front, $j = 1$, or rear, $j = 2$, wheelsets of that bogie. The numbers in brackets indicate the section that describes the specific part of the model.

3.4 LOCOMOTIVE MODEL

The chosen simulation model includes the longitudinal, vertical, pitch and wheelset rotational dynamics, as illustrated in Fig. 3.2. The rail dynamics are ignored, and it is assumed that the wheels never lose contact with the rails, i.e., the wheelsets do not have vertical displacement [4, 19]. Fig. 3.3 illustrates the forces acting on a bogie.

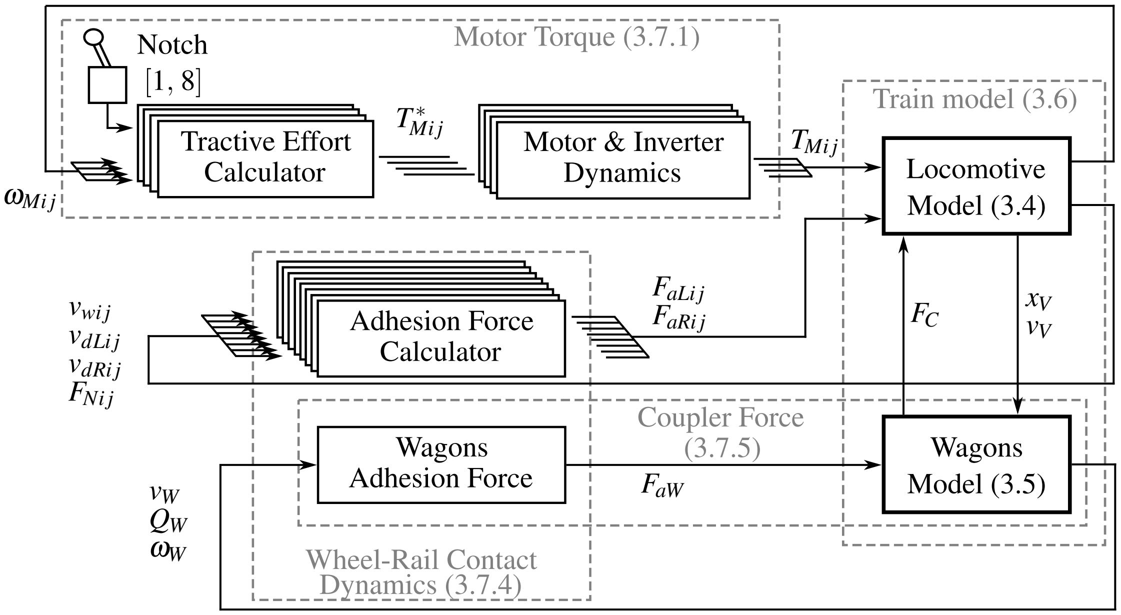

Figure 3.1. Simplified simulation model overview.

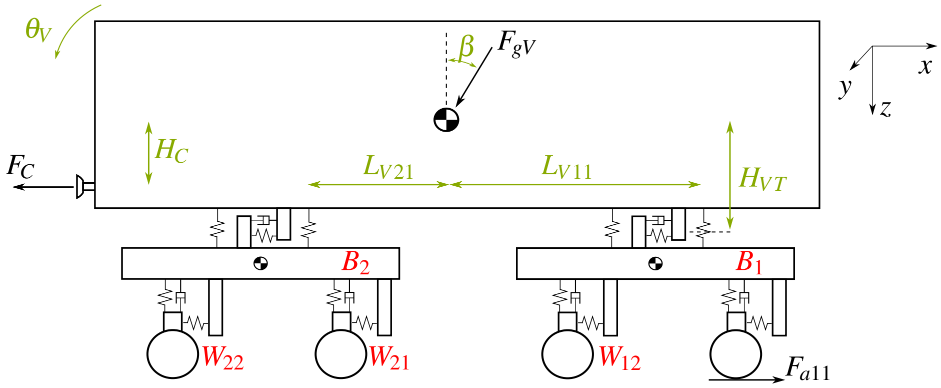

Figure 3.2. Locomotive model. (Front (B_1) and rear (B_2) bogie and the the front (W_{i1}) and rear (W_{i2}) wheelset of each bogie indicated.)

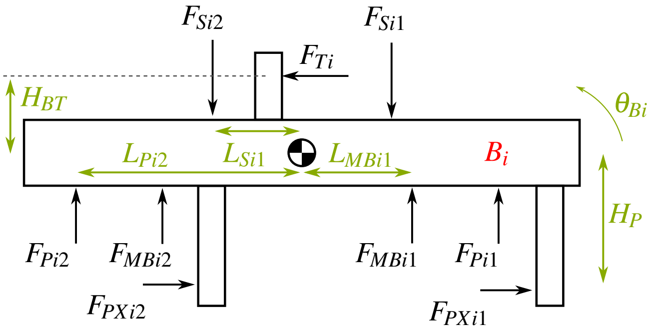

Figure 3.3. Forces on a bogie.

The dynamics of the locomotive can be described in matrix form by:

$$\boldsymbol{M}_q\ddot{\boldsymbol{q}}+\boldsymbol{C}_q\dot{\boldsymbol{q}}+\boldsymbol{K}_q\boldsymbol{q}=\boldsymbol{f}, \tag{3.2}$$

where $\boldsymbol{M}_q$, $\boldsymbol{C}_q$ and $\boldsymbol{K}_q$ are the mass, damping and stiffness matrices, $\boldsymbol{q}$ is the displacement vector and $\boldsymbol{f}$ is the interface force vector [4]. By choosing the state vector as:

$$\boldsymbol{x}=\begin{bmatrix}\boldsymbol{q}\\ \dot{\boldsymbol{q}}\end{bmatrix}, \tag{3.3}$$

the dynamics can be represented in state-space form [4, 10] as:

$$\dot{\boldsymbol{x}}=\boldsymbol{A}\boldsymbol{x}+\boldsymbol{B}\boldsymbol{f}, \tag{3.4}$$

with:

$$\boldsymbol{A}=\begin{bmatrix}\boldsymbol{0} & \boldsymbol{I}\\ -\boldsymbol{M}_q^{-1}\boldsymbol{K}_q & -\boldsymbol{M}_q^{-1}\boldsymbol{C}_q\end{bmatrix},\quad \boldsymbol{B}=\begin{bmatrix}\boldsymbol{0}\\ \boldsymbol{M}_q^{-1}\end{bmatrix}. \tag{3.5}$$

3.4.1 Longitudinal Dynamics

The longitudinal dynamics of the locomotive are:

$$m_V\ddot{x}_V=F_{T1}+F_{T2}-F_C\cos\theta_V-F_{gV}\sin\beta \tag{3.6a}$$

$$m_{Bi}\ddot{x}_{Bi}=F_{PXi1}+F_{PXi2}-F_{Ti}-F_{gBi}\sin\beta \tag{3.6b}$$

$$m_{Wij}\ddot{x}_{Wij}=F_{aLij}+F_{aRij}-F_{PXij}-F_{gWij}\sin\beta, \tag{3.6c}$$

where m_V, m_{Bi} and m_{Wij} (kg) are the masses of the vehicle body, bogies and wheelsets respectively, x_V, x_{Bi} and x_{Wij} (m) are the locomotive vehicle body, bogie and wheelset longitudinal displacements respectively, F_{Ti} (N) are the traction rod forces, F_{PXij} (N) are the primary suspension longitudinal forces, F_C (N) is the coupler force, F_{aLij} and F_{aRij} (N) are the adhesion forces on the left and right wheels of each wheelset respectively, θ_V (rad) is the vehicle body pitch angle, F_{gV}, F_{gBi} and F_{gWij} (N) are the vehicle body, bogie and wheelset gravitational forces respectively, and β (rad) is the rail incline angle. The aerodynamic drag is assumed to be negligible since the force it introduces will generally be much less than the coupler and gravitational forces.

The longitudinal suspension forces, as shown in Fig. 3.3, are:

$$F_{Ti}=k_{Ti}(x_{Bi}-x_V)+c_{Ti}(\dot{x}_{Bi}-\dot{x}_V) \tag{3.7a}$$

$$F_{PXij}=k_{PXij}(x_{Wij}-x_{Bi}), \tag{3.7b}$$

where k_{Ti} (N/m) and c_{Ti} (N·s/m) are the traction rod stiffness and damping coefficients respectively, k_{PXij} (N/m) are the primary suspension longitudinal stiffness coefficients, and x_V, x_{Bi} and x_{Wij} (m) are the locomotive vehicle body, bogie and wheelset longitudinal displacements respectively.

The mass, damping and stiffness matrices of the longitudinal dynamics are derived by choosing its displacement vector as:

$$\boldsymbol{q}_{\text{long}} = \begin{bmatrix} x_V & x_{B1} & x_{W11} & x_{W12} & x_{B2} & x_{W21} & x_{W22} \end{bmatrix}^T, \tag{3.8}$$

such that:

$$\boldsymbol{M}_{\text{long}} = \text{diag}\begin{bmatrix} m_V & m_{B1} & m_{W11} & m_{W12} & m_{B2} & m_{W21} & m_{W22} \end{bmatrix} \tag{3.9}$$

$$\boldsymbol{C}_{\text{long}} = \begin{bmatrix} c_{T1}+c_{T2} & -c_{T1} & 0 & 0 & -c_{T2} & 0 & 0 \\ -c_{T1} & c_{T1} & 0 & 0 & 0 & 0 & 0 \\ 0 & 0 & 0 & 0 & 0 & 0 & 0 \\ 0 & 0 & 0 & 0 & 0 & 0 & 0 \\ -c_{T2} & 0 & 0 & 0 & c_{T2} & 0 & 0 \\ 0 & 0 & 0 & 0 & 0 & 0 & 0 \\ 0 & 0 & 0 & 0 & 0 & 0 & 0 \end{bmatrix} \tag{3.10}$$

$$\boldsymbol{K}_{\text{long}} = \begin{bmatrix} k_{T1}+k_{T2} & -k_{T1} & 0 & 0 & -k_{T2} & 0 & 0 \\ -k_{T1} & k_{PX11}+k_{PX12}+k_{T1} & -k_{PX11} & -k_{PX12} & 0 & 0 & 0 \\ 0 & -k_{PX11} & k_{PX11} & 0 & 0 & 0 & 0 \\ 0 & -k_{PX12} & 0 & k_{PX12} & 0 & 0 & 0 \\ -k_{T2} & 0 & 0 & 0 & k_{PX21}+k_{PX22}+k_{T2} & -k_{PX21} & -k_{PX22} \\ 0 & 0 & 0 & 0 & -k_{PX21} & k_{PX21} & 0 \\ 0 & 0 & 0 & 0 & -k_{PX22} & 0 & k_{PX22} \end{bmatrix} \tag{3.11}$$

$$\boldsymbol{f}_{\text{long}} = \begin{bmatrix} -F_C\cos\theta_V - F_{gV}\sin\beta \\ -F_{gB1}\sin\beta \\ F_{aL11}+F_{aR11}-F_{gW11}\sin\beta \\ F_{aL12}+F_{aR12}-F_{gW12}\sin\beta \\ -F_{gB2}\sin\beta \\ F_{aL21}+F_{aR21}-F_{gW21}\sin\beta \\ F_{aL22}+F_{aR22}-F_{gW22}\sin\beta \end{bmatrix}. \tag{3.12}$$

3.4.2 Vertical Dynamics

The vertical dynamics are:

$$m_V\ddot{z}_V = -F_{S11} - F_{S12} - F_{S21} - F_{S22} - F_C\sin\theta_V + F_{gV}\cos\beta \tag{3.13a}$$

$$m_{Bi}\ddot{z}_{Bi} = -F_{Pi1} - F_{Pi2} - F_{MBi1} - F_{MBi2} + F_{Si1} + F_{Si2} + F_{gBi}\cos\beta, \tag{3.13b}$$

where z_V and z_{Bi} (m) are the vehicle body and bogie vertical displacements respectively, F_{Pij} (N) describes the vertical primary suspension forces, F_{Sij} (N) describes the secondary suspension forces, and F_{MB} (N) are the forces from the motor housings to the bogies.

The vertical primary suspension forces are:

$$F_{Pij} = k_{Pij}(z_{Bi} \mp L_{Pij}\theta_{Bi}) + c_{Pij}(\dot{z}_{Bi} \mp L_{Pij}\dot{\theta}_{Bi}), \tag{3.14}$$

where k_{Pij} (N/m) and c_{Pij} (N $\cdot$ s/m) are the primary suspension vertical stiffness and damping coefficients, respectively, and z_{Bi} (m) are the bogie vertical displacements. The signs are negative for the front wheelsets and positive for the rear wheelsets of each bogie. The secondary suspension forces are:

$$F_{Sij} = k_{Sij}(z_V - z_{Bi} \mp L_{Vij}\theta_V \pm L_{Sij}\theta_{Bi}) + c_{Sij}(\dot{z}_V - \dot{z}_{Bi} \mp L_{Vij}\dot{\theta}_V \pm L_{Sij}\dot{\theta}_{Bi}) \tag{3.15}$$

where k_{Sij} (N/m) and c_{Sij} (N $\cdot$ s/m) are the secondary suspension vertical stiffness and damping coefficients, respectively, and z_V (m) is the vehicle body vertical displacement. The signs preceding the L_{Vij} terms are negative for the front bogie and positive for the rear bogie. The signs preceding the L_{Sij} terms are positive for the front wheelsets and negative for the rear wheelsets of each bogie. Although the secondary suspension does not have dampers, a damping coefficient is included in the model to account for natural damping in the system.

The displacement and interface force vectors are:

$$\boldsymbol{q}_{\text{vert}} = \begin{bmatrix} z_V & z_{B1} & z_{B2} & \theta_V & \theta_{B1} & \theta_{B2} \end{bmatrix}^T \tag{3.16}$$

$$\boldsymbol{f}_{\text{vert}} = \begin{bmatrix} -F_C\sin\theta_V + F_{gV}\cos\beta \\ F_{gB1}\cos\beta - F_{MB11} - F_{MB12} \\ F_{gB2}\cos\beta - F_{MB21} - F_{MB22} \end{bmatrix}. \tag{3.17}$$

Note that there are three vertical equations, while the displacement vector has six elements. Therefore, the mass, stiffness and damping matrix dimensions are 3 × 6. The mass matrix is:

$$\boldsymbol{M}_{\text{vert}} = \begin{bmatrix} \text{diag}[m_V \quad m_{B1} \quad m_{B2}] & 0_{3\times 3} \end{bmatrix}. \tag{3.18}$$

where $0_{p\times q}$ is a matrix of zeros with p rows and q columns and diag$[\cdot]$ is a square matrix with the contained elements on its diagonal. The stiffness and damping matrices are given in Appendix A.2.

3.4.3 Pitch Dynamics

The pitch dynamics are:

$$\begin{aligned} I_V\ddot{\theta}_V &= L_{V11}F_{S11} + L_{V12}F_{S12} - L_{V21}F_{S21} - L_{V22}F_{S22} \\ &\quad + H_{VT}F_{T1} + H_{VT}F_{T2} - H_CF_C\cos\theta_V - L_CF_C\sin\theta_V \qquad (3.19a) \\ I_{Bi}\ddot{\theta}_{Bi} &= L_{Pi1}F_{Pi1} - L_{Pi2}F_{Pi2} - L_{Si1}F_{Si1} + L_{Si2}F_{Si2} \\ &\quad + L_{MBi1}F_{MBi1} - L_{MBi2}F_{MBi2} + H_P(F_{PXi1} + F_{PXi2}) + H_{BT}F_{Ti}, \qquad (3.19b) \end{aligned}$$

where I_V and I_{Bi} ($\mathrm{kg}\cdot\mathrm{m}^2$) are the pitch moment of inertias of the vehicle body and bogies respectively, θ_V and θ_{Bi} (rad) are the pitch angles of the vehicle body and bogies respectively, and the H and L (m) parameters are the geometric heights and lengths as indicated in the figures.

The displacement vector, mass matrix, and interface force vector are:

$$\boldsymbol{q}_{\text{pitch}} = \begin{bmatrix} x_V & x_{B1} & x_{W11} & x_{W12} & x_{B2} & x_{W21} & x_{W22} & z_V & z_{B1} & z_{B2} & \theta_V & \theta_{B1} & \theta_{B2} \end{bmatrix}^T \qquad (3.20)$$

$$\boldsymbol{M}_{\text{pitch}} = \begin{bmatrix} 0_{3\times 10} & \mathrm{diag}[I_V \quad I_{B1} \quad I_{B2}] \end{bmatrix} \qquad (3.21)$$

$$\boldsymbol{f}_{\text{pitch}} = \begin{bmatrix} -H_CF_C\cos\theta_V - L_CF_C\sin\theta_V \\ L_{MB11}F_{MB11} - L_{MB12}F_{MB12} \\ L_{MB21}F_{MB21} - L_{MB22}F_{MB22} \end{bmatrix}. \qquad (3.22)$$

The stiffness and damping matrices are given in Appendix A.3.

3.4.4 Wheelset Rotational Dynamics

The wheelset model is illustrated in Fig. 3.4. The wheelset rotational dynamics are:

$$I_L\ddot{\theta}_L = -r_LF_{aL} + c_1(\dot{\theta}_G - \dot{\theta}_L) + k_1(\theta_G - \theta_L) \qquad (3.23a)$$

$$I_R\ddot{\theta}_R = -r_RF_{aR} + c_2(\dot{\theta}_G - \dot{\theta}_R) + k_2(\theta_G - \theta_R) \qquad (3.23b)$$

$$I_M\ddot{\theta}_M = T_M + c_3(R\dot{\theta}_G - \dot{\theta}_M) + k_3(R\theta_G - \theta_M) \qquad (3.23c)$$

$$I_G\ddot{\theta}_G = n_GF_{PG} + c_1(\dot{\theta}_L - \dot{\theta}_G) + k_1(\theta_L - \theta_G) + c_2(\dot{\theta}_R - \dot{\theta}_G) + k_2(\theta_R - \theta_G) \qquad (3.23d)$$

$$I_P\ddot{\theta}_P = -n_PF_{PG} + c_3(\dot{\theta}_M - \dot{\theta}_P) + k_3(\theta_M - \theta_P), \qquad (3.23e)$$

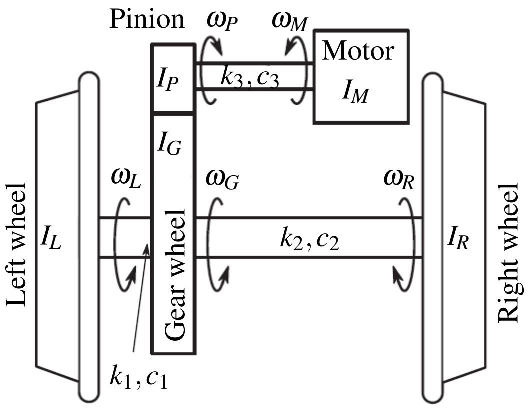

Figure 3.4. Five mass wheelset model. Adapted from [22], © 2018 IEEE.

with $R = \frac{n_G}{n_P} = \frac{\theta_G}{\theta_P}$. By substituting (3.23e) into (3.23d):

$$\begin{aligned}(I_G + R^2 I_P)\ddot{\theta}_G + (c_1 + c_2 + R^2 c_3)\dot{\theta}_G + (k_1 + k_2 + R^2 k_3)\theta_G - c_1\dot{\theta}_L - c_2\dot{\theta}_R - Rc_3\dot{\theta}_M \\ - k_1\theta_L - k_2\theta_R - Rk_3\theta_M = 0, \qquad (3.24)\end{aligned}$$

where I_L, I_R, I_M, I_G and I_P ($\mathrm{kg \cdot m^2}$) are the left wheel, right wheel, motor rotor, gear wheel and pinion moment of inertias respectively, θ_L, θ_R, θ_M, θ_G and θ_P (rad) are the respective angles angles, c_1 & k_1, c_2 & k_2 and c_3 & k_3 are the damping ($\mathrm{N \cdot m \cdot s/rad}$) and stiffness ($\mathrm{N \cdot m/rad}$) coefficients between the left wheel and gear wheel, right wheel and gear wheel, and the motor and pinion respectively, r_L and r_R (m) are the radii from the left and right wheel centres to the wheel-rail contact point respectively, F_{aL} and F_{aR} (N) are the left and right wheel adhesion forces, T_M ($\mathrm{N \cdot m}$) is the motor torque, F_{PG} (N) is the force between the gear wheel and pinion, n_G and n_P (m) are the gear wheel and pinion radii respectively, and R is the gear ratio.

The displacement vector, mass matrix, and interface force vector are:

$$\boldsymbol{q}_{\mathrm{rot}ij} = \begin{bmatrix}\theta_{Lij} & \theta_{Rij} & \theta_{Gij} & \theta_{Mij}\end{bmatrix}^T \qquad (3.25)$$

$$\boldsymbol{M}_{\mathrm{rot}} = \mathrm{diag}\begin{bmatrix}I_L & I_R & I_G + R^2 I_P & I_M\end{bmatrix} \qquad (3.26)$$

$$\boldsymbol{f}_{\mathrm{rot}ij} = \begin{bmatrix}-r_L F_{aLij} \\ -r_R F_{aRij} \\ 0 \\ T_{Mij}\end{bmatrix}. \qquad (3.27)$$

The stiffness and damping matrices are given in Appendix A.4. Each wheelset makes use of the same model (mass, stiffness, and damping matrices), but the variables are specific to a wheelset indicated by the ij subscript.

3.4.5 Consolidated Locomotive Model

Combining the longitudinal, vertical, pitch and rotational dynamics is done by choosing the displacement vector $\boldsymbol{q}$ as:

$$\begin{aligned}\boldsymbol{q} = \Big[& x_V \quad x_{B1} \quad x_{W11} \quad x_{W12} \quad x_{B2} \quad x_{W21} \quad x_{W22} \quad z_V \quad z_{B1} \quad z_{B2} \\ & \ldots \quad \theta_V \quad \theta_{B1} \quad \theta_{B2} \quad \theta_{L11} \quad \theta_{R11} \quad \theta_{G11} \quad \theta_{M11} \quad \theta_{L12} \quad \theta_{R12} \quad \ldots \\ & \theta_{G12} \quad \theta_{M12} \quad \theta_{L21} \quad \theta_{R21} \quad \theta_{G21} \quad \theta_{M21} \quad \theta_{L22} \quad \theta_{R22} \quad \theta_{G22} \quad \theta_{M22} \Big]^T, \end{aligned} \tag{3.28}$$

such that the mass, damping and stiffness matrices are described by:

$$\boldsymbol{X} = \left[\begin{array}{cccccc} \{\boldsymbol{X}_{\text{long}}\}_{7\times7} & 0_{7\times6} & 0_{7\times4} & 0_{7\times4} & 0_{7\times4} & 0_{7\times4} \\ 0_{3\times7} & \{\boldsymbol{X}_{\text{vert}}\}_{3\times6} & 0_{3\times4} & 0_{3\times4} & 0_{3\times4} & 0_{3\times4} \\ \multicolumn{2}{c}{\{\boldsymbol{X}_{\text{pitch}}\}_{3\times13}} & 0_{3\times4} & 0_{3\times4} & 0_{3\times4} & 0_{3\times4} \\ 0_{4\times7} & 0_{4\times6} & \{\boldsymbol{X}_{\text{rot}}\}_{4\times4} & 0_{4\times4} & 0_{4\times4} & 0_{4\times4} \\ 0_{4\times7} & 0_{4\times6} & 0_{4\times4} & \{\boldsymbol{X}_{\text{rot}}\}_{4\times4} & 0_{4\times4} & 0_{4\times4} \\ 0_{4\times7} & 0_{4\times6} & 0_{4\times4} & 0_{4\times4} & \{\boldsymbol{X}_{\text{rot}}\}_{4\times4} & 0_{4\times4} \\ 0_{4\times7} & 0_{4\times6} & 0_{4\times4} & 0_{4\times4} & 0_{4\times4} & \{\boldsymbol{X}_{\text{rot}}\}_{4\times4} \end{array}\right], \tag{3.29}$$

where $\boldsymbol{X}$ is substituted by $\boldsymbol{M}_q$, $\boldsymbol{C}_q$ and $\boldsymbol{K}_q$ for the mass, damping and stiffness matrices respectively. Here, $\{\cdot\}_{p\times q}$ indicates that the contained matrix has p rows and q columns. The interface force vector is:

$$\boldsymbol{f} = \begin{bmatrix} \{\boldsymbol{f}_{\text{long}}\}_{7\times1} \\ \{\boldsymbol{f}_{\text{vert}}\}_{3\times1} \\ \{\boldsymbol{f}_{\text{pitch}}\}_{3\times1} \\ \{\boldsymbol{f}_{\text{rot11}}\}_{4\times1} \\ \{\boldsymbol{f}_{\text{rot12}}\}_{4\times1} \\ \{\boldsymbol{f}_{\text{rot21}}\}_{4\times1} \\ \{\boldsymbol{f}_{\text{rot22}}\}_{4\times1} \end{bmatrix}. \tag{3.30}$$

It should be noted that while the model for each wheelset is the same, but the forces to which they are exposed are not the same, as shown in (3.27) and (3.30).

3.5 WAGONS MODEL

The coupler is modelled as a spring and damper element that connects the wagons to the locomotive. The wagons are modelled using a single axle wheelset model [16, 27], which lumps the inertia of the wheelsets of the wagon together, has the same mass as the wagons and has an adhesion force equal to the sum of the adhesion forces of each wheel. The model is illustrated in Fig. 3.5.

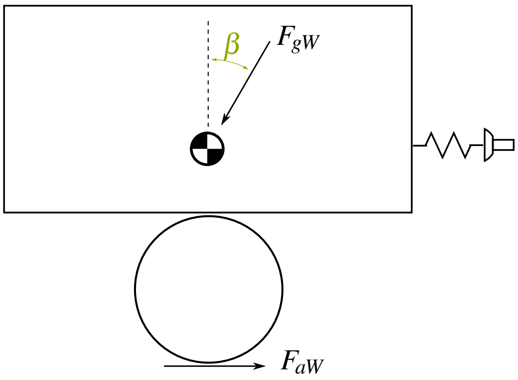

Figure 3.5. Wagons and coupler model.

The dynamics of the wagons are:

$$m_W \ddot{x}_W = F_C + F_{aW} - F_{gW} \sin\beta - F_r \tag{3.31a}$$

$$I_W \dot{\omega}_W = -r_W F_{aW}, \tag{3.31b}$$

where m_W (kg) is the mass of all the wagons of the train, x_W (m) is the displacement of the wagons, F_{gW} (N) is the gravitational force of the wagons, F_r (N) is the rolling resistance, I_W $(\text{kg} \cdot \text{m}^2)$ is sum of the inertias of all the wheelsets of the wagons, ω_W (rad/s) is the angular rate of the wagon wheels, r_W (m) is the average wagon wheel radius, and F_{aW} (N) is the sum of the adhesion forces of each wagon wheel. Note that the adhesion force is in the same direction as defined for the locomotive, but since there is no propulsion in the wagons, this adhesion force will generally be negative.

The coupler force is:

$$F_C = k_C(x_V - x_W) + c_C(v_V - v_W), \tag{3.32}$$

where k_C (N/m) is the coupler stiffness coefficient, c_C (N s/m) is the coupler damping coefficient, and $v_W = \dot{x}_W$ (m/s) is the wagons velocity.

3.6 FULL TRAIN MODEL

The wagons model described in Section 3.5 is combined with the locomotive model in (3.4) described in Section 3.4.5 to produce the full train model, as indicated in Fig. 3.1, by defining the state variable as:

$$\boldsymbol{x}_{\text{Full}} = \begin{bmatrix} \boldsymbol{x}^T & v_W & x_W & \omega_W \end{bmatrix}^T. \tag{3.33}$$

The state matrix of the wagon dynamics in (3.31) and (3.32) is (note that the first and 30th elements of x_{Full} are x_V and v_V, respectively):

$$\boldsymbol{A}_W = \begin{bmatrix} \frac{k_C}{m_W} & 0_{1\times 28} & \frac{c_C}{m_W} & 0_{1\times 28} & -\frac{c_C}{m_W} & -\frac{k_C}{m_W} & 0 \\ 0 & 0_{1\times 28} & 0 & 0_{1\times 28} & 1 & 0 & 0 \\ 0 & 0_{1\times 28} & 0 & 0_{1\times 28} & 0 & 0 & 0 \end{bmatrix}. \tag{3.34}$$

Therefore, the state matrix of the train model is:

$$\boldsymbol{A}_{\text{Full}} = \begin{bmatrix} \{\boldsymbol{A}\}_{58\times 58} & 0_{58\times 3} \\ \multicolumn{2}{c}{\{\boldsymbol{A}_W\}_{3\times 61}} \end{bmatrix}, \tag{3.35}$$

The input matrix of the train model is:

$$\boldsymbol{B}_{\text{Full}} = \begin{bmatrix} \{\boldsymbol{B}\}_{58\times 29} & 0_{58\times 1} & 0_{58\times 1} & 0_{58\times 1} \\ 0_{1\times 29} & \frac{1}{m_W} & 0 & 0 \\ 0_{1\times 29} & 0 & 0 & 0 \\ 0_{1\times 29} & 0 & 0 & \frac{1}{I_W} \end{bmatrix}, \tag{3.36}$$

and the interface force vector is:

$$\boldsymbol{f}_{\text{Full}} = \begin{bmatrix} \{\boldsymbol{f}\}_{29\times 1} \\ F_{aW} - F_{gW}\sin\beta - F_r \\ 0 \\ -r_W F_{aW} \end{bmatrix}. \tag{3.37}$$

3.7 EXTERNAL FORCES

This section describes the computation of the forces in the interface force vector of (3.37).

3.7.1 Motor Torque

Due to the engine ramp-up rate, the rated locomotive power is not immediately available in a diesel locomotive. The diesel engine and alternator can be modelled as a first-order response [4]. However, for this dissertation it is assumed that the engine is constantly running at full speed so that the maximum torque is available at a standstill. Maximum torque under low adhesion conditions is the worst-case scenario under which slip is likely to occur, which the slip controller should be able to handle.

The desired torque of each motor, T^*_{Mij} ($\text{N}\cdot\text{m}$), as shown in Fig. 3.1, is dependent on the selected notch setting and the wheelset speed, as explained in Section 2.3.2.2. Using (2.1) to (2.3), the desired torque for each motor is calculated separately, where the wheel surface velocity is derived from the measured/estimated motor angular velocity:

$$v_{dij} = \frac{r}{R}\omega_{Mij}, \tag{3.38}$$

where v_{dij} (m/s) is the assumed wheelset ij surface velocity, r (m) is the wheel radius, R is the gearbox ratio, and ω_{Mij} (m/s) is the angular velocity of motor ij.

Traction motors are generally controlled using FOC or DTC, producing a fast torque response [1,39]. The motor and inverter dynamics, as shown in Fig. 3.1, can be modelled as a first-order response [4]:

$$T_{Mij} = \frac{1}{\tau_M s + 1} T^*_{Mij}, \tag{3.39}$$

where T_{Mij} (N·m) is the torque produced by motor ij, s is the complex frequency domain Laplace parameter, and τ_M (s) is the inverter and motor time constant.

While electric locomotives fed from overhead cables can rapidly increase their tractive effort, torque rate limits are often imposed on the AC drive systems of diesel locomotives to account for the diesel engine's relatively slow response to the changing power demands [4]. However, such a rate limit is deliberately neglected here so that the worst-case slip can be simulated.

3.7.2 Motor Housing to Bogie Force

The force between the motor housing and the bogie, F_{MBij}, which impacts the vertical dynamics, is derived for any wheelset ij by assuming that the motor housing, as shown in Fig. 3.6 has no pitch, so that the moments around the axle bearings in the motor housing are zero:

$$F_{MBij} = \frac{1}{L_{MP}+L_{MW}} T_{Mij} - \frac{L_{MW}}{L_{MP}+L_{MW}} F_{gMHij} \cos\beta, \tag{3.40}$$

where F_{gMHij} (N) is the gravitational force of the motor and housing, and T_{Mij} (N·m) is the torque from the motor on the housing.

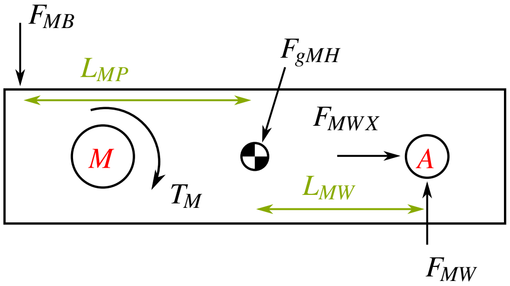

Figure 3.6. Forces on the motor housing.

3.7.3 Normal Forces

The normal forces are not used directly in the interface force vector, but they are needed to calculate the adhesion forces. As mentioned in Section 3.2.4, the normal forces in a wheelset in the simulation model are equal, i.e. $F_{NLij} = F_{NRij} = \frac{1}{2}F_{Nij}$, where F_{NLij} and F_{NRij} (N) are the normal forces of the left and right wheels of wheelset ij, respectively.

To calculate the normal force on the wheelset, as shown in Fig. 3.7, the vertical forces on the motor housing in Fig. 3.6 are considered first (ignoring the ij subscripts for brevity):

$$m_{MH}\ddot{z}_W = F_{MB} + F_{gMH}\cos\beta - F_{MW}, \tag{3.41}$$

where m_{MH} is the mass of the motor and motor housing, F_{MB} is the force from the housing to the bogie, and F_{MW} is the force from the housing to the wheelset. It is assumed that the wheelset never loses contact with the rail and that the changes in the rail angle occur slowly. Therefore, the vertical acceleration of the wheelset, $\ddot{z}_W$, is assumed to be zero. By substituting (3.40) into (3.41) the housing to wheelset force is:

$$F_{MW} = \frac{1}{L_{MP}+L_{MW}}T_M + \frac{L_{MP}}{L_{MP}+L_{MW}}F_{gMH}\cos\beta \tag{3.42}$$

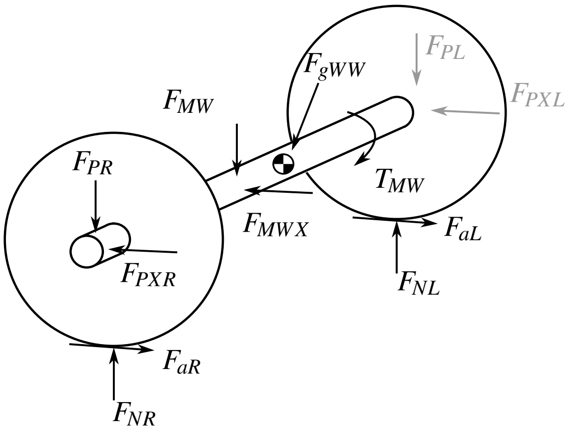

Figure 3.7. Forces on the wheelset.

The normal force on a wheelset is determined from the vertical forces on the wheelset in Fig. 3.7:

$$m_{WW}\ddot{z}_W = F_P + F_{MW} + F_{gWW}\cos\beta - F_N, \tag{3.43}$$

where m_{WW} is the mass of the wheelset without the motor, F_N is the sum of the left and right normal forces (F_{NL} and F_{NL}) on the wheels, F_P is the sum of the left and right vertical primary suspension forces (F_{PR} and F_{PL}), and F_{gWW} is the gravitational force. By substituting (3.42) into (3.43) and assuming that $\ddot{z}_W = 0$, the normal force for any wheelset ij is:

$$F_{Nij} = F_{Pij} + \frac{1}{L_{MP}+L_{MW}}T_{Mij} + (\frac{L_{MP}}{L_{MP}+L_{MW}}F_{gMHij} + F_{gWWij})\cos\beta, \tag{3.44}$$

where F_{Pij} is calculated from (3.14) and T_{Mij} is calculated from (3.39). Additional stacked blocks could be added to Fig. 3.1 to indicate the computation of the normal forces for each wheelset. It was chosen to omit it to prevent overcomplicating the figure.

3.7.4 Wheel-Rail Contact Dynamics

The Polach model, as described in Section 2.4, is used in simulation to determine the adhesion coefficient of each wheel individually (eight locomotive wheels and one wagon wheel). It is summarised as follows:

$$\mu = f_{\text{Polach}}(\{\text{Level}\}, Q, \lambda, v_V), \tag{3.45}$$

where $\{\text{Level}\}$ groups the model parameters k_A, k_S, μ_0, $\frac{\mu_\infty}{\mu_0}$, and B, for the specific adhesion level. The $\{\text{Level}\}$ and Q arguments determine the shape of the surfaces in Fig. 2.4 and the λ and v_V arguments determine the operating point on the surfaces.

3.7.4.1 Locomotive Adhesion Forces

The adhesion coefficients of each left wheel of wheelset ij, μ_{Lji} (μ_{Rji} for the right wheel), of the locomotive are calculated from (3.45) by setting the arguments to:

$$Q = \frac{1}{2} F_{Nij} \tag{3.46a}$$

$$\lambda = (\omega_{Lij} r_L - v_{Wij})/v_{Wij} \tag{3.46b}$$

$$v_V = v_{Wij} = \dot{x}_{Wij} \tag{3.46c}$$

where v_{Wij} (m/s) is the velocity of wheelset ij and $\omega_{Lij} = \dot{\theta}_{Lij}$ (rad/s) is the angular velocity of the left wheel of wheelset ij. Finally, the adhesion force of any wheel is:

$$F_{aLij} = \mu_{Lji} F_{Nij} \tag{3.47a}$$

$$F_{aRij} = \mu_{Rji} F_{Nij}. \tag{3.47b}$$

3.7.4.2 Wagons Adhesion Force

The adhesion coefficient of the wagons, μ_W, is calculated by setting the arguments to:

$$Q = Q_W = m_W\, g \cos\beta / n_W \tag{3.48a}$$

$$\lambda = (r_W\, \omega_W - v_W)/v_W \tag{3.48b}$$

$$v_V = v_W, \tag{3.48c}$$

and the wagons total adhesion force is:

$$F_{aW} = n_W\, Q_W\, \mu_W, \tag{3.49}$$

where n_W is the total amount of wheels of all the wagons.

3.7.5 Coupler Force

The coupler force is needed to compute the longitudinal interface force vector, (3.12). It is computed using (3.32).

3.7.6 Rolling Resistance

As mentioned in Section 3.4.1, the aerodynamic drag on the locomotive is assumed to be negligible. However, on a full train with wagons, it is significant [16, 26], and is present in (3.31a). Due to the complexity of aerodynamic drag and variable designs of rolling stock, the calculation of the moving or rolling resistance is still dependent on empirical formulas. One such empirical formula, which is used here, is the Modified Davis equation [4]:

$$F_r = (m_W/1000)\,K_a(2.943 + 89000/m_a + 0.0305\,v_W + 1718\,k_{ad}v_W^2/(m_a\,n)), \qquad (3.50)$$

where F_r (N) is the rolling resistance, K_a is an adjustment factor depending on the rolling stock type, m_a (kg) is the mass per axle, k_{ad} is an air drag constant depending on the wagons type, and n is the number of axles.

3.8 SIMULATION

The train model in (3.33) to (3.37) is simulated to show that the desired dynamics are captured in the simulation model with sufficient accuracy.

3.8.1 Simulation Configuration

A simulation is configured with the specified parameters in Appendix B. The second notch is selected ($1/4$ of the tractive effort), a single wagon with a weight of 15 ton is attached to the locomotive, and the track angle is 1°. The *low* adhesion condition (see Table B.2) is selected for simulation for the first six seconds of the simulation. After that, the *very low* adhesion condition is simulated.

3.8.2 Simulation Solver

Suppose that at the start of the simulation, the maximum torque is applied by the motor to a wheelset. The wheelset will immediately start accelerating, and an adhesion force will be generated from the Polach model, as described in Section 2.4.3 and 3.7.4. The solver must find the correct adhesion force and wheel angular velocity simultaneously. If it overestimates the adhesion force, the wheelset will rotate in the opposite direction, which is unrealistic. If the adhesion force is underestimated, the wheelset will accelerate too fast. The solver needs multiple steps to find the correct adhesion force at each new time instance of the simulation for each wheel. Therefore, it is important to carefully choose an integration method to ensure numeric stability [14]. The simulations in this dissertation uses the Dormand-Prince algorithm with a variable step, producing simulation results without numerical instability.

3.8.3 Simulation Results

As shown in Fig. 3.8, the chosen simulation conditions produce unstable slip in all the wheelsets. Initially, the motors output the most torque, as shown in Fig. 3.9, which causes the adhesion coefficient to exceed the maximum adhesion limit, resulting in unstable wheel slip. When the adhesion level drops at six seconds, unstable slip occurs again in all wheelsets. The slip is the smallest in the rear wheelset because the normal force of the rear wheelset, F_{N22}, is the largest, as shown in Fig. 3.10. The normal forces are not distributed evenly since the centre of gravity of the locomotive is towards the rear, as seen in Table B.7.

In the stable slip region, the adhesion coefficient increases with an increase in slip ratio. During unstable slip, the wheel velocities will continue to increase while the adhesion coefficient continues to decrease if the applied torque is not reduced. The torque of the rear wheelset T_{22} remains roughly constant for the first second. However, the adhesion force, F_{a22}, drops (as seen in Fig. 3.11), while the wheel surface velocity, v_{dL22}, continues to increase (see Fig. 3.8). Only after the torque decreases (see Fig. 3.9) dramatically does the adhesion force start to increase. Re-adhesion occurs in this simulation because the torque gradually decreases as the wheel surface velocities increase, as described in Section

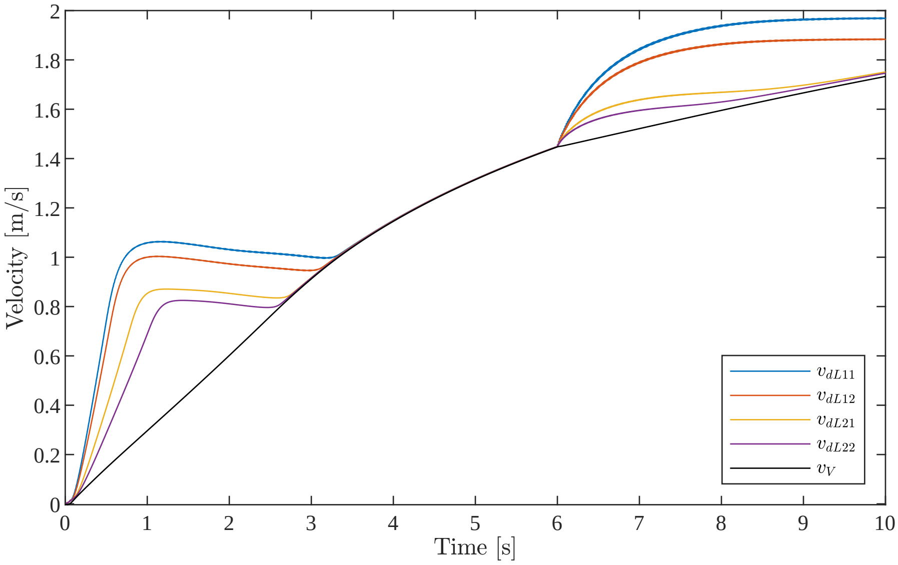

Figure 3.8. Locomotive velocity, v_V , and left wheel surface velocities v_{dLij}.

2.3.2.2. The rate at which re-adhesion occurs could be improved by choosing a more conservative torque reduction factor k_f. This simulation is done purposefully with a small torque reduction factor so that the worst-case slip occurs for the slip controller to handle. As mentioned, unstable slip reduces the adhesion force. In addition, torsional vibrations occur, as shown in Fig. 3.12, that can damage the wheels and rail. As mentioned in Section 3.2.4 and 3.7.3, the normal force of the left and right

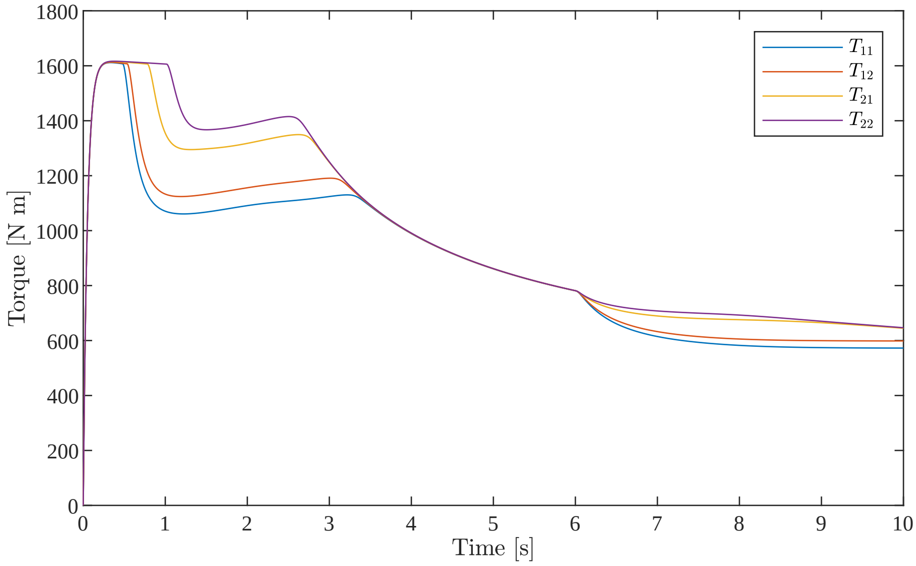

Figure 3.9. Traction motor torques.

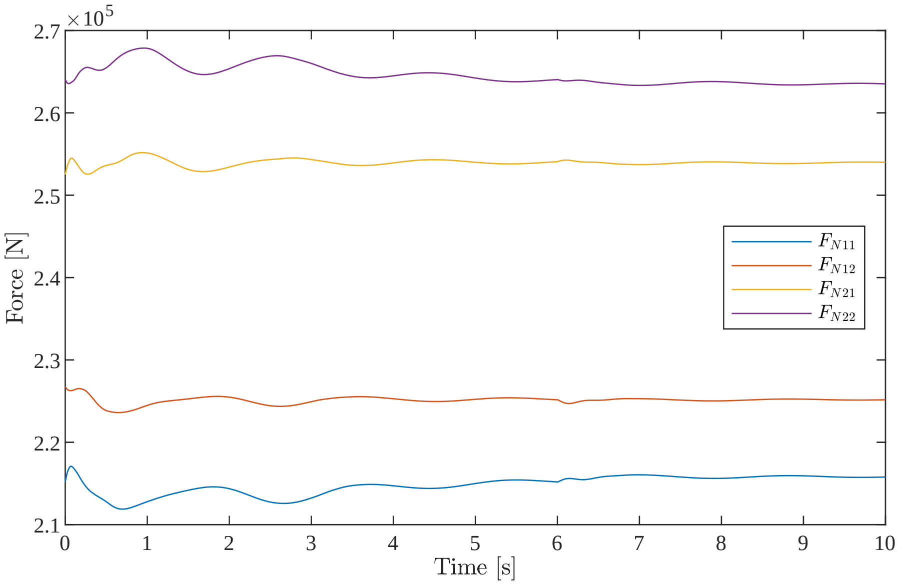

Figure 3.10. Wheelset normal forces.

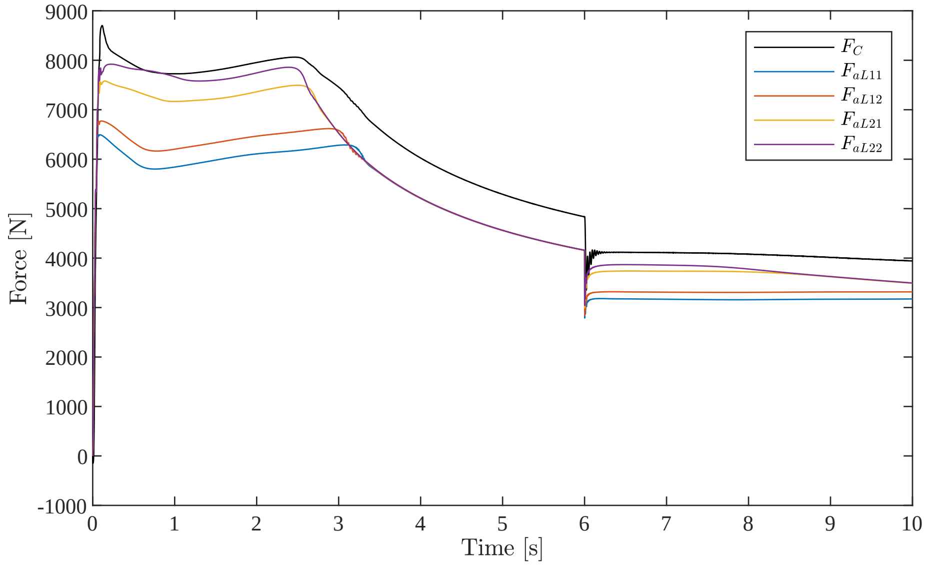

Figure 3.11. Left wheel adhesion forces, F_{aLij}, and coupler force F_C.

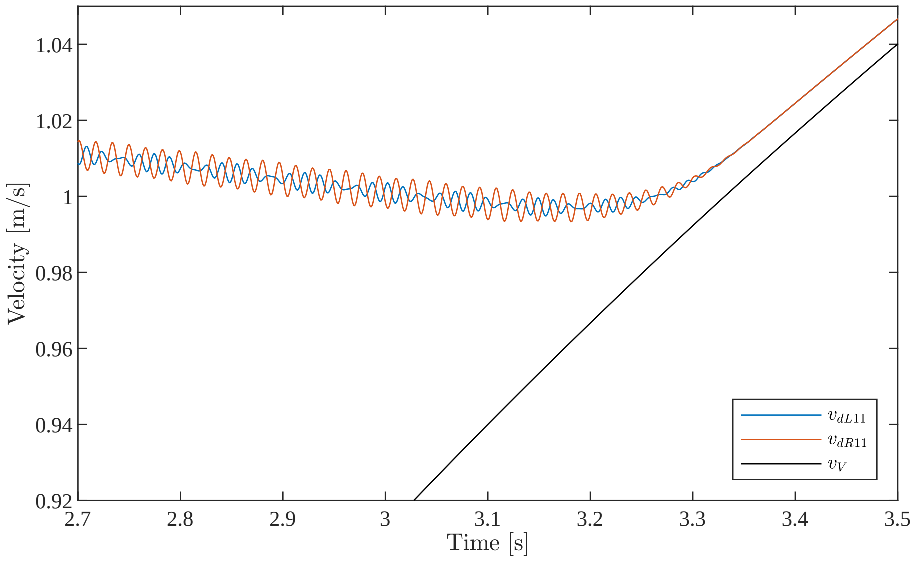

Figure 3.12. Locomotive velocity and surface velocities of both wheels of the front bogie front wheelset.

wheelsets are equal in the simulation. However, torsional vibrations still occur due to the non-rigid wheelset model, as described in Section 3.4.4 and explained in Section 3.2.3, with the adhesion forces calculated separately for each wheel, as described in Section 3.7.4. This occurs because unstable slip creates a low-friction environment where the wheels move more freely over the rail.

Despite the wagon modelling (Section 3.5) being simple, it produces a realistic coupler force, as shown in Fig. 3.11. As expected, the coupler force increases as the tractive force (the sum of all the adhesion forces) increases and decreases when the tractive forces decrease, with some variation due to its stiffness and damping.

3.9 CONCLUSION

The simulation model aims to provide a model of the locomotive in Fig. 1.1 connected to a set of wagons within which the dynamics that have the most significant impact on slip are captured. Slip mainly depends on the wheel-surface conditions, the normal force, and the applied torque/force. A single axle wheelset model, as used in [15, 16], provide a simple model with which to develop and test slip control methods. While such a simple model is informative for developing a slip controller, it neglects much of the dynamics that may make estimation and control complex. Unstable slip in one wheelset may result in slip in another wheelset [23]. Oscillation in the wheelsets impacts their slip ratios. In addition, torsional vibration during unstable slip should be avoided.

The adhesion force is directly proportional to the normal force. Therefore, variations in the normal forces impact slip. The longitudinal velocity of the locomotive is dependent on the adhesion forces and the wagon dynamics. In the presented model, where all wheelsets are modelled, the pitch dynamics are captured through the suspension forces, and the coupler force should consider all the relevant dynamics.

Unstable slip is expected if a locomotive pulls a load under bad adhesion conditions. The simulation model can simulate unstable slip under variable adhesion conditions, providing sufficient variability and complexity to test the estimator and slip controller.

A limitation of this model is that it does not include the roll and lateral dynamics. These dynamics are especially relevant during during cases where the train travels along a curve in the track [13]. Due to the conicity of the wheels, the distance of the axles to the contact points of the wheels (radii) does not stay constant during curves in the track. As mentioned, the difference in the normal forces between the wheels of a wheelset is not essential for this simulation. Unstable lateral slip will reduce the longitudinal adhesion force [37]. However, estimating the lateral adhesion forces is unnecessary, and the model provides sufficient variability of the longitudinal adhesion forces to test the estimation and control. Unfortunately, dynamic variation of the wheel radius is not possible with this model.

To simulate the dynamics during curving, a multi-body simulation should be performed. Torsional vibration is seen, even though the normal forces of the wheels of a wheelset are equal. Therefore, we may assume that the relevant dynamics are modelled, and the roll dynamics may be ignored.

The train model provides a robust foundation for assessing estimation and slip control strategies for locomotives on straight tracks (excluding curves).

CHAPTER 4 ESTIMATION MODEL

4.1 CHAPTER OVERVIEW

To enable effective slip control and slip ratio reference adaptation, as shown in Fig. 2.6, estimates of the adhesion forces, locomotive velocity, normal forces, adhesion coefficients, slip ratios, wheel surface velocities, coupler force, and the rail angle are needed. Section 4.2 describes the wheelset rotational model used in the estimator to estimate the adhesion forces. The longitudinal model is described in Section 4.3, from which the locomotive velocity and coupler force estimates can be produced. In Section 4.4, the longitudinal and wheelset rotational models are combined with the pitch and vertical dynamics in a Kalman filter to produce an estimator for the full model. This estimator is simplified in Section 4.5. The simplified estimator does not contain the pitch and vertical dynamics, as shown in Fig. 4.1. The calculation of the normal force estimates for the full and simplified estimators are described in Section 4.6, and the adhesion coefficient and slip ratio estimate calculations are described in Section 4.7. Section 4.8 presents the simulation results, where the estimation accuracy of the estimators is evaluated. The chapter is concluded in Section 4.9.

4.2 ADHESION FORCE ESTIMATION

As discussed in Section 2.7.3.3.1, an estimator could be constructed based on the rotational dynamics of the wheelset to estimate the adhesion force. Typically, the motor torque is known (estimated within the motor control system), and an encoder measures its angular velocity [8]. These two known parameters are insufficient for the full wheelset model in Section 3.4.4 to produce an observable estimator where both adhesion forces are estimated. By applying a known motor torque, a specific angular velocity response is expected based on the known system dynamics. The estimator should be able to resolve the difference between the measured angular velocity and the expected angular velocity by estimating the disturbance caused by the adhesion forces. By assuming both adhesion forces are equal, $\frac{1}{2}F_a = F_{aL} = F_{aR}$, an observable estimator can be produced. The estimated adhesion force, F_a,

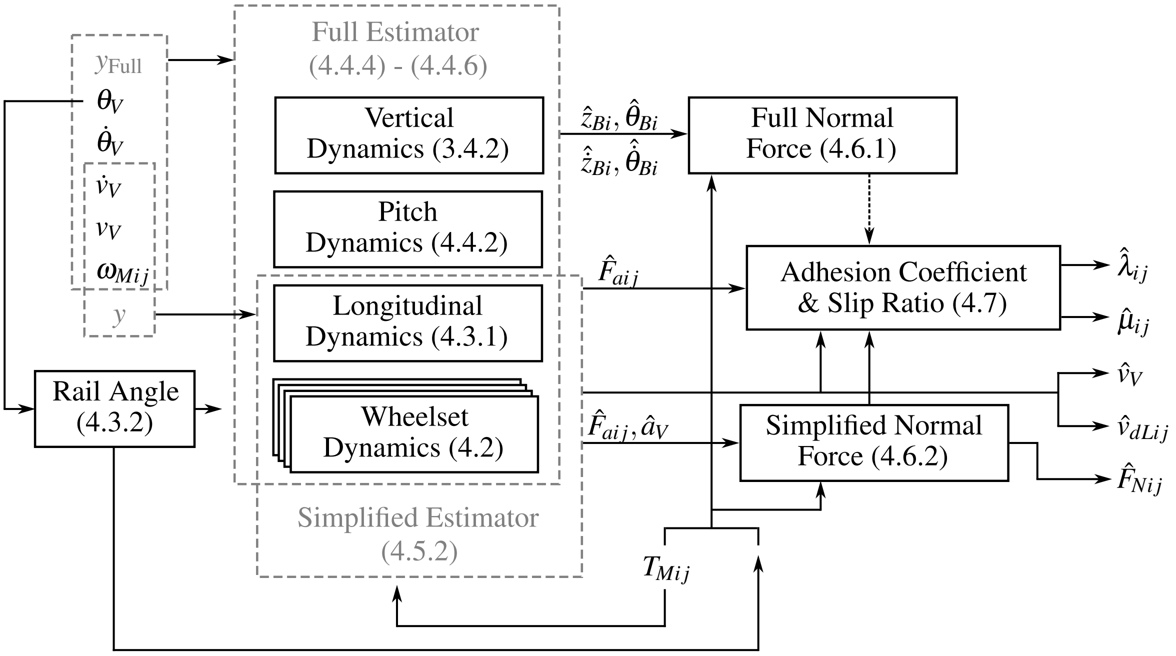

Figure 4.1. Full and simplified estimation models overview. The numbers in brackets indicate the section that describes the block.

estimates the sum of the left and right wheel adhesion forces. From the perspective of a slip control system, the difference between the left and right wheel adhesion forces is not of interest since they cannot be controlled independently in most locomotives.

In [22] and [3], the five-mass wheelset model, as shown in Fig. 3.4, is simplified to a two-mass model, as described in Section 2.7.3.3.1. While such a model reduces the order and preserves the most significant frequency dynamics [22], the model order reduction does not ensure optimal matching of the frequency dynamics. A new model is derived here by using balanced model reduction.

4.2.1 Wheelset Model

The wheelset state-space model for the estimator is:

$$\dot{\boldsymbol{x}}_w = \boldsymbol{A}_w \boldsymbol{x}_w + \boldsymbol{B}_w \boldsymbol{f}_w \tag{4.1a}$$

$$\boldsymbol{y}_w = \boldsymbol{C}_w \boldsymbol{x}_w, \tag{4.1b}$$

where (4.1a) is derived from (3.23) and (3.24) using (3.2) to (3.5) by selecting the displacement vector as:

$$\boldsymbol{q}_w = \begin{bmatrix} \theta_L & \theta_R & \theta_G & \theta_M \end{bmatrix}^T. \tag{4.2}$$

The interface force vector is:

$$\boldsymbol{f}_w = \begin{bmatrix} -r_L F_{aL} & -r_R F_{aR} & 0 & T_M \end{bmatrix}^T. \tag{4.3}$$

The outputs relevant to the estimator are the motor angular velocity, $\omega_M = \dot{\theta}_M$, and the left (or right) wheel surface velocity, $v_{dL} = r_L \omega_L$ (where $\omega_L = \dot{\theta}_L$). Therefore, the output matrix is:

$$\boldsymbol{C}_w = \begin{bmatrix} 0 & 0 & 0 & 0 & 0 & 0 & 0 & 1 \\ 0 & 0 & 0 & 0 & r_L & 0 & 0 & 0 \end{bmatrix}. \tag{4.4}$$

The model of (4.1) contains three complex pole pairs due to the three non-rigid axles of the wheelset and two integrators. Since both relevant outputs are velocities, one of the integrators will produce an unobservable and uncontrollable mode (the absolute angles cannot be determined). Therefore, a minimum realization reduces the order of the model from eight to seven:

$$\tilde{\boldsymbol{G}}_{\min}(s) \overset{s}{=} \left[\begin{array}{c|c} \boldsymbol{A}_{\min} & \boldsymbol{B}_{\min} \\ \hline \boldsymbol{C}_{\min} & 0_{2\times 4} \end{array}\right] \overset{s}{=} \text{minreal} \left[\begin{array}{c|c} \boldsymbol{A}_w & \boldsymbol{B}_w \\ \hline \boldsymbol{C}_w & 0_{2\times 4} \end{array}\right]. \tag{4.5}$$

The tilde symbol indicates that the plant is not scaled (input-output normalized), minreal is the minimum realization function, and $0_{p\times q}$ is a matrix of zeros with p rows and q columns. This model can be simplified further using a balanced truncation to maintain the most significant frequency components.

4.2.2 Model Order Reduction

A balanced realization can only be produced from a given realization if it is asymptotically stable [28]. Therefore, the integrator should be separated from the model before reduction of the stable part. An orthogonal matrix, $\boldsymbol{Q}$, can be found[1] that transforms $\boldsymbol{A}_{\min}$ to the upper Schur form:

$$\boldsymbol{Q}\boldsymbol{A}_{\min}\boldsymbol{Q}^T = \begin{bmatrix} \boldsymbol{A}_{11} & \boldsymbol{A}_{12} \\ \boldsymbol{0} & \boldsymbol{A}_{22} \end{bmatrix}, \tag{4.6}$$

so that $\mathrm{Re}(\lambda_i(\boldsymbol{A}_{11})) < 0$ and $\mathrm{Re}(\lambda_i(\boldsymbol{A}_{22})) \geq 0$ [40], where λ_i here indicates the $i-$th eigenvalue. In our case $\boldsymbol{A}_{22}$ will be a scalar containing the integrator, i.e. $A_{22} = 0$. A second transformation is performed so that:

$$\begin{bmatrix} \boldsymbol{I} & -\boldsymbol{X} \\ \boldsymbol{0} & \boldsymbol{I} \end{bmatrix} \begin{bmatrix} \boldsymbol{A}_{11} & \boldsymbol{A}_{12} \\ \boldsymbol{0} & \boldsymbol{A}_{22} \end{bmatrix} \begin{bmatrix} \boldsymbol{I} & \boldsymbol{X} \\ \boldsymbol{0} & \boldsymbol{I} \end{bmatrix} = \begin{bmatrix} \boldsymbol{A}_{11} & \boldsymbol{A}_{11}\boldsymbol{X} - \boldsymbol{X}\boldsymbol{A}_{22} + \boldsymbol{A}_{12} \\ \boldsymbol{0} & \boldsymbol{A}_{22} \end{bmatrix}, \tag{4.7}$$

where $\boldsymbol{X}$ is the solution of the Sylvester equation, $\boldsymbol{A}_{11}\boldsymbol{X} - \boldsymbol{X}\boldsymbol{A}_{22} + \boldsymbol{A}_{12} = \boldsymbol{0}$ [40]. This Sylvester equation has a solution if $\boldsymbol{A}_{11}$ and $\boldsymbol{A}_{22}$ do not have common eigenvalues, in which case it can be solved using the Bartels-Steward algorithm [40]. In our case $A_{22} = 0$; therefore:

$$\boldsymbol{X} = -\boldsymbol{A}_{11}^{-1}\boldsymbol{A}_{12}. \tag{4.8}$$

---

[1] See MATLAB's schur function.

The new state space matrices are:

$$\begin{aligned}\bar{\boldsymbol{A}} &= \boldsymbol{V}\boldsymbol{Q}\boldsymbol{A}\boldsymbol{Q}^T\boldsymbol{V}^{-1} = \begin{bmatrix}\boldsymbol{A}_{11} & \boldsymbol{0}\\ \boldsymbol{0} & A_{22}\end{bmatrix}\\ \bar{\boldsymbol{B}} &= \boldsymbol{V}\boldsymbol{Q}\boldsymbol{B} = \begin{bmatrix}\bar{\boldsymbol{B}}_1\\ \bar{B}_2\end{bmatrix}\\ \bar{\boldsymbol{C}} &= \boldsymbol{C}\boldsymbol{Q}^T\boldsymbol{V}^{-1} = \begin{bmatrix}\bar{\boldsymbol{C}}_1 & \bar{C}_2\end{bmatrix},\end{aligned} \tag{4.9}$$

where $\boldsymbol{V} = \begin{bmatrix}\boldsymbol{I} & -\boldsymbol{X}\\ \boldsymbol{0} & \boldsymbol{I}\end{bmatrix}$. The Hankel singular values of the section of the state space model without the integrator:

$$\tilde{\boldsymbol{G}}_{\text{sec}} \overset{s}{=} \left[\begin{array}{c|c}\boldsymbol{A}_{11} & \bar{\boldsymbol{B}}_1\\ \hline \bar{\boldsymbol{C}}_1 & 0_{2\times 4}\end{array}\right], \tag{4.10}$$

are $\sigma_i = [11.4\times10^{-3}\ 11.4\times10^{-3}\ 6.7\times10^{-3}\ 6.7\times10^{-3}\ 95.6\times10^{-6}\ 95.6\times10^{-6}]$. The last two singular values are much smaller than the others, which indicates that the order of this model can be reduced to four without impacting the input-output behaviour significantly. The intermediate reduced order model is:

$$\tilde{\boldsymbol{G}}_{\text{int}}(s) \overset{s}{=} \left[\begin{array}{c|c}\boldsymbol{A}_{\text{int}} & \boldsymbol{B}_{\text{int}}\\ \hline \boldsymbol{C}_{\text{int}} & 0_{2\times 4}\end{array}\right] \overset{s}{=} \text{balred}\{\boldsymbol{G}_{\text{sec}}\}. \tag{4.11}$$

where balred is the balanced order reduction function with the order specified as four. The $\mathcal{H}_\infty$ error caused by this truncation will be limited to [28]:

$$\begin{aligned}||\tilde{\boldsymbol{G}}_{\text{sec}} - \tilde{\boldsymbol{G}}_{\text{int}}||_\infty &\leq 2(95.6\times10^{-6} + 95.6\times10^{-6})\\ &\leq 382.4\times10^{-6}.\end{aligned} \tag{4.12}$$

The integrator is added back to (4.11) to produce the reduced order model:

$$\begin{aligned}\boldsymbol{A}_{\text{red}} &= \begin{bmatrix}\boldsymbol{A}_{\text{int}} & 0_{4\times1}\\ 0_{1\times4} & A_{22}\end{bmatrix} \quad \boldsymbol{B}_{\text{red}} = \begin{bmatrix}\boldsymbol{B}_{\text{int}}\\ \bar{B}_2\end{bmatrix}\\ \boldsymbol{C}_{\text{red}} &= \begin{bmatrix}\boldsymbol{C}_{\text{int}} & \bar{C}_2\end{bmatrix},\end{aligned} \tag{4.13}$$

By comparing the frequency responses of the motor torque, T_M, to motor angular velocity, ω_M, of the minimum realization model in (4.5) and the reduced order model in (4.13) in Fig. 4.2, it is shown that the reduced order model preserves the two most significant resonant peaks and the peak caused by the high-frequency complex pole-zero pairs is removed.

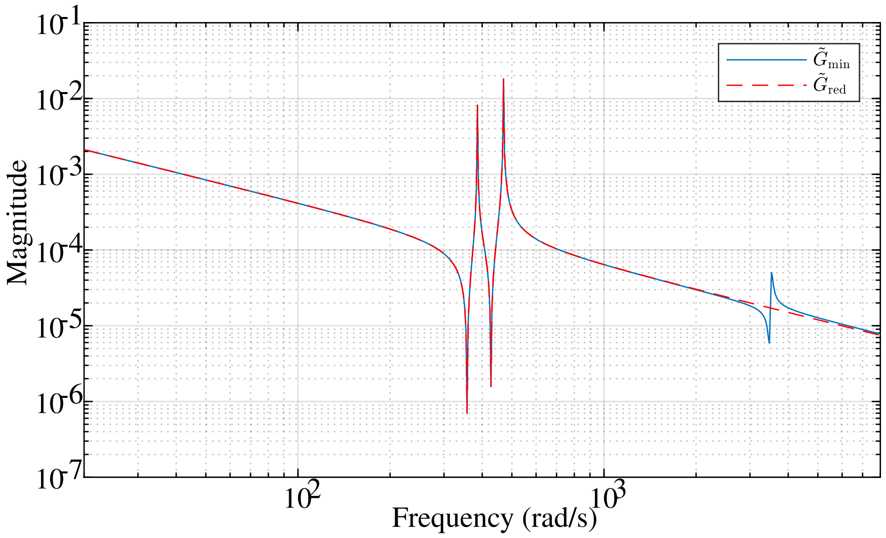

Figure 4.2. Bode plot of the motor torque, T_M, to motor angular velocity, ω_M, for the minimum realization and reduced order models.

4.2.3 Estimation Model

An estimator can be constructed from the model in (4.13) by assuming no inherent dynamic understanding of the adhesion force, i.e. $\dot{F}_a = 0$ [35]. The input to the estimator is the motor torque, $u_{\text{est}} = T_M$, and the measured output is the motor angular velocity, $y_{\text{est}} = \omega_M$. Therefore, the state vector of the estimator is:

$$\boldsymbol{x}_{\text{est}} = \begin{bmatrix} \boldsymbol{x}_{\text{red}} \\ F_a \end{bmatrix}, \tag{4.14}$$

where $\boldsymbol{x}_{\text{red}}$ is the state vector of the model in (4.13), and state-space matrices of the estimator are:

$$\boldsymbol{A}_{\text{est}} = \begin{bmatrix} \boldsymbol{A}_{\text{red}} & \frac{1}{2}\left(-r_L \cdot \boldsymbol{B}_{\text{red}[:,1]} - r_R \cdot \boldsymbol{B}_{\text{red}[:,2]}\right) \\ 0_{1\times 5} & 0 \end{bmatrix} = \begin{bmatrix} \boldsymbol{A}_{\text{red}} & \boldsymbol{A}_{\text{est}Fa} \\ 0_{1\times 5} & 0 \end{bmatrix} \tag{4.15a}$$

$$\boldsymbol{B}_{\text{est}} = \begin{bmatrix} \boldsymbol{B}_{\text{red}[:,4]} \\ 0 \end{bmatrix} \tag{4.15b}$$

$$\boldsymbol{C}_{\text{est}} = \begin{bmatrix} \boldsymbol{C}_{\text{red}[1,:]} & 0 \end{bmatrix} \tag{4.15c}$$

$$D_{\text{est}} = 0, \tag{4.15d}$$

where $\boldsymbol{X}_{[a,:]}$ and $\boldsymbol{X}_{[:,b]}$ are the a row and b column vectors of matrix $\boldsymbol{X}$ respectively. The sixth state in (4.14) contains the estimate of the adhesion force. The estimates of the motor angular velocity and the left wheel surface velocity are obtained by:

$$\hat{\omega}_M = \boldsymbol{C}_{\mathrm{red}[1,:]}\hat{\boldsymbol{x}}_{\mathrm{red}} \tag{4.16}$$

$$\hat{v}_{dL} = \boldsymbol{C}_{\mathrm{red}[2,:]}\hat{\boldsymbol{x}}_{\mathrm{red}}, \tag{4.17}$$

where $\hat{\boldsymbol{x}}_{\mathrm{red}}$ is the reduced order state estimate produced by an observer such as a Kalman filter.

4.3 LOCOMOTIVE VELOCITY ESTIMATION

The locomotive velocity must be determined for the estimator to produce longitudinal slip ratio estimates. As discussed in Section 2.7.1, the efficiency of slip control is directly linked to the accuracy of the vehicle velocity estimate [16]. While estimation without a direct measurement is possible, as discussed in Section 2.7.1.2, the most reliable method is using a Doppler radar. However, a Doppler radar by itself is not sufficiently accurate. Combining an accelerometer to measure the longitudinal acceleration, $\dot{v}_V$, and the Doppler radar in a model-based estimator can produce a sufficiently accurate estimate of the locomotive velocity, v_V.

As outlined in Section 3.2.5, modelling the longitudinal dynamics of a train is complex due to the relative motions between the wagons and many unknowns, such as the masses of the wagons, propulsion resistance, and coupling slack [4]. A dependence on measurements onboard the wagons is not feasible. A practical approach for constructing an estimator is to model the coupler force, F_C, as an unknown disturbance and to assume no inherent dynamic understanding thereof, i.e. $\dot{F}_C = 0$.

4.3.1 Longitudinal Model

The longitudinal stiffness between the body, bogies and wheelsets respectively, is generally large. Therefore, the estimation model may assume that the relative longitudinal displacements between the subsystems are zero. Subsequently, longitudinal dynamics of (3.6) are simplified to:

$$m_L \dot{v}_V = F_{a11} + F_{a12} + F_{a21} + F_{a22} - F_C - F_{gL} \sin\beta, \tag{4.18}$$

where m_L is the total locomotive weight, F_{aij} are the adhesion forces, and $F_{gL} = m_L g$ is the gravitational force of the locomotive. While the coupler force will have a longitudinal and a vertical impact, its longitudinal component is much larger. Therefore, the vertical component of the coupler force is ignored.

4.3.2 Rail Angle

Since the rail angle, β, does not change rapidly, it is computed by low-pass filtering the locomotive body angle measurement, which is calculated from the accelerometers of an onboard inertial measurement unit (IMU). The IMU should be placed inside the locomotive body. Therefore, the angle measured by the IMU is the sum of the rail angle, the body angle, and measurement noise, γ (rad):

$$\beta_{\text{IMU}} = \beta + \theta_V + \gamma, \tag{4.19}$$

A simple first-order delay is used as a low pass filter:

$$\hat{\beta} = \frac{1}{\tau_{LPF}s + 1}\beta_{\text{IMU}}, \tag{4.20}$$

where τ_{LPF} (s) is the low pass filter time constant that roughly approximates the cut-off frequency, $1/\tau_{LPF}$ (Hz), and s is the Laplace variable. A first-order delay has an infinite impulse response. In practice, finite impulse response filters are preferred due to their stability, but the filter in (4.20) should suffice for simulation.

4.4 ESTIMATOR FOR THE FULL MODEL

Combining the longitudinal model in Section 4.3.1 with the wheelset model in Section 4.2.3 for each wheelset in a model-based estimator, the adhesion forces and slip ratios of each wheelset can be estimated. However, to estimate the adhesion coefficients, the normal forces have to be estimated.

During unstable slip, there is a significant redistribution of the normal forces between the wheelsets [23]. As mentioned in Section 4.2, the difference between the adhesion forces (and, by extension, the normal forces) of the left and right wheels is not essential for slip control.

As discussed in Section 2.7.3.3.2 and 3.2.4, a good starting point for the estimator is to include most of the dynamics in the simulation model since the simulation model contains the dynamics most relevant to slip control. Including the pitch dynamics should yield an estimator capable of producing accurate normal force estimates [34].

4.4.1 Longitudinal, Vertical and Wheelset Rotational Dynamics

The wheelset rotational and longitudinal dynamics of the consolidated (full) estimation model are as described in Section 4.2.3 and 4.3.1. The vertical dynamics are the same as in Section 3.4.2 described by (3.13) - (3.15), except for its interface force vector (3.17), where the vertical component of the coupler force is ignored.

4.4.2 Pitch Dynamics

Since the longitudinal displacements are assumed to be negligible, $m_{Bi}\ddot{x}_{Bi}$ and $m_{Wij}\ddot{x}_{Wij}$ in (3.6) are zero. The vertical component of the coupler force is ignored. Therefore, the pitch dynamics of the estimator, derived by solving for F_{PXij} and F_{Ti} and substituting into (3.19), is:

$$\begin{aligned} I_V\ddot{\theta}_V &= L_{V11}F_{S11} + L_{V12}F_{S12} - L_{V21}F_{S21} - L_{V22}F_{S22} \\ &\quad + H_{VT}\frac{m_V}{m_L}(F_{a11} + F_{a12} + F_{a21} + F_{a22}) + (\frac{m_L - m_V}{m_L}H_{VT} - H_C)F_C \end{aligned} \tag{4.21a}$$

$$\begin{aligned} I_{Bi}\ddot{\theta}_{Bi} &= L_{Pi1}F_{Pi1} - L_{Pi2}F_{Pi2} - L_{Si1}F_{Si1} + L_{Si2}F_{Si2} + L_{MBi1}F_{MBi1} - L_{MBi2}F_{MBi2} \\ &\quad + (H_P + H_{BT})(F_{ai1} + F_{ai2} - (F_{gWi1} + F_{gWi2})\sin\beta) - H_{BT}F_{gBi}\sin\beta \\ &\quad - \psi_i(F_{a11} + F_{a12} + F_{a21} + F_{a22} - F_{gL}\sin\beta - F_C), \end{aligned} \tag{4.21b}$$

with:

$$\psi_i = \frac{(H_P + H_{BT})(m_{Wi1} + m_{Wi2}) + H_{BT}m_{Bi}}{m_L}, \tag{4.22}$$

where the suspension forces, F_{Pij} and F_{Sij}, are as described in (3.14) and (3.15) respectively, and the motor to housing forces, F_{MBij}, are as described in (3.40).

By choosing the displacement vector as:

$$\boldsymbol{q}_{\text{pitchEst}} = \begin{bmatrix} z_V & z_{B1} & z_{B2} & \theta_V & \theta_{B1} & \theta_{B2} & F_{a11} & F_{a12} & F_{a21} & F_{a22} & F_C \end{bmatrix}^T, \tag{4.23}$$

and comparing it to the displacement vector in the simulation model, (3.20), the mass, damping and stiffness matrices describing (4.21), from (A.11) and (A.12), are:

$$\boldsymbol{M}_{\text{pitchEst}} = \begin{bmatrix} 0_{3\times3} & \text{diag}[I_V \quad I_{B1} \quad I_{B2}] & 0_{3\times5} \end{bmatrix} \tag{4.24}$$

$$\boldsymbol{C}_{\text{pitchEst}} = \begin{bmatrix} \boldsymbol{C}_{\text{pitch}[1:3,8:13]} & 0_{3\times5} \end{bmatrix} \tag{4.25}$$

$$\boldsymbol{K}_{\text{pitchEst}} = \Bigg[\boldsymbol{K}_{\text{pitch}[1:3,8:13]} \quad \cdots$$

$$\begin{matrix} -H_{VT}\frac{m_V}{m_L} & -H_{VT}\frac{m_V}{m_L} & -H_{VT}\frac{m_V}{m_L} & -H_{VT}\frac{m_V}{m_L} & H_C - \frac{m_L - m_V}{m_L}H_{VT} \\ \psi_1 - H_P - H_{BT} & \psi_1 - H_P - H_{BT} & \psi_1 & \psi_1 & -\psi_1 \\ \psi_2 & \psi_2 & \psi_2 - H_P - H_{BT} & \psi_2 - H_P - H_{BT} & -\psi_2 \end{matrix} \Bigg] \tag{4.26}$$

where $\boldsymbol{X}_{[i_1:i_2,j_1:j_2]}$ is used to denote a sub-matrix of X consisting of the intersection of rows i_1 to i_2 and columns j_1 to j_2.

4.4.3 Vertical and Pitch Combined

The vertical and pitch dynamics are combined by choosing the displacement vector the same as (4.23), from which the mass, damping and stiffness matrices are:

$$\boldsymbol{X}_{\text{v\&p}} = \begin{bmatrix} \{\boldsymbol{X}_{\text{vert}}\}_{3\times 6} & 0_{3\times 5} \\ \multicolumn{2}{c}{\{\boldsymbol{X}_{\text{pitchEst}}\}_{3\times 11}} \\ 0_{5\times 6} & \{\boldsymbol{I}\}_{5\times 5} \end{bmatrix}, \tag{4.27}$$

where $\boldsymbol{X}_{\text{v\&p}}$ is substituted by either $\boldsymbol{M}_{\text{v\&p}}$, $\boldsymbol{K}_{\text{v\&p}}$ or $\boldsymbol{C}_{\text{v\&p}}$ for the mass, stiffness and damping matrices respectively.

The state space form is derived from:

$$\dot{\boldsymbol{x}}_{\text{v\&p}} = \boldsymbol{A}_{\text{v\&p}}\boldsymbol{x}_{\text{v\&p}} + \boldsymbol{B}_{\text{v\&p}}\boldsymbol{f}_{\text{v\&p}} \tag{4.28}$$

$$\begin{bmatrix} \dot{\boldsymbol{q}}_{\text{v\&p}} \\ \ddot{\boldsymbol{q}}_{\text{v\&p}} \end{bmatrix} = \begin{bmatrix} 0_{11\times 11} & \{\boldsymbol{I}\}_{11\times 11} \\ -\boldsymbol{M}^{-1}_{\text{v\&p}}\boldsymbol{K}_{\text{v\&p}} & -\boldsymbol{M}^{-1}_{\text{v\&p}}\boldsymbol{C}_{\text{v\&p}} \end{bmatrix} \begin{bmatrix} \boldsymbol{q}_{\text{v\&p}} \\ \dot{\boldsymbol{q}}_{\text{v\&p}} \end{bmatrix} + \begin{bmatrix} 0_{11\times 11} \\ \boldsymbol{M}^{-1}_{\text{v\&p}} \end{bmatrix}. \tag{4.29}$$

Note that the bottom right subsection of $\boldsymbol{X}_{\text{v\&p}}$ in (4.27) is set to $\{\boldsymbol{I}\}_{5\times 5}$, so that $\boldsymbol{M}_{\text{v\&p}}$ is invertible. The last five terms of the state vector are $\ddot{F}_{aij}$ and $\ddot{F}_C$. In the estimation of the adhesion and coupler forces, it is assumed that $\dot{F}_{aij} = 0$ and $\dot{F}_C = 0$. Therefore, the last five rows and columns of the state space matrices are redundant and should be removed so that the new state vector is:

$$\begin{aligned} \boldsymbol{x}_{\text{v\&pNew}} = \Big[& z_V \quad z_{B1} \quad z_{B2} \quad \theta_V \quad \theta_{B1} \quad \theta_{B2} \quad F_{a11} \quad F_{a12} \quad F_{a21} \quad F_{a22} \quad F_C \quad \ldots \\ & \dot{z}_V \quad \dot{z}_{B1} \quad \dot{z}_{B2} \quad \dot{\theta}_V \quad \dot{\theta}_{B1} \quad \dot{\theta}_{B2} \Big]^T. \end{aligned} \tag{4.30}$$

The new state space equation is then:

$$\dot{\boldsymbol{x}}_{\text{v\&pNew}} = \boldsymbol{A}_{\text{v\&pNew}}\,\boldsymbol{x}_{\text{v\&pNew}} + \boldsymbol{B}_{\text{v\&pNew}}\,\boldsymbol{f}_{\text{v\&pNew}}, \tag{4.31}$$

with:

$$\boldsymbol{A}_{\text{v\&pNew}} = \boldsymbol{A}_{\text{v\&p}[1:17,1:17]} \tag{4.32}$$

$$\boldsymbol{B}_{\text{v\&pNew}} = \boldsymbol{B}_{\text{v\&p}[1:17,1:6]}, \tag{4.33}$$

and the interface force vector is:

$$
\boldsymbol{f}_{\text{v\&pNew}} = \begin{bmatrix} F_{gV}\cos\beta \\ F_{gB1}\cos\beta - F_{MB11} - F_{MB12} \\ F_{gB2}\cos\beta - F_{MB21} - F_{MB22} \\ 0 \\ [\psi_1 F_{gL} - H_{BT}F_{gB1} - (H_P + H_{BT})(F_{gW11} + F_{gW12})]\sin\beta + L_{MB11}F_{MB11} - L_{MB12}F_{MB12} \\ [\psi_2 F_{gL} - H_{BT}F_{gB2} - (H_P + H_{BT})(F_{gW21} + F_{gW22})]\sin\beta + L_{MB21}F_{MB21} - L_{MB22}F_{MB22} \end{bmatrix}. \tag{4.34}
$$

4.4.4 Full Estimation Model

The longitudinal, vertical, pitch and rotational dynamics of the estimation model can be combined into a single state space system by choosing the state vector as:

$$
\begin{aligned}
\boldsymbol{x}_{\text{Full}} = \Big[& v_V \quad z_V \quad z_{B1} \quad z_{B2} \quad \theta_V \quad \theta_{B1} \quad \theta_{B2} \quad F_{a11} \quad F_{a12} \quad F_{a21} \quad F_{a22} \quad F_C \\
& \dots \quad \dot{z}_V \quad \dot{z}_{B1} \quad \dot{z}_{B2} \quad \dot{\theta}_V \quad \dot{\theta}_{B1} \quad \dot{\theta}_{B2} \quad \boldsymbol{x}^T_{\text{red}11} \quad \boldsymbol{x}^T_{\text{red}12} \quad \boldsymbol{x}^T_{\text{red}21} \quad \boldsymbol{x}^T_{\text{red}22} \Big]^T.
\end{aligned} \tag{4.35}
$$

The state space matrices are then:

$$
\boldsymbol{A}_{\text{Full}} =
$$

$$
\left[\begin{array}{cccccccccccc}
0 & 0_{1\times6} & 1/m_L & 1/m_L & 1/m_L & 1/m_L & -1/m_L & 0_{1\times6} & 0_{1\times5} & 0_{1\times5} & 0_{1\times5} & 0_{1\times5} \\
0_{17\times1} & \multicolumn{7}{c}{\{\boldsymbol{A}_{\text{v\&pNew}}\}_{17\times17}} & 0_{17\times5} & 0_{17\times5} & 0_{17\times5} & 0_{17\times5} \\
0_{5\times1} & 0_{1\times6} & \boldsymbol{A}_{\text{est}Fa} & 0_{5\times1} & 0_{5\times1} & 0_{5\times1} & 0_{5\times1} & 0_{5\times6} & \boldsymbol{A}_{\text{red}} & 0_{5\times5} & 0_{5\times5} & 0_{5\times5} \\
0_{5\times1} & 0_{1\times6} & 0_{5\times1} & \boldsymbol{A}_{\text{est}Fa} & 0_{5\times1} & 0_{5\times1} & 0_{5\times1} & 0_{5\times6} & 0_{5\times5} & \boldsymbol{A}_{\text{red}} & 0_{5\times5} & 0_{5\times5} \\
0_{5\times1} & 0_{1\times6} & 0_{5\times1} & 0_{5\times1} & \boldsymbol{A}_{\text{est}Fa} & 0_{5\times1} & 0_{5\times1} & 0_{5\times6} & 0_{5\times5} & 0_{5\times5} & \boldsymbol{A}_{\text{red}} & 0_{5\times5} \\
0_{5\times1} & 0_{1\times6} & 0_{5\times1} & 0_{5\times1} & 0_{5\times1} & \boldsymbol{A}_{\text{est}Fa} & 0_{5\times1} & 0_{5\times6} & 0_{5\times5} & 0_{5\times5} & 0_{5\times5} & \boldsymbol{A}_{\text{red}}
\end{array}\right] \tag{4.36a}
$$

$$
\boldsymbol{B}_{\text{Full}} = \begin{bmatrix}
1/m_L & 0_{1\times6} & 0 & 0 & 0 & 0 \\
0_{17\times1} & \{\boldsymbol{B}_{\text{v\&pNew}}\}_{17\times6} & 0_{17\times1} & 0_{17\times1} & 0_{17\times1} & 0_{17\times1} \\
0_{5\times1} & 0_{5\times6} & \boldsymbol{B}_{\text{red}[:,4]} & 0_{5\times1} & 0_{5\times1} & 0_{5\times1} \\
0_{5\times1} & 0_{5\times6} & 0_{5\times1} & \boldsymbol{B}_{\text{red}[:,4]} & 0_{5\times1} & 0_{5\times1} \\
0_{5\times1} & 0_{5\times6} & 0_{5\times1} & 0_{5\times1} & \boldsymbol{B}_{\text{red}[:,4]} & 0_{5\times1} \\
0_{5\times1} & 0_{5\times6} & 0_{5\times1} & 0_{5\times1} & 0_{5\times1} & \boldsymbol{B}_{\text{red}[:,4]}
\end{bmatrix}, \tag{4.36b}
$$

where $\boldsymbol{A}_{\text{red}}$ and $\boldsymbol{B}_{\text{red}}$ are defined (4.13) in and $\boldsymbol{A}_{\text{est}Fa}$ is defined in (4.15a). The interface force vector is:

$$\boldsymbol{f}_{\text{Full}} = \begin{bmatrix} -F_{gL}\sin\beta \\ \boldsymbol{f}_{\text{v\&pNew}} \\ T_{M11} \\ T_{M12} \\ T_{M21} \\ T_{M22} \end{bmatrix}. \tag{4.37}$$

The motor control systems provide the applied motor torques and the rail angle is calculated as explained in Section 4.3.2.

4.4.5 Kalman-Bucy Filter

A Kalman-Bucy filter, the continuous time equivalent of the Kalman filter, is used to construct the estimator. It is described by [41]:

$$\dot{\hat{\boldsymbol{x}}}_{\text{Full}} = \boldsymbol{A}_{\text{Full}}\hat{\boldsymbol{x}}_{\text{Full}} + \boldsymbol{B}_{\text{Full}}\boldsymbol{f}_{\text{Full}} + \boldsymbol{K}_{\text{Full}}\left(\boldsymbol{y}_{\text{Full}} - \hat{\boldsymbol{y}}_{\text{Full}}\right) \tag{4.38a}$$

$$\hat{\boldsymbol{y}}_{\text{Full}} = \boldsymbol{C}_{\text{Full}}\hat{\boldsymbol{x}}_{\text{Full}} + \boldsymbol{D}_{\text{Full}}\boldsymbol{f}_{\text{Full}}, \tag{4.38b}$$

where $\hat{\boldsymbol{x}}_{\text{Full}}$ and $\hat{\boldsymbol{y}}_{\text{Full}}$ are the estimated states and outputs, $\boldsymbol{y}_{\text{Full}}$ is the measured outputs, and $\boldsymbol{K}_{\text{Full}}$ is the Kalman gain [35]. The estimation model is found to be observable by showing that the observability matrix:

$$\boldsymbol{O} = \begin{bmatrix} \boldsymbol{C}_{\text{Full}} \\ \boldsymbol{C}_{\text{Full}}\boldsymbol{A}_{\text{Full}} \\ \boldsymbol{C}_{\text{Full}}\boldsymbol{A}^2_{\text{Full}} \\ \vdots \\ \boldsymbol{C}_{\text{Full}}\boldsymbol{A}^{n-1}_{\text{Full}} \end{bmatrix}, \tag{4.39}$$

where n is the number of states, has full rank. By testing various combinations of output variables, it was found from (4.39) that the minimum measured outputs that would produce an observable estimation model are:

$$\boldsymbol{y}_{\text{Full}} = \begin{bmatrix} \dot{v}_V & v_V & \boldsymbol{p} & \omega_{M11} & \omega_{M12} & \omega_{M21} & \omega_{M22} \end{bmatrix}^T, \tag{4.40}$$

where $\boldsymbol{p}$ must be at least one of the following:

$$z_V \quad z_{B1} \quad z_{B2} \quad \theta_V \quad \theta_{B1} \quad \theta_{B2} \quad \dot{\theta}_V \quad \dot{\theta}_{B1} \quad \dot{\theta}_{B2}.$$

As mentioned in Section 4.3, the locomotive velocity, v_V, is measured with a Doppler radar and the longitudinal acceleration, $\dot{v}_V$, is measured with an accelerometer. Accurate measurements of the motor angular velocities, ω_{Mij}, are readily available from encoders. The bogie pitch angles, $\dot{\theta}_{Bi}$, could be calculated using suspension deflection transducers, which are not common sensors [34]. The locomotive body angle and angular rate can be determined from an IMU. Therefore, these are chosen as the two additional measurements, i.e. $\boldsymbol{p} = [\theta_V \quad \dot{\theta}_V]$.

The Kalman filter can estimate the adhesion forces and coupler forces by attributing large uncertainty in the process noise covariance matrix, $\boldsymbol{Q}_{\text{Full}}$, to the assumption that $\dot{F}_{aij} = 0$ and $\dot{F}_C = 0$ (rows 8 to 12 in (4.38a)) [17, 35]:

$$\boldsymbol{Q}_{\text{Full}} = \text{diag}\left[10_{1\times7} \quad [1\times10^{12}]_{1\times5} \quad 10_{1\times6} \quad 1_{1\times20}\right]. \tag{4.41}$$

The encoder measurements are expected to have lower noise than the other measurements. Therefore the measurement noise covariance matrix, $\boldsymbol{R}_{\text{Full}}$, is set to:

$$\boldsymbol{R}_{\text{Full}} = \text{diag}\left[5 \quad 10 \quad 20 \quad 20 \quad 1_{1\times4}\right]. \tag{4.42}$$

The Kalman gain, $\boldsymbol{K}_{\text{Full}}$, in (4.38a) is found by:

$$\boldsymbol{K}_{\text{Full}} = \boldsymbol{P}_{\text{Full}}\boldsymbol{C}^T_{\text{Full}}\boldsymbol{R}^{-1}_{\text{Full}} \tag{4.43a}$$

$$\dot{\boldsymbol{P}}_{\text{Full}} = \boldsymbol{A}_{\text{Full}}\boldsymbol{P}_{\text{Full}} + \boldsymbol{P}_{\text{Full}}\boldsymbol{A}^T_{\text{Full}} - \boldsymbol{K}_{\text{Full}}\boldsymbol{R}_{\text{Full}}\boldsymbol{K}^T_{\text{Full}} + \boldsymbol{Q}_{\text{Full}}, \tag{4.43b}$$

where $\boldsymbol{P}_{\text{Full}}$ is the error covariance matrix. $\boldsymbol{Q}_{\text{Full}}$ and $\boldsymbol{R}_{\text{Full}}$ are time invariant. Assuming $\dot{\boldsymbol{P}}_{\text{Full}} = 0$, (4.43b) becomes the well known algebraic Ricatti equation [35]. By solving the algebraic Ricatti equation, a constant Kalman gain, $\boldsymbol{K}_{\text{Full}}$, is calculated from (4.43a).

4.4.6 Measurements Update

The measurement update state-space matrices of (4.38b) are needed to generate the estimated outputs, $\hat{\boldsymbol{y}}_{\text{Full}}$. By considering the longitudinal dynamics in (4.18), it is shown that:

$$\boldsymbol{A}_{\text{Full}[1,:]}\hat{\boldsymbol{x}}_{\text{Full}} = \frac{1}{m_L}(\hat{F}_{a11} + \hat{F}_{a12} + \hat{F}_{a21} + \hat{F}_{a22} - \hat{F}_C), \tag{4.44}$$

where $\boldsymbol{A}_{\text{Full}[1,:]}$ is the first row of (4.36a). Compensating for the gravitational force will produce the acceleration estimate:

$$\hat{a}_V = \boldsymbol{A}_{\text{Full}[1,:]}\hat{\boldsymbol{x}}_{\text{Full}} - \frac{1}{m_L}F_{gL}\sin\beta = \boldsymbol{A}_{\text{Full}[1,:]}\hat{\boldsymbol{x}}_{\text{Full}} + \frac{1}{m_L}\boldsymbol{f}_{\text{Full}[1]} \tag{4.45}$$

where $a_V = \dot{v}_V$ $(\mathrm{m/s^2})$ and $\boldsymbol{f}_{\mathrm{Full}[1]}$ is the first element of the external interface force vector described in (4.37). Therefore, the measurement update state space matrices are:

$$\boldsymbol{C}_{\mathrm{Full}} = \begin{bmatrix} \boldsymbol{A}_{\mathrm{Full}[1,:]} \\ \begin{bmatrix} 1 & 0_{1\times37} \end{bmatrix} \\ \begin{bmatrix} 0_{1\times4} & 1 & 0_{1\times33} \end{bmatrix} \\ \begin{bmatrix} 0_{1\times15} & 1 & 0_{1\times22} \end{bmatrix} \\ \begin{bmatrix} 0_{1\times18} & \boldsymbol{C}_{\mathrm{red}[1,:]} & 0_{1\times5} & 0_{1\times5} & 0_{1\times5} \end{bmatrix} \\ \begin{bmatrix} 0_{1\times18} & 0_{1\times5} & \boldsymbol{C}_{\mathrm{red}[1,:]} & 0_{1\times5} & 0_{1\times5} \end{bmatrix} \\ \begin{bmatrix} 0_{1\times18} & 0_{1\times5} & 0_{1\times5} & \boldsymbol{C}_{\mathrm{red}[1,:]} & 0_{1\times5} \end{bmatrix} \\ \begin{bmatrix} 0_{1\times18} & 0_{1\times5} & 0_{1\times5} & 0_{1\times5} & \boldsymbol{C}_{\mathrm{red}[1,:]} \end{bmatrix} \end{bmatrix} \tag{4.46a}$$

$$\boldsymbol{D}_{\mathrm{Full}} = \begin{bmatrix} \frac{1}{m_L} \\ 0_{7\times38} \end{bmatrix}, \tag{4.46b}$$

where $\boldsymbol{C}_{\mathrm{red}}$ is defined in (4.13).

4.5 ESTIMATOR FOR THE SIMPLIFIED MODEL

Although there may be oscillations present in the normal forces due to the locomotive suspension, the suspension of a locomotive is generally very stiff. In automotive applications, the normal forces are typically calculated without considering changes in the vertical, pitch and roll dynamics [34]. Such an approach is attempted here to produce a simplified estimation model. The order of the simplified model is less than the full model, making it less computationally expensive, fewer modelling parameters are needed, and fewer measurements are needed to produce an observable estimator.

4.5.1 Simplified Estimation Model

The suspensions are removed, as shown in Fig. 4.3. It is assumed that all the pitch angles are zero and there is no vertical displacement.

4.5.2 Simplified Kalman-Bucy Filter

The Kalman-Bucy filter for this model simplifies the Kalman-Bucy filter in Section 4.4.5 since the vertical and pitch dynamics are removed. The longitudinal model and wheelset rotational model for each wheelset, as described in Section 4.3.1 and 4.2.3, are combined by choosing the state vector as:

$$\boldsymbol{x} = \begin{bmatrix} v_V & F_{a11} & F_{a12} & F_{a21} & F_{a22} & F_C & \boldsymbol{x}_{\mathrm{red}11}^T & \boldsymbol{x}_{\mathrm{red}12}^T & \boldsymbol{x}_{\mathrm{red}21}^T & \boldsymbol{x}_{\mathrm{red}22}^T \end{bmatrix}^T. \tag{4.47}$$

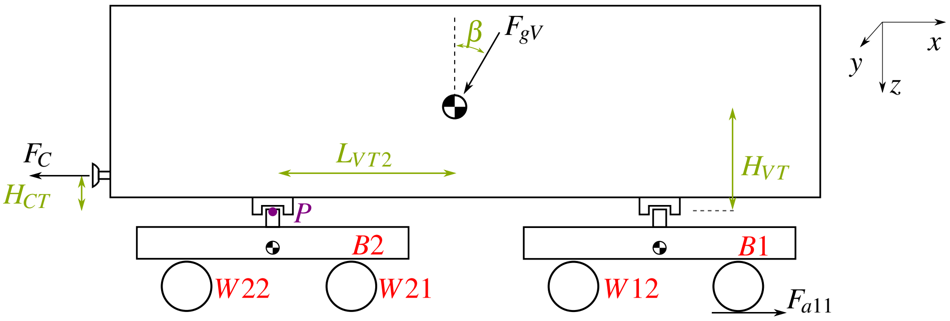

Figure 4.3. Pitch plane of the simplified locomotive. (Front (B_1) and rear (B_2) bogie and the the front (W_{i1}) and rear (W_{i2}) wheelset of each bogie indicated.)

The measured outputs are the same as in Section 4.4.5, but the pitch angle and rate are no longer needed:

$$\boldsymbol{y} = \begin{bmatrix} \dot{v}_V & v_V & \omega_{M11} & \omega_{M12} & \omega_{M21} & \omega_{M22} \end{bmatrix}^T . \tag{4.48}$$

These measurements produce a state-observable model. The interface force vector is:

$$\boldsymbol{f} = \begin{bmatrix} -F_{gL}\sin\beta & T_{M11} & T_{M12} & T_{M21} & T_{M22} \end{bmatrix}^T . \tag{4.49}$$

The process noise covariance matrix is:

$$\boldsymbol{Q} = \text{diag}\begin{bmatrix} 10 & [1\times 10^{12}]_{1\times 5} & [1]_{1\times 20} \end{bmatrix}, \tag{4.50}$$

and the measurement noise covariance matrix is set to:

$$\boldsymbol{R} = \text{diag}\begin{bmatrix} 5 & 10 & [1]_{1\times 4} \end{bmatrix}. \tag{4.51}$$

4.6 NORMAL FORCE ESTIMATION

The normal forces of each wheelset can be computed using the parameters estimated by the full and simplified estimators.

4.6.1 Full Estimator Normal Force Estimate

If the full estimator is used, the normal force estimates are calculated, as shown in (3.44), from:

$$\hat{F}_{Nij} = \hat{F}_{Pij} + \frac{1}{L_{MP}+L_{MW}} T_{Mij} + (\frac{L_{MP}}{L_{MP}+L_{MW}} F_{gMHij} + F_{gWWij})\cos\beta, \tag{4.52}$$

and the primary suspension force estimates are calculated, as shown in (3.14), by:

$$\hat{F}_{Pij} = k_{Pij}(\hat{z}_{Bi} \mp L_{Pij}\hat{\theta}_{Bi}) + c_{Pij}(\hat{\dot{z}}_{Bi} \mp L_{Pij}\hat{\dot{\theta}}_{Bi}). \tag{4.53}$$

4.6.2 Simplified Estimator Normal Force Estimate

For the simplified estimator the normal forces are computed by first considering the locomotive body in Fig. 4.3 in isolation. The pitch dynamics of the body are computed from the moments around P:

$$I_V \dot{\omega}_V - H_{VT} m_V a_x - L_{VT2} m_V a_z = H_{CT} F_C + H_{VT} F_{gV} \sin\beta - L_{VT2} F_{gV} \cos\beta + (L_{VT1} + L_{VT2}) F_{Tz1}, \tag{4.54}$$

where $a_x = \dot{v}_V$ and a_z $(\mathrm{m/s^2})$ are the longitudinal and vertical accelerations, respectively, and the H and L (m) parameters are the geometric heights and lengths as indicated in Fig. 4.3.

Assuming that the pitch rate, ω_V (rad/s), and vertical acceleration, a_z, are negligible, the vertical force between the front bogie and the body, F_{Tz1} (N) as shown in Fig. 4.4, calculated from (4.54) is:

$$F_{Tz1} = \frac{1}{L_{VT1} + L_{VT2}} [-H_{VT} m_V a_V - H_{CT} F_C - H_{VT} F_{gV} \sin\beta + L_{VT2} F_{gV} \cos\beta]. \tag{4.55}$$

Similarly, the vertical force on the rear bogie is:

$$F_{Tz2} = \frac{1}{L_{VT1} + L_{VT2}} [H_{VT} m_V a_V + H_{CT} F_C + H_{VT} F_{gV} \sin\beta + L_{VT1} F_{gV} \cos\beta]. \tag{4.56}$$

By considering the longitudinal dynamics of the bogies, the longitudinal forces between the body and bogies, F_{Txi} (N), are described by:

$$F_{Txi} = F_{ai1} + F_{ai2} - m_{BWi}(a_V + g \sin\beta), \tag{4.57}$$

where m_{BWi} (kg) is the weight of the bogie. With the forces between the bogies and the body defined, the normal forces are found by assuming that the pitch rates and vertical acceleration of the bogies are zero and taking the moments around the point R in Fig. 4.4:

$$F_{Ni1} = \frac{1}{(L_{BNi1} + L_{BNi2})} [-H_{BR} m_{BWi} a_V - H_{TR} F_{Txi} + L_{BNi2}(F_{Tzi} + F_{gWi} \cos\beta) - H_{BR} F_{gWi} \sin\beta] \tag{4.58a}$$

$$F_{Ni2} = \frac{1}{(L_{BNi1} + L_{BNi2})} [H_{BR} m_{BWi} a_V + H_{TR} F_{Txi} + L_{BNi1}(F_{Tzi} + F_{gWi} \cos\beta) + H_{BR} F_{gWi} \sin\beta], \tag{4.58b}$$

Normal force estimates of each wheelset are calculated with (4.55)-(4.58b) using estimates of the acceleration, $\hat{a}_v = \dot{\hat{x}}_1$, adhesion forces, and the coupler force from the estimator in Section 4.5.2.

The same strategy does not directly apply to a co-co locomotive (three wheelsets per bogie). In that case, the normal forces could be resolved by assuming that the normal forces are linearly distributed across the wheelsets of a bogie.

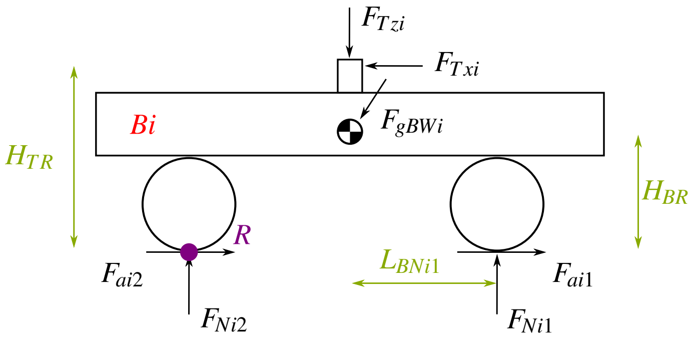

Figure 4.4. A single bogie of the locomotive body. (Front (B_1) and rear (B_2) bogie and the the front (W_{i1}) and rear (W_{i2}) wheelset of each bogie indicated.)

4.7 ADHESION COEFFICIENT AND SLIP RATIO ESTIMATION

Although the adhesion forces will have an observable impact on the pitch dynamics, the wheelset rotational dynamics will dominate the adhesion force estimates. Therefore, it is expected that the full and simplified estimators, as described in Section 4.4.5 and 4.5.2 respectively, will produce estimates with similar accuracy of the adhesion forces, locomotive velocity, and wheel surface velocities.

The slip ratio estimates of each wheelset are calculated by:

$$\hat{\lambda}_{ij} = (\hat{v}_{dLij} - \hat{v}_V)/\hat{v}_V, \tag{4.59}$$

where $\hat{v}_{dLij}$ is calculated from (4.17). The adhesion coefficient estimate is calculated by:

$$\hat{\mu}_{ij} = \hat{F}_{aij}/\hat{F}_{Nij}, \tag{4.60}$$

where $\hat{F}_{Nij}$ is calculated from either (4.52) or (4.58), depending on which estimator is used.

The benefit of the presented estimation methods is that they are linear since the adhesion forces are assumed to be unknown, and none of the non-linear wheel-rail dynamics are included in the models. A drawback of the estimator is that it assumes the radius of the wheels remains constant, which might impact the performance of the estimator during curves. Possible solutions are discussed in Section 2.7.2.

4.8 SIMULATION

A simulation is configured to validate that the desired estimates are produced with sufficient accuracy. In addition, the full and simplified estimator are compared.

4.8.1 Simulation Configuration

A simulation with the same model parameters as in Section 3.8 is configured. However, here the low adhesion condition is chosen for the duration of the simulation. The second notch setting (corresponding to 25% of the maximum tractive power output) is selected for the first five seconds, and the third notch is chosen after that. Zero-mean Gaussian noise is added to the locomotive velocity, acceleration, pitch, and pitch rate measurements with standard deviations of 0.1 m/s, 0.01 m/s^2, 0.01 rad, and 0.01 rad/s, respectively. Modelling errors of 2% are added to all the parameters in the estimation models except for the masses and wheel radii. The wheelset velocity response in Fig. 4.5 shows that the chosen simulation conditions produce unstable slip in all the wheelsets. The slip velocity is much more significant in the front wheelset than the rear wheelset because the normal forces are smaller on the front wheelset. This is primarily due to the centre of gravity of the modelled locomotive being towards the rear. In most cases throughout the rest of this dissertation, only the front bogie front wheelset and rear bogie rear wheelset dynamics are shown since they have the most extreme differences, as seen in Section 3.8.

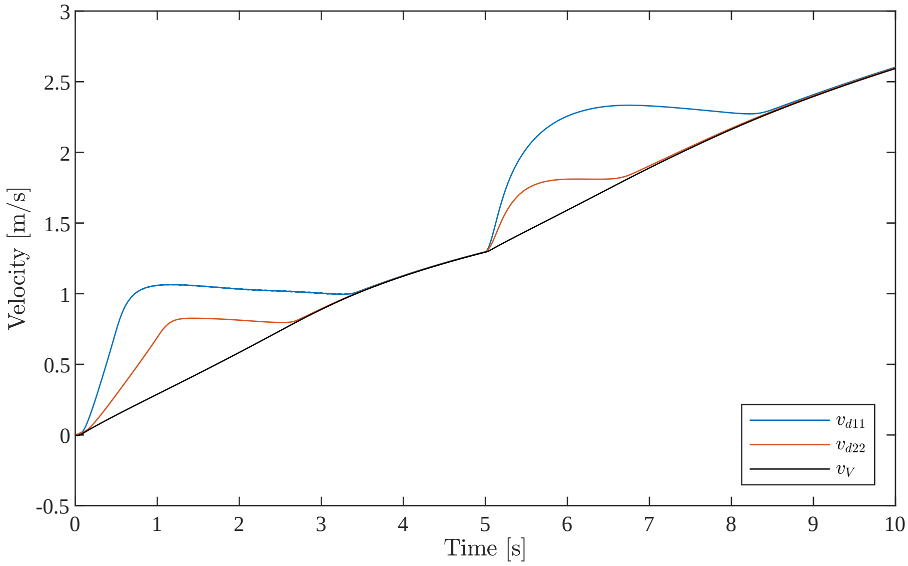

Figure 4.5. Locomotive velocity, v_V, and wheel surface velocities v_{dij} of the front bogie front wheelset and rear bogie rear wheelset.

4.8.2 Adhesion Coefficient Estimation Result

The traction force applied by the motor is approximated with:

$$F_{tij} = T_{Mij}\frac{R}{r}, \tag{4.61}$$

where R is the gear ratio and r (m) is the wheel radius. Fig. 4.6 shows the traction and adhesion forces. During slip, there is a large difference between the traction force and the adhesion force, resulting in acceleration of the wheelset, as shown in Fig. 4.5. As mentioned in Section 3.8.3, re-adhesion is achieved because the torque is gradually decreased as the wheel surface velocities increase, as described in Section 2.3.2.2. While the slip velocities are not excessive, large unstable slip velocities would be observed if higher notch settings are selected. In such cases, slip controllers are needed to ensure re-adhesion.

As explained in Section 4.2, the adhesion force estimate is the sum of the left and right wheel adhesion forces. The estimate in Fig. 4.6 converges within 0.18 s, whereafter the estimation error is maintained below 250 N (1.5%). The estimate of the simplified estimator is shown. Since the wheelset dynamics dominate the estimation of the adhesion force and both estimators use the same model, both produce equally accurate estimates (maximum difference of 19 N between the estimators).

The normal forces and estimates are shown in Fig. 4.7. The full estimator produces more accurate estimates, but the angle sensor noise causes the estimates to deviate from the actual values. Although a 2% modelling error is imposed, the estimator has the benefit in this simulation that it is based on the exact model used in the simulation. It is expected that if the simulation model complexity is increased,

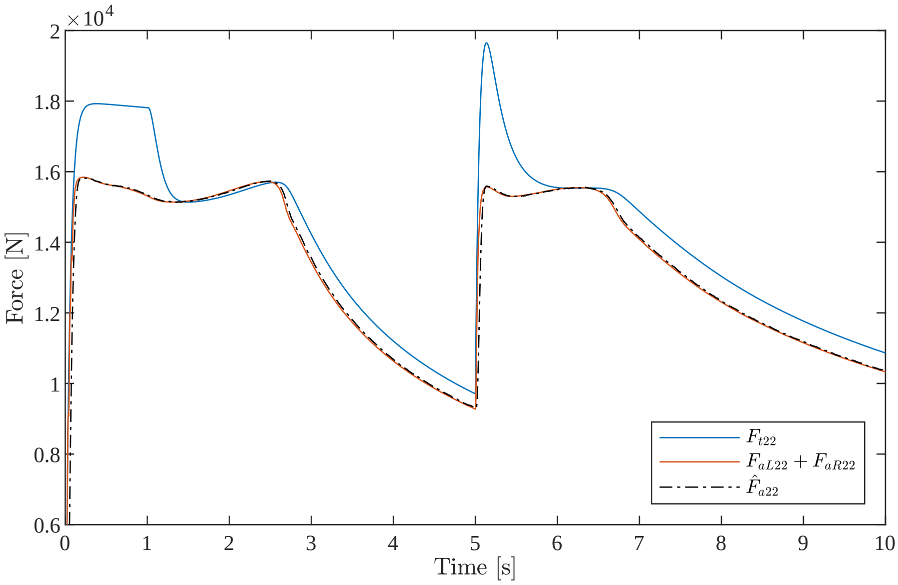

Figure 4.6. Traction force and adhesion force of the rear bogie rear wheelset, and the adhesion force estimate of the simplified estimator.

the normal force estimation errors of the full model will increase.

The simplified estimator reasonably estimates the normal force redistribution during slip, but the oscillations due to the bogie suspensions are not captured. The advantage of this estimator is that it does not require complex modelling of the bogies and can produce normal force estimates that are superior to assuming that the normal forces remain constant. Equally accurate estimates are expected to be produced on a simulation model with higher complexity.

The adhesion coefficient estimates are shown in Fig. 4.8. The adhesion coefficient estimates converge for both estimators within 0.5 s and maintain estimation errors below 0.002 and 0.001 for the simplified and full estimators, respectively. The adhesion coefficients are generally between 0 to 0.6. While the full estimator produces more accurate adhesion coefficient estimates, its marginal improvement does not justify the increase in complexity, as mentioned earlier. The estimate produced by the simplified estimator is sufficiently accurate. Therefore, it is the preferred estimator.

4.8.3 Slip Ratio Estimation Result

Since the simplified estimator is preferred, it will be used in the remaining simulation results. Fig. 4.9 shows the coupler force estimation. If the coupler force estimate is not fast enough, the acceleration and velocity estimates, and thereby the slip ratio estimates, will be affected adversely.

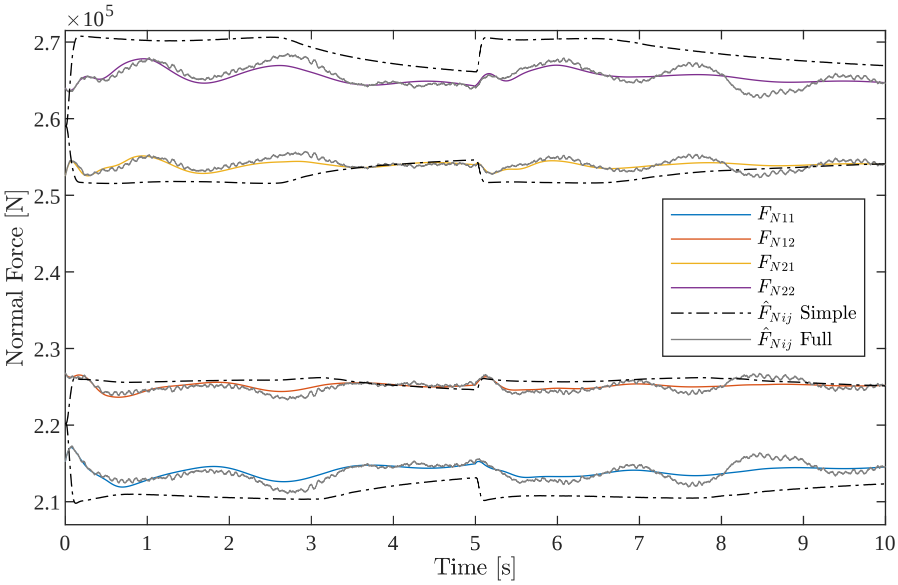

Figure 4.7. Wheel-rail normal forces and estimates of the full and simplified estimators.

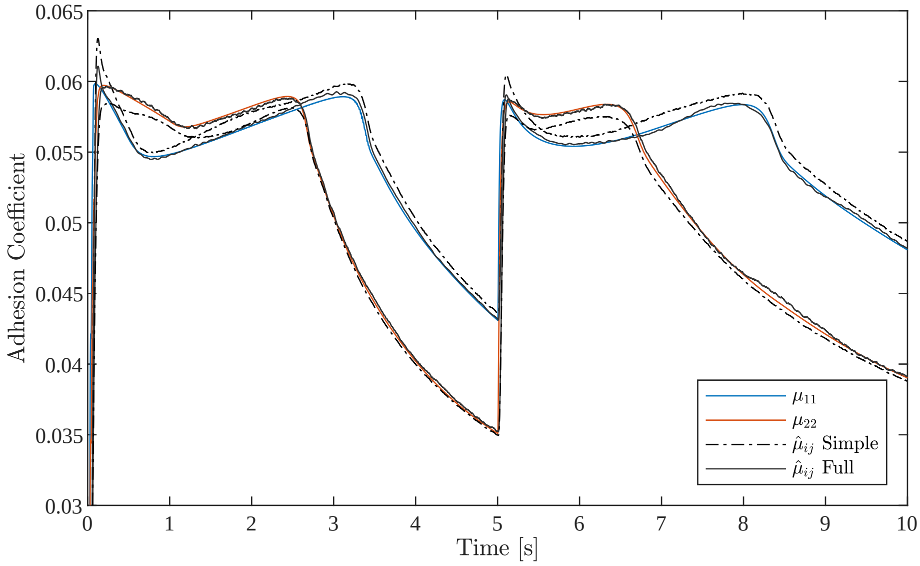

Figure 4.8. Front bogie front wheelset and rear bogie rear wheelset adhesion coefficients and estimates.

As mentioned in Section 4.3, an accurate locomotive velocity estimate is needed. As shown in Fig. 4.10, the estimator removes the noise effectively from the velocity (the estimation error is within 0.008 m/s) and acceleration measurements (the estimator converges within 0.8 s and maintains the estimation error within 0.007 m/s^2). It can be concluded that the combination of the longitudinal model, the chosen measurements, and the coupler force estimation method works well. Fig. 4.10 shows that the rail angle estimation is accurate (the error is within 0.002 rad/s), meaning the filter in Section 4.3.2 works well. The rail angle estimate is used to calculate the gravitational forces, which impact the locomotive velocity and normal force estimates.

The slip ratio estimates are shown in Fig. 4.11. The estimator converges within 0.35 s and maintains estimation errors below 0.026. The slip ratios generally range from zero (no slip) to one (slide during braking). It can be concluded that the presented simplified estimator can produce fast and accurate slip ratio estimates.

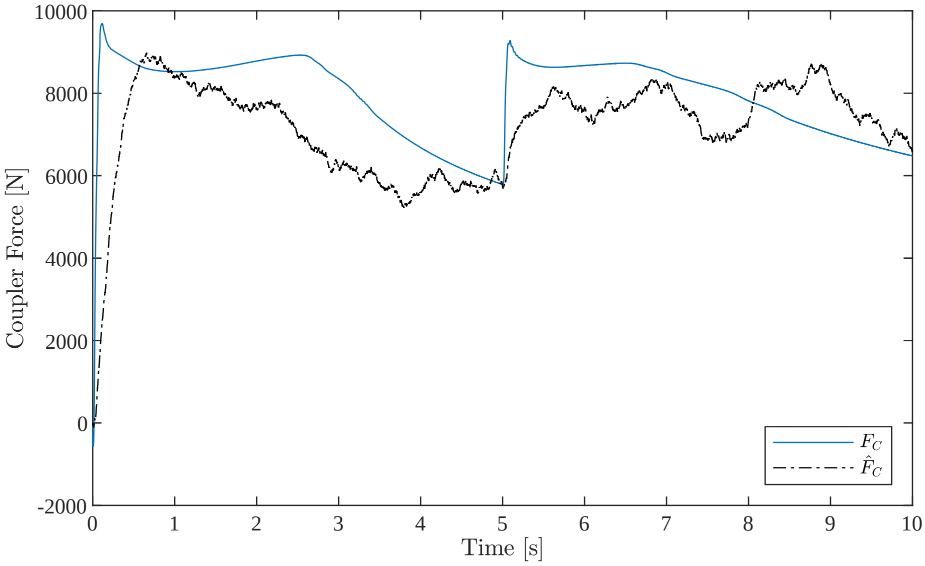

Figure 4.9. Actual, F_C, and estimated, $\hat{F}_C$, coupler forces.

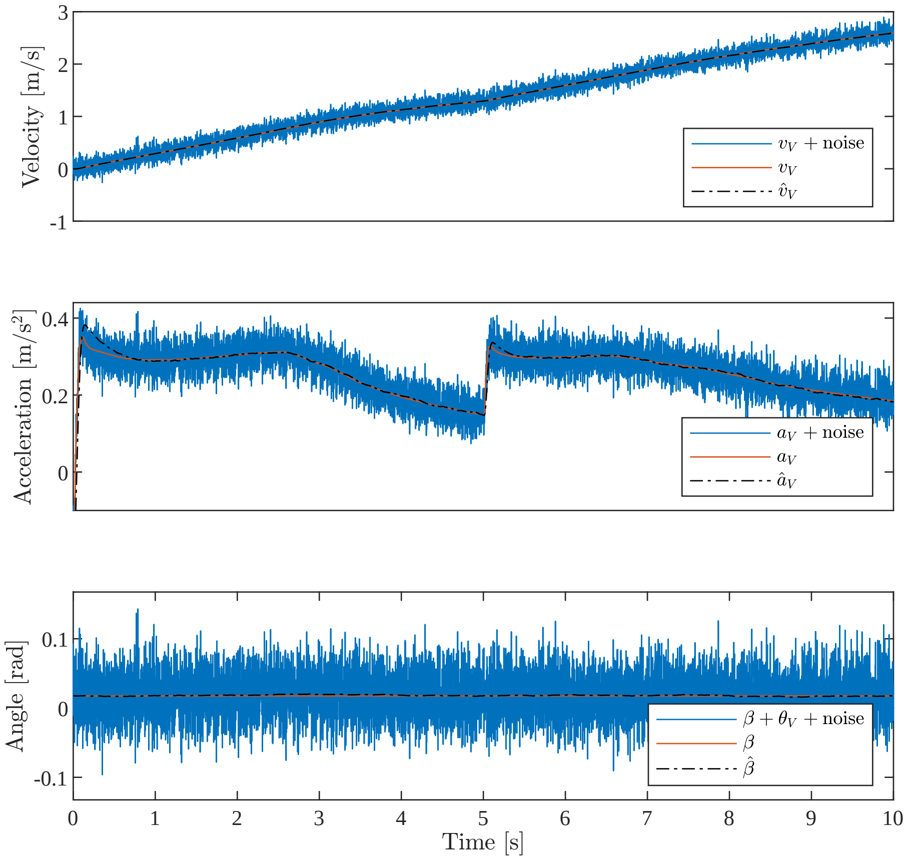

Figure 4.10. Locomotive velocity, acceleration, rail angle, and their estimates.

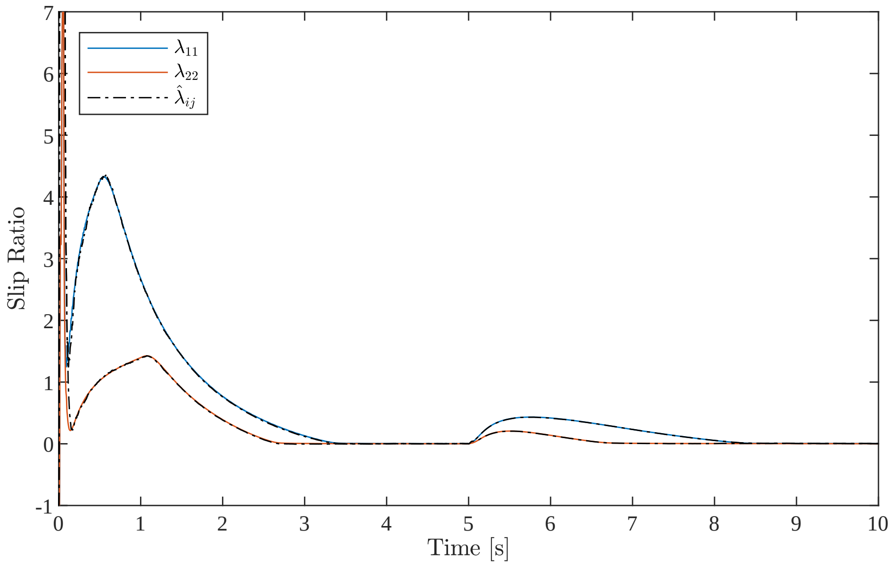

Figure 4.11. Front bogie front wheelset and rear bogie rear wheelset slip ratios and estimates.

4.9 CONCLUSION

Most continuous slip controllers generate a reaction torque based on the current slip ratio estimate and a slip ratio reference. The reference can be generated based on estimates of the slip ratio and adhesion coefficient. If these parameters can be estimated accurately, it is expected to enable continuous controllers to perform better than the traditional rule-based or fuzzy logic controllers.

The dynamics important in slip control were established in Section 3.2, which are the longitudinal, vertical, pitch, and wheelset rotational dynamics. An estimator can be constructed using the simulation model with minor modifications and modelling the adhesion forces and coupler force as unknown disturbances. This estimator requires measurements of the locomotive longitudinal acceleration and velocity, body pitch angle and rate, and the motor angular velocities. The rail angle and motor torque estimates should be provided to the estimator. The estimator is linear since the non-linear wheel-rail dynamics are not included in the estimation model.

Since the pitch angles and vertical displacements of a locomotive are generally small, the estimator can be simplified by removing the pitch and vertical dynamics from it. The body pitch angle and rate measurements are not needed in this estimator. The normal forces are calculated from a pitch-plane model of the locomotive. The simplified estimator is computationally less expensive than the full estimator and requires fewer modelling parameters.

The simulation shows that this estimation method can produce fast and accurate estimates of the adhesion coefficients and slip ratios of each wheelset, which enables efficient slip control.

CHAPTER 5 SLIP CONTROLLER

5.1 CHAPTER OVERVIEW

Slip control aims to maximise adhesion utilisation while preventing unstable slip. The closer the slip ratio operating point can be to the peak (corresponding to maximum adhesion) without causing unstable slip, the higher the tractive force that can be delivered. Therefore, improving a locomotive's slip control improves its hauling capability. Section 5.2 normalizes the wheelset transfer functions to enable the control design. A speed differential controller to control the front wheelsets relative to the speed of the rear (reference) wheelset is presented in Section 5.3. The design of the PI slip controller for the reference wheelset is given in Section 5.4. A novel slip ratio reference adaptation method is presented in Section 5.5. The simulations in Section 5.6 validate the controllers and reference adaptation. The chapter is concluded in Section 5.7.

5.2 PLANT NORMALIZATION

Normalising the input-output behaviour (maximum inputs and outputs of one) simplifies the controller design to ensure disturbance rejection [42].

5.2.1 Wheelset Single Input Single Output Transfer Function

For controller design, converting the state-space system to a single input single output transfer function of the following shape is useful:

$$\tilde{y}(s) = \tilde{G}(s)\tilde{u}(s) + \tilde{G}_d(s)\tilde{d}(s). \tag{5.1}$$

where $\tilde{y}$ is the output, $\tilde{G}$ is the plant transfer function, $\tilde{u}$ is the input, $\tilde{G}_d$ is the disturbance transfer function, and $\tilde{d}$ is the disturbance input. The tilde symbol indicates that the variables and transfer functions are unscaled. The motor angular velocity is chosen as the output, $\tilde{y} = \omega_M$, the input is the motor torque, $\tilde{u} = T_M$, and by assuming the left and right adhesion forces are equal, the disturbance is:

$\tilde{d} = F_a = 2F_{aL} = 2F_{aR}$. Therefore, the input and output matrices are:

$$\boldsymbol{B}_G = \boldsymbol{B}_w \begin{bmatrix} 0 & 0 & 0 & 1 \end{bmatrix}^T \tag{5.2}$$

$$\boldsymbol{B}_{G_d} = \boldsymbol{B}_w \begin{bmatrix} -\frac{1}{2}r_L & -\frac{1}{2}r_R & 0 & 0 \end{bmatrix}^T \tag{5.3}$$

$$\boldsymbol{C}_{\omega_M} = \begin{bmatrix} 0 & 0 & 0 & 0 & 0 & 0 & 0 & 1 \end{bmatrix}, \tag{5.4}$$

from which the transfer functions are calculated:

$$\tilde{G}(s) = \mathrm{tf}(\mathrm{minreal}\left[\begin{array}{c|c} \boldsymbol{A}_w & \boldsymbol{B}_G \\ \hline \boldsymbol{C}_{\omega_M} & 0 \end{array}\right]) \tag{5.5}$$

$$\tilde{G}_d(s) = \mathrm{tf}(\mathrm{minreal}\left[\begin{array}{c|c} \boldsymbol{A}_w & \boldsymbol{B}_{G_d} \\ \hline \boldsymbol{C}_{\omega_M} & 0 \end{array}\right]), \tag{5.6}$$

where $\boldsymbol{B}_w$ and $\boldsymbol{A}_w$ is defined in (4.1a) and tf indicates that the state-space system is converted to a transfer function.

5.2.2 Scaling Factors

A useful scaling for the transfer function is to make the variables less than one in magnitude [42]:

$$y = \tilde{y}/\tilde{e}_{max} = D_e^{-1}\tilde{y} \tag{5.7a}$$

$$u = \tilde{u}/\tilde{u}_{max} = D_u^{-1}\tilde{u} \tag{5.7b}$$

$$d = \tilde{d}/\tilde{d}_{max} = D_d^{-1}\tilde{d}, \tag{5.7c}$$

where $\tilde{e}_{max}$, $\tilde{u}_{max}$, and $\tilde{d}_{max}$ are the maximum allowed output error, maximum input, and maximum expected disturbance, respectively. The scaling factors (D_e, D_u, D_d) are used to scale the transfer functions:

$$G = D_e^{-1}\tilde{G}D_u \tag{5.8}$$

$$G_d = D_e^{-1}\tilde{G}_d D_d. \tag{5.9}$$

By assuming that the deflection in the axles can be ignored, the angular velocity of the motor relative to the wheel surface velocity is $\omega_M \approx R\,\omega_L = R\frac{v_{dL}}{r_L}$. The maximum allowed motor angular velocity error is derived by choosing the maximum allowed slip velocity, $v_s = v_{dL} - v_V$. The choice of the allowed error will determine the required controller bandwidth. Therefore, the maximum allowed slip velocity is a design choice akin to settling time in classical control. However, 1 (m/s) is chosen because a slip velocity greater than 1 m/s will cause unstable slip under most adhesion conditions. The maximum input is the maximum torque that the motor can deliver. The maximum disturbance is determined by assuming that the sum of the left and right wheel adhesion forces will not exceed 95% of the maximum tractive effort the motor can deliver. Therefore, the scaling factors are:

$$D_e = \frac{R}{r_L} v_{s\,max} \tag{5.10a}$$

$$D_u = T_{M max} \tag{5.10b}$$

$$D_d = F_{a\,max} = 0.95 \cdot F_{t\,max} = 0.95 \frac{R}{r} T_{M\,max}. \tag{5.10c}$$

5.3 SPEED DIFFERENTIAL CONTROL

When the locomotive is accelerating, the weight redistribution causes a decrease in the normal force of the front wheelsets and an increase in the rear wheelsets, as seen in Fig. 4.7. The front wheelset (with the smallest normal force) is the most likely to slip. If slip can be prevented in the rear wheelset, its speed can be used as a reference speed to the other wheelsets, thereby reducing the torque if they slip [23].

5.3.1 Design Philosophy

The speed differential controller is implemented with load sharing control, as shown in Fig. 5.1. A feedforward controller applies the torque that is applied to the rear wheelset to the other wheelsets, $T_{M\mathrm{ref}}$ (equal to T of Fig. 2.6) and a feedback speed controller is implemented with the rear wheelset's speed as the reference, $\omega_{M\mathrm{ref}}$.

As mentioned in Section 4.2.1, the full wheelset model has an integrator. Therefore, a simple proportional controller could be sufficient. As shown in Fig. 4.2, the wheelset transfer function has a high gain at the resonant frequencies. Torsional vibrations at these frequencies are prevalent during unstable slip, as seen in Fig. 3.12. Torsional vibration can cause damage to the wheels and should

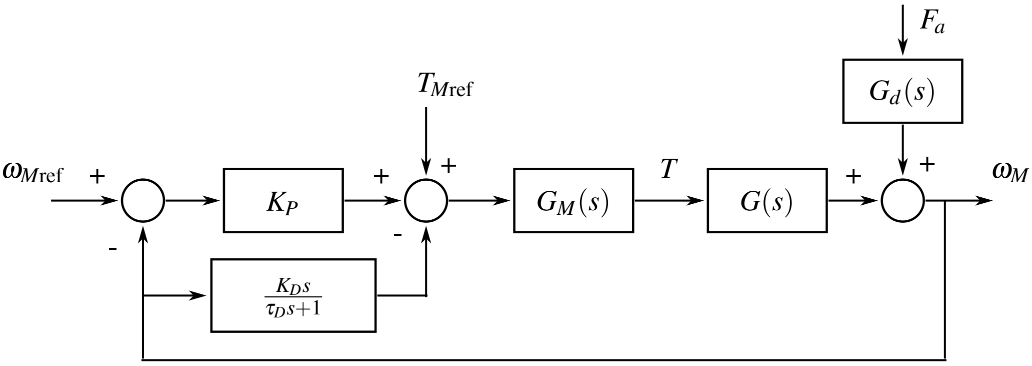

Figure 5.1. Speed differential controller.

be avoided. To prevent these vibrations, the controller's frequency response should drop off at higher frequencies while having a high gain at low frequencies for disturbance rejection. A feedforward derivative term adds damping to prevent these vibrations, as shown in Fig. 5.1. The required bandwidth of the controller is dependent on the disturbance transfer function G_d.

5.3.2 Controller Design

Traction motors are generally controlled using FOC or DTC, producing a fast torque response [1,39]. Therefore, the speed differential controller may be designed based on the wheelset transfer function, $G(s)$ defined in (5.8), by ignoring the motor transfer function, $G_M(s) \approx 1$. The reference torque, $T_{M\mathrm{ref}}$, is not expected to vary much for slip that occurs only in the front wheelsets. Therefore, the speed controller is designed independent of the reference torque. By setting $G_M(s) = 1$ and $T_{M\mathrm{ref}} = 0$, the closed loop transfer function for a feedback controller (without the feedforward derivative term) becomes:

$$y = GK(r-y) + G_d d = L(r-y) + G_d d \tag{5.11a}$$

$$y = (1+L)^{-1}Lr + (I+L)^{-1}G_d d \tag{5.11b}$$

$$= T_c r + SG_d d \tag{5.11c}$$

where K is the feedback controller, L is the loop transfer function, $r = D_e^{-1}\omega_{M\mathrm{ref}}$ is the scaled reference, S is the sensitivity function and T_c is the complimentary sensitivity function [42]. The requirement that the maximum allowed output error is not exceeded ($e = r - y < 1$ for $d < 1$) can only be satisfied if [42]:

$$|S(j\omega)| < 1/|G_d(j\omega)| \quad \forall\omega \tag{5.12}$$

where ω denotes frequency. The loop transfer function for the controller in Fig. 5.1 is:

$$L_{PD}(s) = \frac{K_P G(s)}{1 + K_D \frac{s}{\tau_D s+1} G(s)} \tag{5.13}$$

where K_P is the proportional gain, K_D is the derivative gain, and τ_D is the derivative filter time constant.

The disturbance rejection requirement of (5.12) is plotted in the top plot of Fig. 5.2. Both the proportional (P) controller and the proportional derivative (PD) controller of Fig. 5.1 meet the disturbance rejection requirement. However, the PD controller attenuates the resonant peaks in the loop transfer function much better, as seen in the bottom plot of Fig. 5.2, indicating that it should suppress excessive torsional vibrations. Therefore, the PD controller is preferred. Fig. 5.2 is plotted from the wheelset parameters in Table B.4, B.5 and B.6, and the controller gains in Table B.12.

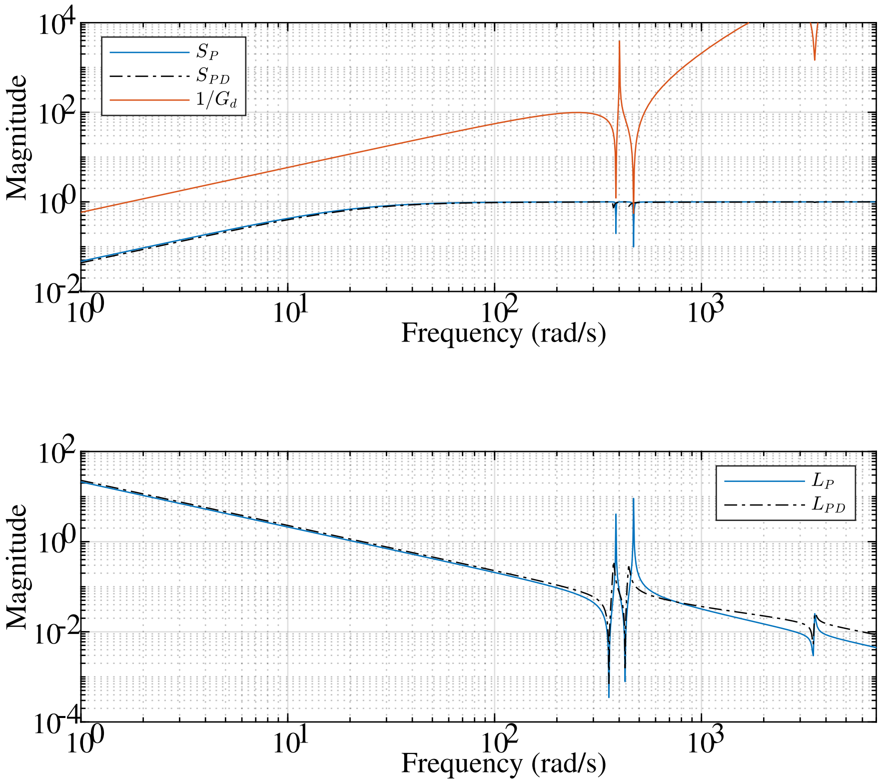

Figure 5.2. Sensitivity (top) and loop (bottom) transfer functions of the PD and P controllers and the inverse of the disturbance transfer function.

5.4 PI SLIP CONTROL

Assuming that a slip ratio reference, λ_R, is provided, the slip controller in Fig. 2.6 should produce a positive reaction torque, T_{react}, during unstable slip ($\hat{\lambda} > \lambda_R$) [9]. After recovering from unstable slip, the reaction torque should be reduced as far as possible without causing unstable slip to reoccur.

5.4.1 Plant Model

The transfer function of the slip controller is described by:

$$\lambda(s) = \frac{\omega_L(s)r - v_V(s)}{v_V(s)} = G_{\text{slip}}(s)(T^* - T_{\text{react}}(s)), \tag{5.14}$$

with:

$$T_{\text{react}}(s) = v_V K_{\text{slip}}(s)(\hat{\lambda}(s) - \lambda_R(s)) \tag{5.15}$$

where $K_{\text{slip}}(s)$ is the PI slip controller. The PI controller is multiplied by v_V to produce a consistent system response independent of the locomotive velocity [9].

By substituting (5.15) into (5.14) and considering the desired torque setpoint, T^*, as a disturbance from the perspective of the slip controller ($T^* = 0$):

$$v_{dL} - v_V = v_V G_{\text{slip}} K_{\text{slip}} ((v_{dL_R} - v_V) - (v_{dL} - v_V)), \tag{5.16}$$

which can be written in the form:

$$y = G_{\text{new}} K_{\text{slip}} (r - y). \tag{5.17}$$

From (5.17), it can be seen that the model for which the PI controller, K_{slip}, should be designed (plant model) is:

$$G_{\text{new}} = \frac{v_{dL} - v_V}{T_{\text{react}}} \approx \frac{v_{dL}}{T_{\text{react}}}, \tag{5.18}$$

where v_V is removed from the model because it can be seen as a constant in this context. The reaction torque, T_{react}, will have an immediate effect on v_{dL}, and the locomotive velocity will change at a much slower rate. Therefore, the transfer function for which the PI controller is designed is:

$$G_{\text{new}}(s) = \text{tf}(\text{minreal} \left[\begin{array}{c|c} \boldsymbol{A}_w & \boldsymbol{B}_G \\ \hline \boldsymbol{C}_{\text{slip}} & 0 \end{array} \right]), \tag{5.19}$$

with:

$$\boldsymbol{C}_{\text{slip}} = \begin{bmatrix} 0 & 0 & 0 & 0 & r_L & 0 & 0 & 0 \end{bmatrix}, \tag{5.20}$$

and $\boldsymbol{A}_w$ and $\boldsymbol{B}_G$ are defined in (4.1a) and (5.2) respectively.

5.4.2 Controller Design

For the particular modelling parameters used, a PI controller with a settling time of 0.88 s provides sufficient disturbance rejection (determined from (5.12)). The system is much more stable in the linear region. Therefore, the PI gains can be interchanged with gains that produce a faster response (2% settling time of 0.5 s) if $\hat{\lambda} < \lambda_R$. Fig. 5.3 shows the PI control system with anti-windup. The anti-windup gain, K_a, is usually chosen as the reciprocal of the proportional gain [39]. The saturation block ensures that the reaction torque stays positive, $T_{\text{react}} > 0$, and less than the desired torque setpoint, T^*. Therefore, the anti-windup gain is chosen as $K_a = 1/K_{p_{\text{fast}}}$, where $K_{p_{\text{fast}}}$ is the proportional gain K_p of the faster PI controller.

The complete slip control scheme consists of the slip controller in Fig. 2.6 and Fig. 5.3 for the rear wheelset and the speed differential controller in Fig. 5.1 for the other wheelsets.

5.5 SLIP RATIO REFERENCE ADAPTATION

As shown in Fig. 2.6 and discussed in Section 5.4, the slip controller requires a slip ratio reference, λ_R. Due to the difficulty in generating a reliable slip ratio reference, a constant reference is often used. As mentioned in Section 2.6, an improvement thereon is creating a peak slip ratio vs locomotive

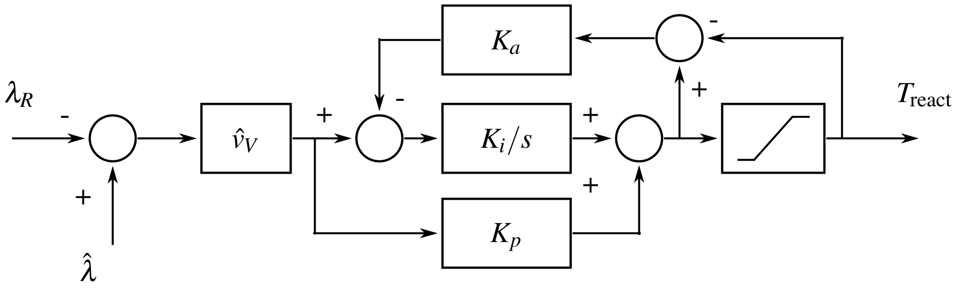

Figure 5.3. Proportional (gain K_p) integral (gain K_i) slip controller with anti-windup (gain K_a).

velocity pseudo-static curve, where the peak slip ratios correspond to the peak values of the adhesion coefficient to slip ratio curves shown in Fig. 2.5 [15]. A lookup table can be constructed to provide the peak slip ratio based on the current locomotive velocity at small velocity intervals. The peak ratios are calculated numerically for a specific adhesion condition from the Polach model as described in Section 2.4.3.

5.5.1 Adhesion Level Dependent Reference Generation

Since the pseudo-static curve is generated for a specific adhesion condition, the produced references will not be optimal for all conditions. The proposed improvement is to store multiple pseudo-static curves corresponding to different adhesion levels and to switch between them by detecting the adhesion level. The generated references for the different adhesion levels are shown in Fig. 5.4.

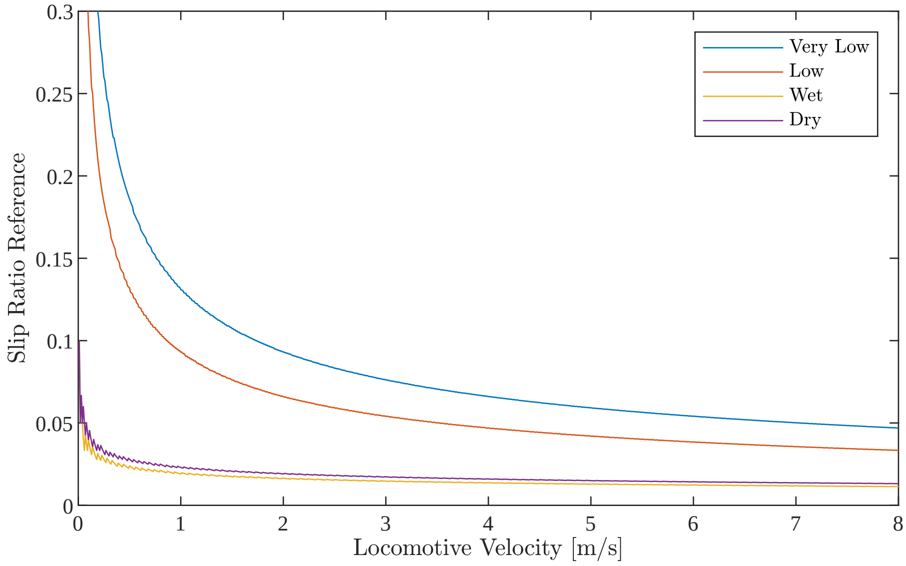

Figure 5.4. Generated slip ratio references for the different adhesion levels.

5.5.2 Adhesion Level Detection

By using the estimated adhesion coefficient, (4.60), slip ratio, (4.59), normal force, (4.58b), and locomotive velocity (second output produced by the estimator in Section 4.5.2), and comparing with the expected adhesion coefficients for different adhesion levels as shown in Fig. 2.4, the adhesion level can be determined.

The expected adhesion coefficient for each adhesion level can be calculated using the Polach model, as described in (3.45), by:

$$(\mu_{\text{actual}})_n = f_{\text{Polach}}(\{\text{Level}\}_n, \hat{F}_N, \hat{\lambda}, \hat{v}_V) \tag{5.21}$$

where $\{\text{Level}\}_n$ groups the model parameters for the specific adhesion level n of the N adhesion levels ($n \in [0, N]$ where 0 is the lowest adhesion level and N is the highest). The parameters used in the Polach model should be as accurate as possible for the specific locomotive, but these are relatively easy to determine from the physical properties of the locomotive [16] and experimental results [9].

Determining the adhesion level is described in Algorithm 1:

Algorithm 1 Adhesion Level Calculation

```
1: Initialize the adhesion level: $n = N$.
2: Using $\hat{F}_N$, $\hat{\lambda}$, and $\hat{v}_V$, calculate $(\mu_{\text{actual}})_{n+1}$, $(\mu_{\text{actual}})_n$, and $(\mu_{\text{actual}})_{n-1}$ from (5.21).
3: $\mu_{\text{Top}} = \frac{1}{2}[(\mu_{\text{actual}})_{n+1} + \mu_{\text{actual}})_n]$
   $\mu_{\text{Bot}} = \frac{1}{2}[(\mu_{\text{actual}})_n + \mu_{\text{actual}})_{n-1}]$
4: if $n < N$ and $\hat{\mu} > \mu_{\text{Top}}$ then
5:     $n = n + 1$
6: else if $n > 0$ and $\hat{\mu} < \mu_{\text{Bot}}$ then
7:     $n = n - 1$
8: end if
9: Return to 2.
```

Here μ_{Top} and μ_{Bot} are the upper and lower adhesion level detection crossover points. The calculated level, n, determines which pseudo-static slip ratio reference to the locomotive velocity curve should be used to produce the reference, λ_R.

The benefit of this approach to the preferred adaptation approach in literature (mainly based on polynomial fitting algorithms [8]) is that this adaptation is fast. Even if the wrong adhesion level is identified, a slip ratio reference will be produced that will prevent excessive slip. Due to the discrete nature of the pseudo-static curves and contact dynamics modelling errors, the generated slip ratio reference will not be the exact peak, but it produces an adaptive reference which is superior to a constant reference or a single pseudo-static curve.

5.6 SIMULATION

In this simulation, the speed differential controller, slip controller, and slip ratio reference generator presented in this chapter, and the simplified estimator presented in Chapter 4 are combined and tested using the simulation model presented in Chapter 3.

5.6.1 Simulation Configuration

A simulation with the same model parameters as in Section 4.8 is configured. The same 2% estimation modelling errors and measurement noise apply. The eighth notch is selected (maximum tractive power). The adhesion conditions are chosen to be *wet* for $t \in [0,3)$ s, *dry* for $t \in [3,6)$ s, *low* for $t \in [6,14)$ s, and *very low* for $t \in [14,20)$ s to test the slip controller under significant changes in adhesion conditions. The adhesion parameters defined in [19] and given in Tables B.1 and B.2 are used.

5.6.2 Simulation Results

The simulation velocity response is shown in Fig. 5.5. During the *wet* and *dry* adhesion conditions, the slip ratio of the rear wheelset is well within the stable/linear region, and torque reduction is unnecessary. However, during the *wet* condition, the front wheelset experiences slip as seen in Fig. 5.6, which is quickly suppressed by the speed differential controller (see the reduction in T_{11} in Fig. 5.7).

When the adhesion level drops to the *low* and *very low* conditions, unstable slip occurs (the maximum adhesion point is exceeded). As seen in Fig. 5.8, the adhesion coefficient changes suddenly when the adhesion level is altered, causing an error in the adhesion coefficient estimate. However, the estimator converges within 15 ms, which allows for fast detection of changes in the adhesion levels.

As described in Section 5.5, the detected adhesion level is used to switch between the pseudo-static curves relating to the desired slip ratios based on the locomotive velocity. Fig. 5.6 shows that the correct slip ratio reference is detected when unstable slip occurs during *low* adhesion. It is more difficult to determine the adhesion level if the operating point is in the stable region because the adhesion surfaces are close in the stable region. However, an accurate slip ratio reference is only needed during unstable slip.

When the adhesion level drops, unstable slip occurs, and the slip ratio of the rear wheelset, λ_{22}, overshoots the reference, as shown in Fig. 5.6. As shown in Fig. 5.7, the slip controller reacts

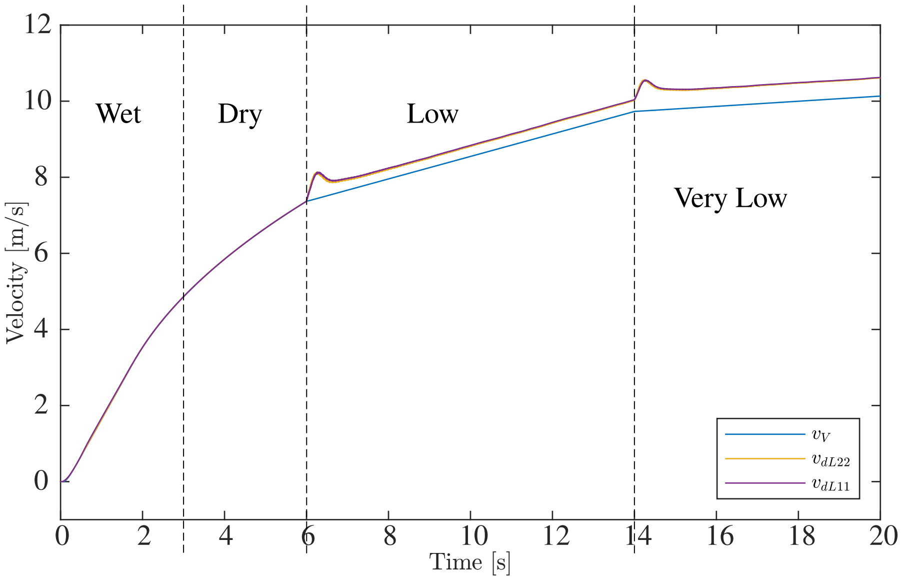

Figure 5.5. Locomotive velocity, v_V, and left wheel surface velocities v_{dLij} of the front bogie front wheelset and rear bogie rear wheelset. Wet, Dry, Low, and Very Low refer to the change in adhesion conditions.

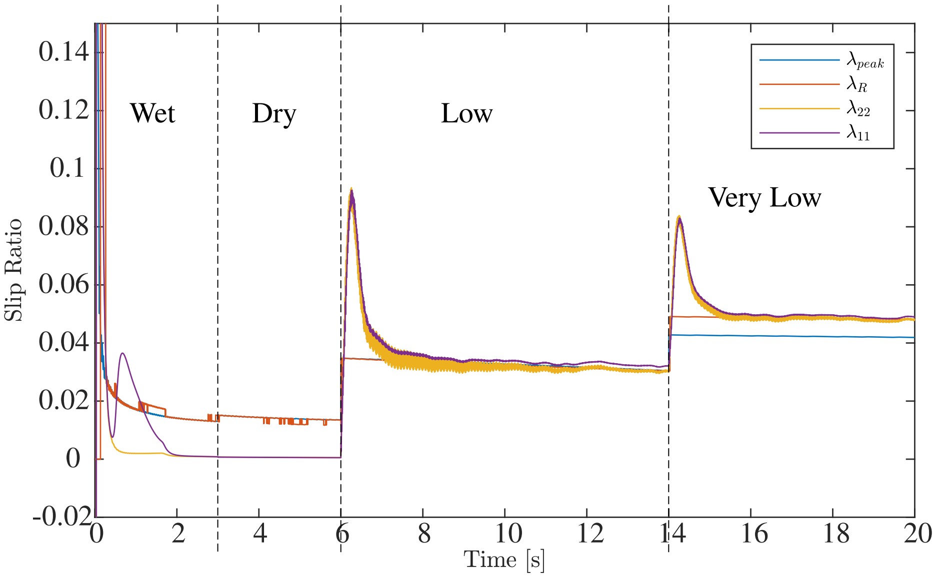

Figure 5.6. Peak slip ratio reference, λ_{peak}, calculated slip ratio reference, λ_R, and the actual slip ratio of the rear bogie rear wheelset, λ_{22}, and front bogie front wheelset, λ_{11}.

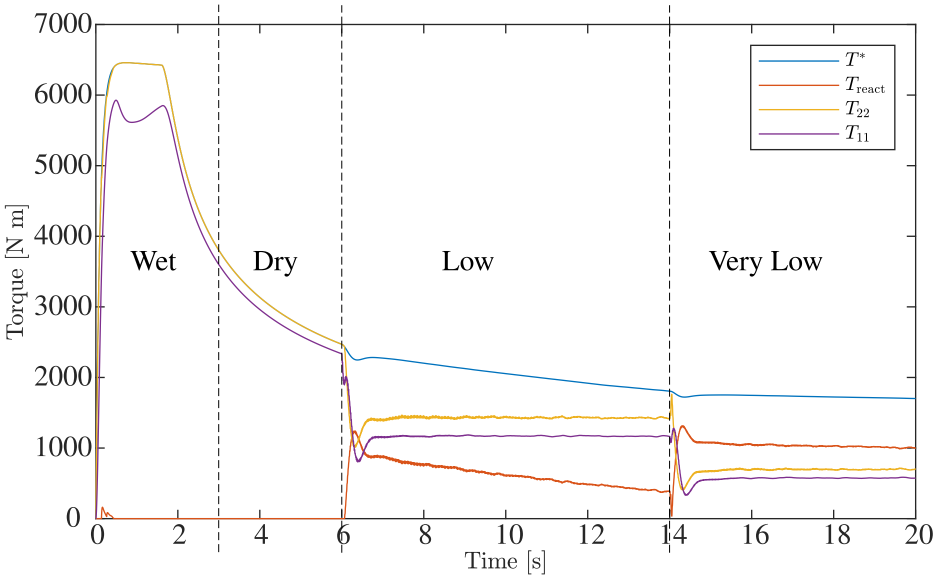

Figure 5.7. Rear wheelset PI controller torque set-point, T^*, reaction torque, T_{react}, and applied torque, T_{22}, as well as the applied torque of the front wheelset, T_{11}, computed with the speed differential controller.

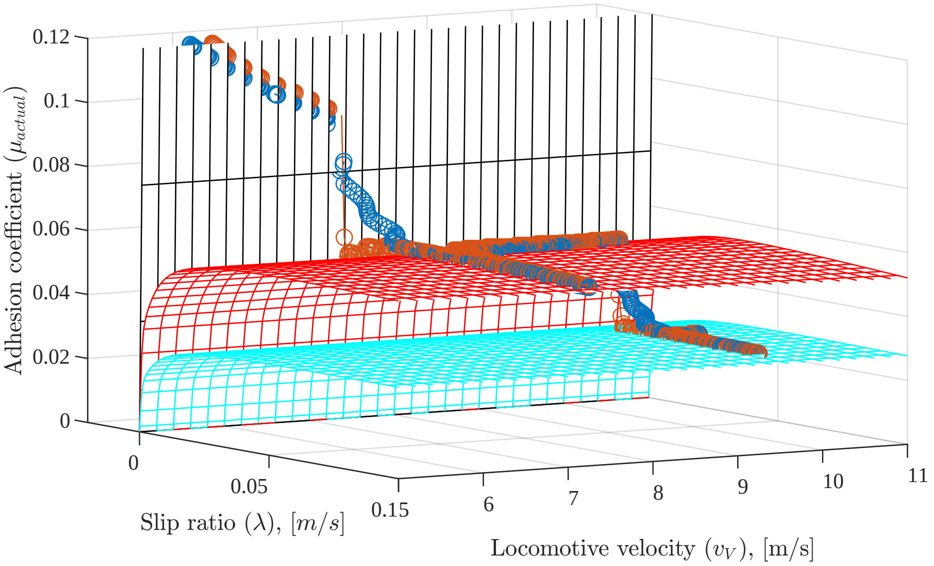

Figure 5.8. Actual (red) and estimated (blue) operating point of the rear bogie rear wheelset plotted onto the *dry* (black), *low* (red), and *very low* (cyan) adhesion surfaces of Fig. 2.4.

by producing a reaction torque and the unstable slip is suppressed within 1.4 s. After that, the slip controller effectively prevents unstable slip, from which it can be concluded that the anti-windup functions as desired. The reference for the *very low* adhesion is purposefully scaled to exceed the peak reference by 15%. Even though the reference is within the unstable slip region, the slip controller can prevent the slip velocity from increasing uncontrollably. Since operating in the unstable slip region is undesirable, the references used in practice should be less than the peak slip ratios.

5.7 CONCLUSION

By ensuring that the wheelset with the largest normal force does not slip (generally the rear wheelset during acceleration), the slip in the other wheelsets is easily prevented with a speed differential controller that tracks the speed of the reference (rear) wheelset.

A slip controller is needed to prevent unstable slip in the reference wheelset. As mentioned in Section 2.5.6, PI controllers are typically tuned for a specific linear model that may make them poorly suited to variable wheel-rail conditions. A few modifications to the PI controller produce a slip controller with satisfactory performance. The controller is multiplied by the locomotive velocity to produce a consistent system response independent of the locomotive velocity. The PI controller requires anti-windup to gradually reduce the reaction torque in the stable region without causing unstable slip. Due to the inherent stability in the linear (stable) region, faster PI gains can be used in this region.

Controllers such as SMC and MPC are expected to provide better tracking performance and warrant further investigation. However, the performance of most continuous controllers is limited by the quality of the provided slip ratio reference and accurate estimation of the slip ratio [8]. Therefore, this research focuses on enabling slip control and reference generation by effective estimation. While the presented slip control might not be optimal, it achieved fast re-adhesion and maintained the operating point on the peak without causing unstable slip to reoccur. It can be concluded that the aim of enabling slip control by effective estimation was achieved.

This chapter's most significant and unique contribution is the novel slip ratio reference adaptation method, which generates a slip-ratio reference based on the detected adhesion level. The adhesion level is detected by comparing the estimated and expected adhesion coefficient for different adhesion levels at the estimated adhesion ratio and locomotive velocity.

The presented simulation has the benefit that the adhesion surfaces used in the adhesion level calculation correspond exactly with those used in the simulation. In reality, capturing the adhesion coefficients produces clouds of points rather than discrete levels. Therefore, this method cannot produce precise slip ratio references, but it provides a method of adapting the reference to a suitable value during varying adhesion conditions. Here, four discrete levels have been used, but multiple levels based on experimental data should be constructed in practice. If unstable slip becomes prevalent, the adhesion surfaces used should be re-tuned and the slip ratio references should be generated more conservatively. However, it was demonstrated in the simulation that even if the generated reference is larger than the slip ratio peak, the control should still be able to prevent excessive unstable slip. Therefore, this method can provide much more adhesion utilisation (operating closer to the peak) than by selecting a constant slip ratio reference or a single pseudo-static slip ratio reference curve.

Using multiple pseudo-static curves for different adhesion levels has two additional benefits. Firstly, the estimator allows for fast detection of the adhesion level, allowing for rapid adaptation of the slip ratio reference. Secondly, since the slip ratio references are computed offline, it is guaranteed (so long as the locomotive velocity estimate is accurate) that the reference generation will not become unstable (generating unreasonably large or small references), as is possible with the fuzzy logic and extremum seeking methods mentioned in Section 2.6.

CHAPTER 6 CONCLUSION

The aim of this dissertation is to determine if a slip controller can be developed using model-based estimation suitable for real-time control on board a locomotive.

Slip control is difficult because of the uncertainty due to the inherent non-linearities of the adhesion characteristic curve and the unpredictable external environment. The adhesion coefficient cannot be measured directly, and it is difficult to determine whether the maximum adhesion point has been exceeded. Therefore, rule-based and fuzzy logic controllers have predominantly been used.

6.1 FINDINGS

Developing an improved continuous slip controller using model-based estimation was structured by finding solutions to the sub-questions/problems listed in Section 1.2. The **first problem** was finding the necessary level of complexity of the locomotive dynamics modelling for simulation.

Slip largely depends on the wheel-surface conditions, the normal force, and the applied torque/force. While there are many different modelling approaches in the literature, it was found that most of these lacked either the pitch dynamics complexity to capture the normal force distributions or the wheelset rotational dynamics complexity to capture the possible torsional vibrations. Consideration is needed in controller design to prevent torsional vibrations.

A new simulation model was developed that includes the longitudinal, pitch, vertical, and wheelset rotational dynamics. It includes a unique approach to the coupler force by modelling the wagons using a single-axle wheelset model. The model captured the normal force oscillations and the wheelset torsional vibrations. The presented simulation model has an order of 61, indicating a balanced complexity for slip control-relevant dynamics simulation, enabling efficient analysis and evaluation.

The **second problem** involved finding the required level of complexity of the estimation model. While the simulation model provides a good starting point for constructing the estimation model, simplifying the estimator by removing the vertical and pitch dynamics from the model used in the Kalman filter was beneficial.

The **third problem** was aimed at determining which relevant parameters can (or should) be measured and which parameters can (or should) be estimated. The simplified estimator requires measurements of the locomotive velocity, acceleration, and motor angular rates, and the rail angle and motor torques should be provided. These parameters are easily measured or determined on modern locomotives. The simplified estimator produces fast and accurate estimates of the adhesion forces and slip ratios of each wheelset. A pitch plane model can be used to produce the normal force estimates. The adhesion coefficient estimates are calculated by dividing the adhesion force by the normal force estimates.

The **fourth and final problem** involved finding a suitable slip control strategy. This dissertation showed that a continuous controller, such as an adaptive PI controller with anti-windup, can produce reliable slip control given a slip ratio reference and estimate. A novel slip-ratio adaptation method is presented, generating a slip-ratio reference based on the detected adhesion level. The adhesion level is detected by comparing the estimated and expected adhesion coefficient for different adhesion levels at the estimated adhesion ratio and locomotive velocity.

In summary:

- The proposed slip controller with reference adaptation and estimator is simple to implement practically. Complex locomotive modelling is not required.
- The controller adapts to changes in the adhesion conditions without requiring prior knowledge of the rail conditions or geometry.
- This system can be implemented on modern locomotives with accurate individual wheelset torque control.
- The locomotive requires only a Doppler radar (to measure the longitudinal velocity) and an inertial measurement unit (to determine the longitudinal acceleration and rail angle) in addition to a modern locomotive's existing sensors onboard.

It can be concluded that the aim of enabling slip control using model-based estimation suitable for real-time control onboard a locomotive was achieved.

6.2 FUTURE WORK

This dissertation provides a simulation model, estimator, slip controller and a slip ratio reference adaptation algorithm. Since each of these informs the fidelity required of the others. Therefore, the limited scope of this dissertation uncovers several areas warranting further research.

The objective of the simulation model here was to provide sufficient variability to variables controllable by the slip controller. However, since it is used as the basis for the design of the estimation model. Therefore, validating the accuracy simulation model using a multi-body simulation or experimental results is recommended for future work.

As mentioned in Section 4.7, the estimator is sensitive to wheel radius errors. Estimating the wheel radius, as discussed in Section 2.7.2, should be investigated. Model errors and sensor noise are added to the simulations to provide insight into the robustness of the estimator. However, a more formal study into estimator robustness against parameter errors and sensor noise could be performed.

The cost of a powerful onboard processor to perform the estimator and slip-controller could easily be justified relative to the locomotive cost and the potential performance gain. However, discretising the algorithms and quantifying the computational load may be insightful and necessary for practical implementation.

As mentioned in Section 5.7, controllers such as SMC and MPC are expected to provide better tracking performance and warrant further investigation.

As mentioned in Section 5.7, four discrete adhesion levels have been used in this dissertation. Multiple levels based on experimental data should be constructed, as discussed in Section 5.5.2.

This work would benefit from the simulation of the estimator and controller in a multi-body simulation and experimental validation in a full-scale implementation. Full-scale implementation may be costly, so the slip ratio reference adaptation algorithm and slip controller can be tested on a lab-scale twin disc machine [26].

REFERENCES

[1] D. Ronanki, S. A. Singh, and S. S. Williamson, "Comprehensive topological overview of rolling stock architectures and recent trends in electric railway traction systems," *IEEE Transactions on Transportation Electrification*, vol. 3, no. 3, pp. 724–738, 2017.

[2] S. Wang, W. Zhang, J. Huang, Q. Wang, and P. Sun, "Adhesion control of heavy-duty locomotive based on axle traction control system," *IEEE Access*, vol. 7, pp. 164 614–164 622, 2019.

[3] P. Pichlik, "Locomotive wheel slip controller based on power dissipation in wheel-rail contact," in *2019 International Conference on Electrical Drives & Power Electronics (EDPE)*. The High Tatras, Slovakia: IEEE, 24-26 Sep. 2019, pp. 211–216.

[4] M. Spiryagin, P. Wolfs, C. Cole, V. Spiryagin, Y. Q. Sun, and T. McSweeney, *Design and Simulation of Heavy Haul Locomotives and Trains*. Boca Raton: CRC/Taylor & Francis, 2017.

[5] M. Spiryagin, Y. Q. Sun, C. Cole, S. Simson, and I. Persson, "Development of traction control for hauling locomotives," *Journal of System Design and Dynamics*, vol. 5, no. 6, pp. 1214–1225, 2011.

[6] T. X. Mei and H. Li, "Measurement of absolute vehicle speed with a simplified inverse model," *IEEE Transactions on Vehicular Technology*, vol. 59, no. 3, pp. 1164–1171, 2010.

[7] S. Iwnicki, *Handbook of Railway Vehicle Dynamics*. Boca Raton: CRC/Taylor & Francis, 2006.

[8] F. Pretagostini, L. Ferranti, G. Berardo, V. Ivanov, and B. Shyrokau, "Survey on wheel slip

control design strategies, evaluation and application to antilock braking systems," *IEEE Access*, vol. 8, pp. 10 951–10 970, 2020.

[9] D. Savitski, D. Schleinin, V. Ivanov, and K. Augsburg, "Robust continuous wheel slip control with reference adaptation: Application to the brake system with decoupled architecture," *IEEE Transactions on Industrial Informatics*, vol. 14, no. 9, pp. 4212–4223, 2018.

[10] Y. Tian, "Fuzzy logic creep control for a 2d locomotive dynamic model under transient wheel-rail contact conditions," in *Computers in Railways XIV*, ser. WIT Transactions on The Built Environment, C. Brebbia, N. Tomii, P. Tzieropoulos, J. Mera, B. Ning, W. J. T. Daniel, S. Liu, and P. A. Meehan, Eds. WIT Press, Southampton, UK, 2014, pp. 885–896.

[11] D. Tavernini, F. Vacca, M. Metzler, D. Savitski, V. Ivanov, P. Gruber, A. E. Hartavi, M. Dhaens, and A. Sorniotti, "An explicit nonlinear model predictive ABS controller for electro-hydraulic braking systems," *IEEE Transactions on Industrial Electronics*, vol. 67, no. 5, pp. 3990–4001, 2020.

[12] J. He, G. Liu, J. Liu, C. Zhang, and X. Cheng, "Identification of a nonlinear wheel/rail adhesion model for heavy-duty locomotives," *IEEE Access*, vol. 6, pp. 50 424–50 432, 2018.

[13] P. D. Hubbard, G. A. Amarantidis, and C. P. Ward, "Leaves on the line: Low adhesion detection in railways," *IFAC-PapersOnLine*, vol. 49, no. 21, pp. 467–472, 2016.

[14] D. Kun, L. Kaijun, and X. Qunsheng, "Application of unscented Kalman filter for the state estimation of anti-lock braking system," in *2006 IEEE International Conference on Vehicular Electronics and Safety*. Shanghai, China: IEEE, 13-15 Dec. 2006, pp. 130–133.

[15] E. Kayacan, Y. Oniz, and O. Kaynak, "A grey system modeling approach for sliding-mode control of antilock braking system," *IEEE Transactions on Industrial Electronics*, vol. 56, no. 8, pp. 3244–3252, 2009.

[16] Ö. Ararat and M. T. Söylemez, "Robust velocity estimation for railway vehicles," *IFAC-PapersOnLine*, vol. 50, no. 1, pp. 5961–5966, 2017.

[17] C. P. Ward, R. M. Goodall, and R. Dixon, "Contact force estimation in the railway vehicle wheel-rail interface," *IFAC Proceedings Volumes*, vol. 44, no. 1, pp. 4398–4403, 2011.

[18] O. Polach, "Creep forces in simulations of traction vehicles running on adhesion limit," *Wear*, vol. 258, pp. 992–1000, 2005.

[19] G. Charles, R. Goodall, and R. Dixon, "Model-based condition monitoring at the wheel–rail interface," *Vehicle System Dynamics*, vol. 46, no. sup1, pp. 415–430, 2008.

[20] J. J. Kalker, *Three-Dimensional Elastic Bodies in Rolling Contact*. Dordrecht, Netherlands: Kluwer Academic Publishers, 1990.

[21] S. H. Park, J. S. Kim, and J. J. Choi, "Reference slip ratio generation and adaptive sliding mode control for railway rolling stocks," *International Journal of Precision Engineering and Manufacturing*, vol. 10, no. 2, pp. 39–44, 2009.

[22] P. Pichlik and J. Zdenke, "Locomotive wheel slip control method based on an unscented Kalman filter," *IEEE Transactions on Vehicular Technology*, vol. 16, no. 7, pp. 5730–5739, 2018.

[23] I. Yasuoka, Y. Mochizuki, S.-I. Toda, Y. Nakazawa, G. Hongguang, and L. Huiyan, "Consideration of wheel slip and readhesion control for induction traction motor electric locomotives with individual traction control," *Electrical Engineering in Japan*, vol. 169, no. 3, pp. 55–64, 2009.

[24] S. Wang, J. Xiao, J. Huang, and H. Sheng, "Locomotive wheel slip detection based on multi-rate state identification of motor load torque," *Journal of the Franklin Institute*, vol. 353, no. 2, pp. 521–540, 2016.

[25] M. Djukić, S. Rusov, and Z. Mitrović, "A fuzzy model for an increase in locomotive traction force," *Transport*, vol. 25, no. 1, pp. 36–45, 2010.

[26] S. Sadr, D. A. Khaburi, and J. Rodriguez, "Predictive slip control for electrical trains," *IEEE Transactions on Industrial Electronics*, vol. 63, no. 6, pp. 3446–3457, 2016.

[27] K. Ohishi, K. Nakano, I. Miyashita, and S. Yasukawa, "Anti-slip control of electric motor coach based on disturbance observer," in *5th International Workshop on Advanced Motion Control*. Coimbra, Portugal: IEEE, 29 Jun. - 1 Jul. 1998.

[28] M. Green and D. J. N. Limebeer, *Linear Robust Control*, 2nd ed. Newburyport: Dover, 2012.

[29] N. Zengin, H. Zengin, B. Fidan, and A. Khajepour, "Slip ratio optimization in vehicle safety control systems using least-squares based adaptive extremum seeking," in *2020 IEEE International Conference on Systems, Man, and Cybernetics (SMC)*. Toronto, ON, Canada: IEEE, 11-14 Oct. 2020, pp. 1445–1450.

[30] K. Berntorp, "Joint wheel-slip and vehicle-motion estimation based on inertial, GPS, and wheel-speed sensors," *IEEE Transactions on Control Systems Technology*, vol. 24, no. 3, pp. 1020–1027, 2016.

[31] G. Charles, R. Goodall, and R. Dixon, "Wheel-rail profile estimation," in *2006 IET International Conference On Railway Condition Monitoring*, Birmingham, United Kingdom, 29-30 Nov. 2006, pp. 32–37.

[32] P. D. Hubbard, C. Ward, R. Dixon, and R. Goodall, "Models for estimation of creep forces in the wheel/rail contact under varying adhesion levels," *Vehicle System Dynamics*, vol. 52, no. 1, pp. 370–386, 2014.

[33] K. Ohishi, S. Kadowaki, Y. Smizu, T. Sano, S. Yasukawa, and T. Koseki, "Anti-slip readhesion control of electric commuter train based on disturbance observer considering bogie dynamics," in *IECON 2006 - 32nd Annual Conference on IEEE Industrial Electronics*. Paris, France: IEEE, 6-10 Nov. 2006, pp. 5270–5275.

[34] A. Rezaeian, R. Zarringhalam, S. Fallah, W. Melek, A. Khajepour, S.-K. Chen, N. Moshchuck, and B. Litkouhi, "Novel tire force estimation strategy for real-time implementation on vehicle applications," *IEEE Transactions on Vehicular Technology*, vol. 64, no. 6, pp. 2231–2241, 2015.

[35] C. P. Ward, R. M. Goodall, R. Dixon, and G. A. Charles, "Adhesion estimation at the wheel–rail

interface using advanced model-based filtering," *Vehicle System Dynamics*, vol. 50, no. 12, pp. 1797–1816, 2012.

[36] M. Spiryagin, K. S. Lee, and H. H. Yoo, "Control system for maximum use of adhesive forces of a railway vehicle in a tractive mode," *Mechanical Systems and Signal Processing*, vol. 22, no. 3, pp. 709–720, 2008.

[37] A. W. Ndiaye, M. Cassaro, C. Combier, J.-M. Biannic, and C. Roos, "On-ground aircraft modeling for advanced braking control system design," in *2022 European Control Conference (ECC)*, London, United Kingdom, 12-15 Jul. 2022, pp. 649–656.

[38] R. Jibrin, S. Hillmansen, and C. Roberts, "Convex optimization for fuel cell hybrid trains: Speed, energy management system, and battery thermals," in *2022 European Control Conference (ECC)*, London, United Kingdom, 12-15 Jul. 2022, pp. 2130–2136.

[39] S.-H. Kim, *Electric Motor Control*. Amsterdam, Netherlands: Elsevier Inc., 2017.

[40] K. Glover, "All optimal Hankel-norm approximations of linear multivariable systems and their L_∞ -error bounds," *International Journal of Control*, vol. 39, no. 6, pp. 1115–1193, 1984.

[41] M. S. Grewal and A. P. Andrews, *Kalman Filtering: Theory and Practice Using MATLAB*, 4th ed. Hoboken, New Jersey: John Wiley & Sons, Inc., 2015.

[42] S. Skogestad and I. Postlethwaite, *Multivariable Feedback Control: Analysis and Design*. Hoboken, NJ, USA: John Wiley & Sons, Inc., 2005.

APPENDIX A SIMULATION MODEL MATRICES

A.1 LONGITUDINAL DYNAMICS MATRICES

$$\boldsymbol{q}_{\text{long}} = \begin{bmatrix} x_V & x_{B1} & x_{W11} & x_{W12} & x_{B2} & x_{W21} & x_{W22} \end{bmatrix}^T \tag{A.1}$$

$$\boldsymbol{M}_{\text{long}} = \text{diag}\begin{bmatrix} m_V & m_{B1} & m_{W11} & m_{W12} & m_{B2} & m_{W21} & m_{W22} \end{bmatrix} \tag{A.2}$$

$$\boldsymbol{C}_{\text{long}} = \begin{bmatrix} c_{T1}+c_{T2} & -c_{T1} & 0 & 0 & -c_{T2} & 0 & 0 \\ -c_{T1} & c_{T1} & 0 & 0 & 0 & 0 & 0 \\ 0 & 0 & 0 & 0 & 0 & 0 & 0 \\ 0 & 0 & 0 & 0 & 0 & 0 & 0 \\ -c_{T2} & 0 & 0 & 0 & c_{T2} & 0 & 0 \\ 0 & 0 & 0 & 0 & 0 & 0 & 0 \\ 0 & 0 & 0 & 0 & 0 & 0 & 0 \end{bmatrix} \tag{A.3}$$

$$\boldsymbol{K}_{\text{long}} = \begin{bmatrix} k_{T1}+k_{T2} & -k_{T1} & 0 & 0 & -k_{T2} & 0 & 0 \\ -k_{T1} & k_{PX11}+k_{PX12}+k_{T1} & -k_{PX11} & -k_{PX12} & 0 & 0 & 0 \\ 0 & -k_{PX11} & k_{PX11} & 0 & 0 & 0 & 0 \\ 0 & -k_{PX12} & 0 & k_{PX12} & 0 & 0 & 0 \\ -k_{T2} & 0 & 0 & 0 & k_{PX21}+k_{PX22}+k_{T2} & -k_{PX21} & -k_{PX22} \\ 0 & 0 & 0 & 0 & -k_{PX21} & k_{PX21} & 0 \\ 0 & 0 & 0 & 0 & -k_{PX22} & 0 & k_{PX22} \end{bmatrix} \tag{A.4}$$

A.2 VERTICAL DYNAMICS MATRICES

$$\boldsymbol{q}_{\text{vert}} = \begin{bmatrix} z_V & z_{B1} & z_{B2} & \theta_V & \theta_{B1} & \theta_{B2} \end{bmatrix}^T \tag{A.5}$$

$$\boldsymbol{M}_{\text{vert}} = \begin{bmatrix} \text{diag}[m_V \quad m_{B1} \quad m_{B2}] & [0]_{3\times3} \end{bmatrix} \tag{A.6}$$

$$\boldsymbol{C}_{\text{vert}} = \left[\begin{matrix} c_{s11}+c_{s12}+c_{s21}+c_{s22} & -c_{s11}-c_{s12} & -c_{s21}-c_{s22} \\ -c_{s11}-c_{s12} & c_{s11}+c_{s12}+c_{p11}+c_{p12} & 0 \\ -c_{s21}-c_{s22} & 0 & c_{s21}+c_{s22}+c_{p21}+c_{p22} \end{matrix}\right. \quad \ldots$$

$$\left.\begin{matrix} -c_{s11}L_{V11}-c_{s12}L_{V12}+c_{s21}L_{V21}+c_{s22}L_{V22} & c_{s11}L_{s11}-c_{s12}L_{s12} & c_{s21}L_{s21}-c_{s22}L_{s22} \\ c_{s11}L_{V11}+c_{s12}L_{V12} & -c_{s11}L_{s11}+c_{s12}L_{s12}-c_{p11}L_{p11}+c_{p12}L_{p12} & 0 \\ -c_{s21}L_{V21}-c_{s22}L_{V22} & 0 & -c_{s21}L_{s21}-c_{s22}L_{s22}-c_{p21}L_{p21}+c_{p22}L_{p22} \end{matrix}\right] \tag{A.7}$$

$$\boldsymbol{K}_{\text{vert}} = \left[\begin{matrix} k_{S11}+k_{S12}+k_{S21}+k_{S22} & -k_{S11}-k_{S12} & -k_{S21}-k_{S22} \\ -k_{S11}-k_{S12} & k_{S11}+k_{S12}+k_{P11}+k_{P12} & 0 \\ -k_{S21}-k_{S22} & 0 & k_{S21}+k_{S22}+k_{P21}+k_{P22} \end{matrix}\right. \quad \ldots$$

$$\left.\begin{matrix} -k_{S11}L_{V11}-k_{S12}L_{V12}+k_{S21}L_{V21}+k_{S22}L_{V22} & k_{S11}L_{S11}-k_{S12}L_{S12} & k_{S21}L_{S21}-k_{S22}L_{S22} \\ k_{S11}L_{V11}+k_{S12}L_{V12} & -k_{S11}L_{S11}+k_{S12}L_{S12}-k_{P11}L_{P11}+k_{P12}L_{P12} & 0 \\ -k_{S21}L_{V21}-k_{S22}L_{V22} & 0 & -k_{S21}L_{S21}-k_{S22}L_{S22}-k_{P21}L_{P21}+k_{P22}L_{P22} \end{matrix}\right]. \tag{A.8}$$

A.3 PITCH DYNAMICS MATRICES

$$\boldsymbol{q}_{\text{pitch}} = \begin{bmatrix} x_V & x_{B1} & x_{W11} & x_{W12} & x_{B2} & x_{W21} & x_{W22} & z_V & z_{B1} & z_{B2} & \theta_V & \theta_{B1} & \theta_{B2} \end{bmatrix}^T \tag{A.9}$$

$$\boldsymbol{M}_{\text{pitch}} = \begin{bmatrix} [0]_{3\times 10} & \text{diag}[I_V \quad I_{B1} \quad I_{B2}] \end{bmatrix} \tag{A.10}$$

$$\boldsymbol{C}_{\text{pitch}} = \left[\begin{matrix} H_{VT}(c_{T1}+c_{T2}) & -H_{VT}c_{T1} & 0 & 0 & -H_{VT}c_{T2} & 0 & 0 \\ H_{BT}c_{T1} & -H_{BT}c_{T1} & 0 & 0 & 0 & 0 & 0 & \dots \\ H_{BT}c_{T2} & 0 & 0 & 0 & -H_{BT}c_{T2} & 0 & 0 \end{matrix}\right.$$

$$\begin{matrix} -L_{V11}c_{S11}-L_{V12}c_{S12}+L_{V21}c_{S21}+L_{V22}c_{S22} & L_{V11}c_{S11}+L_{V12}c_{S12} \\ L_{S11}c_{S11}-L_{S12}c_{S12} & -L_{P11}c_{P11}+L_{P12}c_{P12}-L_{S11}c_{S11}+L_{S12}c_{S12} & \dots \\ L_{S21}c_{S21}-L_{S22}c_{S22} & 0 \end{matrix}$$

$$\begin{matrix} -L_{V21}c_{S21}-L_{V22}c_{S22} & L_{V11}^2c_{S11}+L_{V12}^2c_{S12}+L_{V21}^2c_{S21}+L_{V22}^2c_{S22} \\ 0 & -L_{S11}c_{S11}L_{V11}+L_{S12}c_{S12}L_{V12} & \dots \\ -L_{P21}c_{P21}+L_{P22}c_{P22}-L_{S21}c_{S21}+L_{S22}c_{S22} & L_{S21}c_{S21}L_{V21}-L_{S22}c_{S22}L_{V22} \end{matrix}$$

$$\left.\begin{matrix} -L_{V11}c_{S11}L_{S11}+L_{V12}c_{S12}L_{S12} & L_{V21}c_{S21}L_{S21}-L_{V22}c_{S22}L_{S22} \\ L_{P11}^2c_{P11}+L_{P12}^2c_{P12}+L_{S11}^2c_{S11}+L_{S12}^2c_{S12} & 0 \\ 0 & L_{P21}^2c_{P21}+L_{P22}^2c_{P22}+L_{S21}^2c_{S21}+L_{S22}^2c_{S22} \end{matrix}\right] \tag{A.11}$$

$$\boldsymbol{K}_{\text{pitch}} = \left[\begin{matrix} H_{VT}(k_{T1}+k_{T2}) & -H_{VT}k_{T1} & 0 & 0 & -H_{VT}k_{T2} & 0 & 0 \\ H_{BT}k_{T1} & -H_{BT}k_{T1}+H_{P}(k_{PX11}+k_{PX12}) & -H_{P}k_{PX11} & -H_{P}k_{PX12} & 0 & 0 & 0 \\ H_{BT}k_{T2} & 0 & 0 & 0 & -H_{BT}k_{T2}+H_{P}(k_{PX21}+k_{PX22}) & -H_{P}k_{PX21} & -H_{P}k_{PX22} \end{matrix}\right.$$

$$\begin{matrix} & -L_{V11}k_{S11}-L_{V12}k_{S12}+L_{V21}k_{S21}+L_{V22}k_{S22} & L_{V11}k_{S11}+L_{V12}k_{S12} & \\ \dots & L_{S11}k_{S11}-L_{S12}k_{S12} & -L_{P11}k_{P11}+L_{P12}k_{P12}-L_{S11}k_{S11}+L_{S12}k_{S12} & \dots \\ & L_{S21}k_{S21}-L_{S22}k_{S22} & 0 & \end{matrix}$$

$$\begin{matrix} -L_{V21}k_{S21}-L_{V22}k_{S22} & L_{V11}^{2}k_{S11}+L_{V12}^{2}k_{S12}+L_{V21}^{2}k_{S21}+L_{V22}^{2}k_{S22} & \\ 0 & -L_{S11}k_{S11}L_{V11}+L_{S12}k_{S12}L_{V12} & \dots \\ -L_{P21}k_{P21}+L_{P22}k_{P22}-L_{S21}k_{S21}+L_{S22}k_{S22} & L_{S21}k_{S21}L_{V21}-L_{S22}k_{S22}L_{V22} & \end{matrix}$$

$$\left.\begin{matrix} -L_{V11}k_{S11}L_{S11}+L_{V12}k_{S12}L_{S12} & L_{V21}k_{S21}L_{S21}-L_{V22}k_{S22}L_{S22} \\ L_{P11}^{2}k_{P11}+L_{P12}^{2}k_{P12}+L_{S11}^{2}k_{S11}+L_{S12}^{2}k_{S12} & 0 \\ 0 & L_{P21}^{2}k_{P21}+L_{P22}^{2}k_{P22}+L_{S21}^{2}k_{S21}+L_{S22}^{2}k_{S22} \end{matrix}\right]. \tag{A.12}$$

A.4 ROTATIONAL DYNAMICS MATRICES

$$\boldsymbol{q}_{\mathrm{rot}ij} = \begin{bmatrix} \theta_{Lij} & \theta_{Rij} & \theta_{Gij} & \theta_{Mij} \end{bmatrix}^T \tag{A.13}$$

$$\boldsymbol{M}_{\mathrm{rot}} = \mathrm{diag}\begin{bmatrix} I_L & I_R & I_G + R^2 I_P & I_M \end{bmatrix} \tag{A.14}$$

$$\boldsymbol{C}_{\mathrm{rot}} = \begin{bmatrix} c_1 & 0 & -c_1 & 0 \\ 0 & c_2 & -c_2 & 0 \\ -c_1 & -c_2 & c_1 + c_2 + R^2 c_3 & -Rc_3 \\ 0 & 0 & -Rc_3 & c_3 \end{bmatrix} \tag{A.15}$$

$$\boldsymbol{K}_{\mathrm{rot}} = \begin{bmatrix} k_1 & 0 & -k_1 & 0 \\ 0 & k_2 & -k_2 & 0 \\ -k_1 & -k_2 & k_1 + k_2 + R^2 k_3 & -Rk_3 \\ 0 & 0 & -Rk_3 & k_3 \end{bmatrix}. \tag{A.16}$$

APPENDIX B MODEL PARAMETERS

The model parameters (other than Appendix B.1) were obtained from the Transnet locomotive datasheets, discussions with locomotive engineers, and adaptations from [4].

B.1 POLACH MODEL PARAMETERS

Symbol	Description	Value
a	Half - axes of the contact ellipse	0.00821
b	Half - axes of the contact ellipse	0.00796
G	Sheer modulus	82.677×10^9
C_1	Kalker's linear theory coefficient	4.2836
$\frac{\mu_\infty}{\mu_0}$	Ratio of friction coefficients	0.4

Table B.1. Constant adhesion modelling parameters, provided in [32].

Symbol	Description	Very Low	Low	Wet	Dry
k_A	Reduction factor in the area of adhesion	0.3	0.6	1.0	1.0
k_S	Reduction factor in the area of slip	0.1	0.2	1.0	1.0
μ_0	Maximum friction coefficient at zero slip	0.03	0.06	0.3	0.55
B	Coefficient of exponential friction decrease	0.1	0.2	0.6	0.6

Table B.2. Adhesion condition varying parameters, provided in [32].

B.2 LOCOMOTIVE MODEL

Symbol	Description	Value (kg)
m_V	Locomotive vehicle body mass	62 120
m_{B1}	Front bogie mass	11 000
m_{B2}	Rear bogie mass	11 000
m_{Wij}	Wheelset mass	3 400
m_A	Mass per axle	24 430
m	Total locomotive mass	97 720

Table B.3. Mass parameters.

Symbol	Description	Value ($\text{kg} \cdot \text{m}^2$)
I_V	Locomotive vehicle body inertia	3 793 457
I_{B1}	Front bogie inertia	33 585
I_{B2}	Rear bogie inertia	33 585
I_L	Left wheel inertia	154
I_R	Right wheel inertia	154.1
I_G	Gearwheel inertia	24.982
I_P	Pinion inertia	0.161
I_M	Motor rotor inertia	16.205

Table B.4. Inertia parameters.

Symbol	Description	Value	Unit
k_1	Left wheel to gear wheel stiffness	30.152×10^6	$\mathrm{N \cdot m/rad}$
k_2	Right wheel to gear wheel stiffness	21.120×10^6	$\mathrm{N \cdot m/rad}$
k_3	Pinion to motor stiffness	7.382×10^6	$\mathrm{N \cdot m/rad}$
k_{Pij}	Primary suspension vertical stiffness	782×10^3	$\mathrm{N/m}$
k_{PXij}	Primary suspension longitudinal stiffness	101.5×10^6	$\mathrm{N/m}$
k_{Sij}	Secondary suspension stiffness	20×10^6	$\mathrm{N/m}$
k_{Ti}	Traction rods stiffness	25×10^6	$\mathrm{N/m}$

Table B.5. Stiffness parameters.

Symbol	Description	Value	Unit
c_1	Left wheel to gear wheel damping	100.507	$\mathrm{N \cdot m \cdot s/rad}$
c_2	Right wheel to gear wheel damping	70.401	$\mathrm{N \cdot m \cdot s/rad}$
c_3	Pinion to motor damping	24.608	$\mathrm{N \cdot m \cdot s/rad}$
c_{Pij}	Primary suspension vertical damping	50×10^3	$\mathrm{N \cdot s/m}$
c_{Sij}	Secondary suspension damping	50×10^6	$\mathrm{N \cdot s/m}$
c_{Ti}	Traction rods damping	1×10^6	$\mathrm{N \cdot s/m}$

Table B.6. Damping parameters.

Symbol	Description	Value (m)
r	Maximum wheel radius	0.61
H_{VT}	Vehicle body centre of gravity (CoG) to the traction rods vertical distance	1.0
H_C	Vehicle body CoG to the coupler vertical distance	0.8
H_{BT}	Bogie CoG to the traction rods vertical distance	0.2
H_P	Bogie CoG to the primary suspension vertical distance	0.3
L_{B1}	Vehicle body CoG to the front bogie CoG horizontal distance	4.425
L_{B2}	Vehicle body CoG to the rear bogie CoG horizontal distance	3.425
L_C	Vehicle body CoG to the coupler horizontal distance	7.56
L_{Pij}	Bogie CoG to the primary suspension horizontal distance	1.64
L_{Sij}	Bogie CoG to the secondary suspension horizontal distance	0.3
L_{MBij}	Bogie CoG to the pin between the motor housing and bogie	0.24
L_{V11}	Vehicle body CoG to front bogie front secondary suspension horizontal distance	4.725
L_{V12}	Vehicle body CoG to front bogie rear secondary suspension horizontal distance	4.125
L_{V21}	Vehicle body CoG to rear bogie front secondary suspension horizontal distance	3.125
L_{V22}	Vehicle body CoG to rear bogie rear secondary suspension horizontal distance	3.725
L_{MP}	Motor and housing CoG to the pin between the motor housing and bogie	0.5
L_{MW}	Motor and housing CoG to the wheelset axle	0.9

Table B.7. Geometric parameters.

B.3 EXTERNAL FORCES PARAMETERS

Symbol	Description	Value	Unit
R	Gear ratio	$115/17$	-
P_{max}	Maximum locomotive power	800×10^3	W
F_{max}	Maximum locomotive traction	287.6×10^3	N
k_f	Torque reduction factor	1000	$N/(m/s)$
n	Axle count	4	-
τ_M	Inverter and motor time constant	0.05	s

Table B.8. Tractive effort parameters.

B.4 WAGONS MODEL

Symbol	Description	Value	Unit
n_W	Amount of wagons	1	-
m_W	Mass of all the wagons	15000	kg
I_W	Sum of the inertias of all the wheelsets of the wagons	1600	$\text{kg} \cdot \text{m}^2$
k_C	Coupler stiffness coefficient	100×10^6	N/m
c_C	Coupler damping coefficient	300×10^6	$\text{N} \cdot \text{s/m}$

Table B.9. Wagons modelling parameters.

Symbol	Description	Value
K_a	Adjustment factor depending on rolling stock type	0.85
k_{ad}	Air drag constant depending on car type	0.07

Table B.10. Rolling resistance parameters.

B.5 ESTIMATION MODEL

Symbol	Description	Value (m)
H_{CT}	Coupler to the traction rods vertical distance	0.2
H_{BR}	Bogie CoG to the rail distance	0.7954
H_{TR}	Traction rod to the rail distance	1.11
L_{VT1}	Vehicle body CoG to the front bogie traction rod distance	4.425
L_{VT2}	Vehicle body CoG to the rear bogie traction rod distance	3.425
L_{BNij}	Bogie CoG to wheelset distance	1.64

Table B.11. Estimation model geometric parameters.

B.6 CONTROLLER PARAMETERS

Symbol	Description	Value	Unit
τ_{LPF}	Rail angle filter time constant	0.8	s
K_P	PD controller proportional gain	1000	$\mathrm{N \cdot s/rad}$
K_D	PD controller derivative gain	20	$\mathrm{N \cdot s^2/rad}$
τ_D	PD derivative filter time constant	0.001	s
K_p	PI controller proportional gain	2261.9	$\mathrm{N \cdot s/m}$
K_i	PI controller integral gain	5055.3	$\mathrm{N/m}$
K_a	PI controller anti-windup gain	442.1×10^{-6}	$\mathrm{m/(s \cdot N)}$
$K_{p\text{fast}}$	Fast PI controller proportional gain	4090.6	$\mathrm{N \cdot s/m}$
$K_{i\text{fast}}$	Fast PI controller integral gain	32.12×10^{3}	$\mathrm{N/m}$
$K_{a\text{fast}}$	Fast PI controller anti-windup gain	244.5×10^{-6}	$\mathrm{m/(s \cdot N)}$

Table B.12. Controller parameters.